Design Study and Analysis of a Conventional Radial-Field Flux-Switching Permanent Magnet Machine for a Medium-Speed Wind Turbine

by

Dewald Pretorius (PRTDEW002)

Bachelor of Science in Engineering, University of Cape Town, 2016

Dissertation Submitted in Fulfilment of the Requirements
for the Degree of Master of Science in Engineering

in the
Department of Electrical Engineering
Faculty of Engineering and the Built Environment

University of Cape Town
December 18, 2020

This page is intentionally left empty.

Declaration

I know the meaning of plagiarism and declare that all the work in the document, save for that which is properly acknowledged, is my own. This thesis/dissertation has been submitted to the Turnitin module (or equivalent similarity and originality checking software) and I confirm that my supervisor has seen my report and any concerns revealed by such have been resolved with my supervisor.

Signed by candidate

Dewald Pretorius
December 18, 2020

Abstract

Design Study and Analysis of a Conventional Radial-Field Flux-Switching Permanent Magnet Machine for a Medium-Speed Wind Turbine

Dewald Pretorius (PRTDEW002)

Menzies Building, Department of Electrical Engineering, Faculty of Engineering and the Built Environment, University of Cape Town, Upper Campus, Rondebosch 7701, South Africa

Dissertation: MSc(Eng) in Electrical Engineering
December 18, 2020

A conventional radial-field FSPM machine was designed and studied. The research focussed on the effectiveness of using a parametric study to obtain an optimized solution compared to using a computerized optimizer; as well as an in-depth core loss analysis. The designing process started with an analytical design that was used for initial design purposes, and this was followed by numerical simulations to get an optimized solution. Within the numerical simulations, the parametric analysis and optimization were performed. The final optimized design was designed to be manufactured and compared to both the analytical and numerical results for validation. The analytical and numerical results were obtained using MathWorks MATLAB 2019a and Ansys Maxwell 19.1 respectively. The results show that an optimizer is more effective in finding an optimized solution in the design space, however, the parametric analyses are still useful in order to determine the design regions for the optimizer and how sensitive certain parameters are towards the FSPM machine's performance. In the end, these analyses are used to speed up the design process by minimizing computational time, and also provides an understanding to the designer of parameter changes on the FSPM machine's performance.

Acknowledgements

First and foremost, I would like to thank my parents, Lizda and Lionel Pretorius, for their love, patience, understanding and constant support throughout my postgraduate studies. I would like to thank my supervisor, Professor Azeem Khan, for his support, meetings and valuable discussions and insight related to this dissertation. To Riyaad Jacobs for his assistance on the mechanical design considerations. To Doctor Akuru at Stellenbosch University and Darren Dudley for their assistance with the Ansys Maxwell Software. To Bethany and Sean for being supportive friends and showing interest in my research over the last two years. Lastly, I would like to thank the South African Department of Science and Technology and the National Research Foundation for the scholarship that gave me the opportunity to conduct this research.

Contents

List of Tables vii
List of Figures viii
Nomenclature xii
Abbreviations xvi

1 Introduction **1**
1.1 Background 1
1.2 Defining the Problem 4
1.3 Objectives 4
1.4 Methodology 5
1.5 Limitations 5
1.6 Dissertation Layout 6

2 Flux-Switching Permanent Magnet Machines **7**
2.1 Operating Principle 7
2.2 Topologies 9
2.3 Optimal Dimensions and Ratios 12
2.3.1 Initial Geometrical Dimensions 12
2.3.2 Parameters under Investigation 12
2.3.3 Summary of Optimal Dimensions and Ratios 16
2.4 Design Methods 16
2.5 Material Selection 16

3 Electrical Drives **18**
3.1 Operating Principle 18
3.1.1 Independent Generator 18
3.1.2 Electrical Drive Controlled 19
3.2 Topologies 19
3.3 Reference Frame Conversions 22
3.4 Electromagnetic Modelling of a PM Machine 23

4 Development of the FSPM Machine **25**
4.1 Geometrical Data . . . 25
4.2 Back-EMF . . . 26
4.2.1 Winding Turns Per Phase . . . 26
4.2.2 Flux . . . 27
4.2.3 Final Back-EMF Equation . . . 28
4.3 Magnetic Circuit Modelling . . . 29
4.4 Induced Current . . . 34
4.5 Losses . . . 35
4.6 Sizing Equation . . . 36
4.7 Winding Configurations . . . 37
4.8 Cogging Torque . . . 40

5 Initial FSPM Machine Design **41**
5.1 Analytical Design . . . 42
5.2 Numerical Analysis of the FSPM Machine . . . 44
5.2.1 Setup . . . 44
5.2.2 Initial Results . . . 46

6 Parametric Design and Analysis **51**
6.1 Stator Outer Rib . . . 52
6.2 Rotor Pole Width . . . 54
6.3 Stator Back-Iron . . . 56
6.4 Permanent Magnet Thickness . . . 58
6.5 Rotor Yoke Thickness . . . 60
6.6 Summary . . . 62
6.7 Design Using Optimal Parametric Ratios . . . 65

7 Optimization **76**
7.1 Optimization Setup and Results . . . 77
7.2 Finalized FSPM Machine Design . . . 81

8 Core Loss Analysis **85**
8.1 Modelling of Core Losses . . . 85
8.2 Determination of Core Losses . . . 90

9 Conclusion and Recommendations **98**

Bibliography **100**

Appendices **107**
Appendix A - Scripts 107
Appendix A.1 - FSPM Stator Outer Diameter vs. Stack Length 107
Appendix A.2 - FSPM Geometrical Parameters 111
Appendix A.3 - Core Loss Curve Fitting 113
Appendix A.4 - Core Loss Curve Fitting for Flux Densities 115
Appendix A.5 - Magnetic Circuit Modelling 116
Appendix A.6 - Deep Learning for Core Losses 119
Appendix A.7 - Machine Learning for Core Losses 122
Appendix B - Mechanical Drawings 125
Appendix B.1 - Stator Laminations 125
Appendix B.2 - Rotor Laminations 126
Appendix B.3 - Permanent Magnets 127
Appendix C - Wire Gauge Chart 128

List of Tables

1.1 Classification of Generators Based on Rotational Speed 2

2.1 Summary of Optimized Parameters 16
2.2 Properties of M400-50A Silicone Steel 17
2.3 Properties of NdFeB35 Rare-earth Magnets 17

4.1 Comparison between electrical and magnetic circuit elements 29

5.1 Initial Estimation of Parameters 42
5.2 Design Constraints of a Conventional FSPM Machine 42
5.3 Design Data of a Conventional FSPM Machine 44
5.4 Initial Design Data Comparison 49

6.1 Initial vs. Parametrically Optimized (PO) FSPM Machine's Performance 64
6.2 Optimal Geometric Ratios Obtained from Parametric Analysis 65
6.3 Estimation of Parameters 65
6.4 Analytical Design Data Using Parametrically Optimized Ratios 68
6.5 New Analytical vs. Parametrically Optimized (PO) FSPM Machine's Performance Characteristics 71
6.6 Design Data Using Parametrically Optimized Ratios 75

7.1 Optimized Parameters Using Sequential Non-Linear Programming Optimizer 79
7.2 Geometric Ratios Obtained from Parametric Analysis vs. Optimizer . . . 79
7.3 Design Data Using Optimizer 80
7.4 Final FSPM Design Data 84

8.1 X, Y, Z, k_e, k_{ex} and k_h coefficients at different flux densities 87
8.2 Frequencies in Different Magnetic Core Parts of an FSPM Machine . . . 94
8.3 Individual Core Losses 96

List of Figures

1.1 Benefits of SR, PM and FSPM machines 3
1.2 Output torque vs. rated speed from existing 3-phase FSPM machine research 3

2.1 FSPM machine with all poles wound 8
2.2 Operating principle of FSPM machines from generator-oriented perspective. (a) Rotor at four typical positions. (b) Ideal PM flux, back-EMF, and phase-current waveforms 8
2.3 a) Numbered armature coils on the stator b) Coil-EMF vectors c) Phase coil vectors d) Phase winding connections 9
2.4 FSPM Topologies (a) Conventional with all poles wound. (b) Conventional with alternate poles wound. (c) Multi-tooth. (d) E-core. (e) C-core. (f) DC winding excited. (g) Modular rotor. (h) Modular rotor DC excited. (i) Hybrid excited. (j) Hybrid excited E-core 11
2.5 Coil EMF vectors and winding configuration for a 12 slot all-poles-wound FSPM machine with rotor pole numbers of a) 10, b) 11, c) 13 and d) 14 . 14

3.1 High-level overview of the machine- and grid-side converters 19
3.2 Hysteresis Band Current Control Strategy 19
3.3 Field Oriented Control Strategy 20
3.4 Voltage Oriented Control Scheme 20
3.5 Vector Oriented Control Scheme 21
3.6 Comparison of the abc to the $\alpha\beta$ and dq reference frames 22

4.1 Geometry of conventional FSPM machine with labels 25
4.2 a) Flux lines contributing to the stator pole in its aligned position with the b) approximate air-gap leakage flux paths 30
4.3 Air-gap leakage flux path approximates 31
4.4 Magnetic circuit model using reluctances, MMF and flux 32
4.5 PM magnetization direction and pole number for a 12 stator slot FSPM . 38
4.6 Coil EMF vectors for a 12/14 FSPM 38

4.7 Sectors indicated by green area for a 12/14 FSPM 39
4.8 Coil EMF vectors for a 12/14 FSPM grouped by phase 39

5.1 Design process followed in this dissertation 41
5.2 Stack length vs. stator outer diameter to achieve design requirements based on initial estimates of K_d, B_{peak} and ϵ 43
5.3 12/14 FSPM in the d-axis position including flux lines 45
5.4 Phase flux indicating d- and q-axis positions 46
5.5 Phase A back-EMF of initial design 46
5.6 Cogging torque 47
5.7 No-load air-gap flux density 47
5.8 Phase A Full-load Voltage and Current 48
5.9 Output Power 49

6.1 Back-EMF vs. the rib length on the stator's outer diameter 52
6.2 Cogging torque vs. the rib length on the stator's outer diameter 52
6.3 Nominal FSPM a) Flux lines and b) Flux density in the d-axis position . 53
6.4 FSPM with 2mm outer rib a) Flux lines and b) Flux density in the d-axis position 53
6.5 Back-EMF vs. the ratio of new rotor pole thickness to the nominal . . . 54
6.6 Cogging torque vs. the ratio of new rotor pole thickness to the nominal . 54
6.7 FSPM with 2mm outer rib a) Flux lines and b) Flux density in the d-axis position 55
6.8 FSPM with 1.4 times the nominal rotor pole thickness a) Flux lines and b) Flux density in the d-axis position 55
6.9 Back-EMF vs. the ratio of new stator back-iron thickness to the nominal 56
6.10 Cogging torque vs. the ratio of new stator back-iron thickness to the nominal 56
6.11 FSPM with 1.4 times the nominal rotor pole thickness a) Flux lines and b) Flux density in the d-axis position 57
6.12 FSPM with 1.1 times the nominal stator back-iron thickness a) Flux lines and b) Flux density in the d-axis position 57
6.13 Back-EMF vs. the ratio of new PM thickness to the nominal 58
6.14 Cogging torque vs. the ratio of new PM thickness to the nominal 58
6.15 FSPM with 1.4 times the nominal rotor pole thickness a) Flux lines and b) Flux density in the d-axis position 59
6.16 FSPM with 0.8 times the nominal permanent magnet thickness a) Flux lines and b) Flux density in the d-axis position 59
6.17 Back-EMF vs. the ratio of new rotor yoke thickness to the nominal . . . 60

6.18 Cogging torque vs. the ratio of new rotor yoke thickness to the nominal . 60
6.19 FSPM with 0.8 times the nominal permanent magnet thickness a) Flux lines and b) Flux density in the d-axis position 61
6.20 FSPM with 1.3 times the nominal rotor yoke thickness a) Flux lines and b) Flux density in the d-axis position 61
6.21 Back-EMF of parametrically optimized FSPM machine 62
6.22 Cogging torque of parametrically optimized FSPM machine 62
6.23 No-load air-gap flux density of parametrically optimized FSPM machine . 63
6.24 Full-load terminal voltage of parametrically optimized FSPM machine . . 63
6.25 Output power of parametrically optimized FSPM machine 64
6.26 Stack length vs. stator outer diameter to achieve design requirements based on parametrically optimized ratios and estimates of K_d, B_{peak}, ϵ, $cos(\theta)$, H_{ribSO}, β_r, H_{ys}, β_{pm} and H_{yr} 66
6.27 Stack length vs. stator outer diameter using $D_{ac} = 1.829$ mm and $J_s = 4.65\ A/mm^2$ 67
6.28 Back-EMF using ratios in Table 6.3 and dimensions in Table 6.4 69
6.29 Cogging torque using ratios in Table 6.3 and dimensions in Table 6.4 . . 69
6.30 No-load air-gap flux density using ratios in Table 6.3 and dimensions in Table 6.4 70
6.31 Full-load terminal voltage using ratios in Table 6.3 and dimensions in Table 6.4 70
6.32 Output power using ratios in Table 6.3 and dimensions in Table 6.4 . . . 71
6.33 Parametric study of full-load terminal voltage vs. stack length 72
6.34 Parametric study of output power vs. stack length 72
6.35 Back-EMF vs. time for the final parametrically optimized FSPM machine 73
6.36 Cogging torque vs. time for the final parametrically optimized FSPM machine 73
6.37 Full-load terminal voltage and current vs. time for the final parametrically optimized FSPM machine 74
6.38 Output power vs. time for the final parametrically optimized FSPM machine 74

7.1 Cost function vs. number of evaluations (lower is better) 77
7.2 Optimized back-EMF vs. time 77
7.3 Optimized cogging torque vs. time 78
7.4 Optimized full-load terminal voltage and current vs. time 78
7.5 Optimized output power vs. time 79
7.6 Final nominal back-EMF vs. time 81

7.7 Final nominal cogging torque vs. time 82
7.8 Final nominal full-load terminal voltage vs. time 82
7.9 Final nominal output power vs. time 82
7.10 Final losses at rated power vs. time 83
7.11 Variation in current angle on average output torque 83

8.1 Core losses versus flux density for different frequencies as specified by the manufacturer for M400-50A silicone steel 86
8.2 Core losses per frequency versus the square root of the frequency for different flux densities 86
8.3 Eddy current coefficient versus flux density 88
8.4 Excess current coefficient versus flux density 88
8.5 Hysteresis coefficient versus flux density 88
8.6 Core loss comparison between data from manufacturer and analytical computations at a) 50 Hz b) 100 Hz c) 200 Hz d) 400 Hz e) 1000 Hz f) and 2500 Hz 89
8.7 Switched reluctance machine's structure with changes in the flux's frequency in the different zones 90
8.8 Flux in a stator tooth vs. Time 91
8.9 Flux in the stator back-iron vs. Time 91
8.10 Flux in a rotor pole and back-iron vs. Time 91
8.11 Spectral analysis of stator tooth flux 92
8.12 Spectral analysis of stator back-iron flux 92
8.13 Spectral analysis of rotor pole flux 93
8.14 Spectral analysis of rotor back-iron flux 93
8.15 Derived core losses at a) 25 Hz and b) 58.33 Hz 94
8.16 Derived core losses at a) 75 Hz b) 116.67 Hz c) 125 Hz d) 175 Hz and e) 233.33 Hz 95
8.17 Numerical vs. calculated vs. machine learning core losses 97

Nomenclature

α_{cog}	Mechanical angle corresponding to each cogging torque period
α_e	Electrical degrees
α_m	Mechanical degrees
β	Steinmetz constant
β_r	Rotor pole width
β_s	Stator tooth width
β_{pm}	PM Height
ϵ	Ratio of back-EMF to rated terminal voltage
η	Efficiency
γ	Current angle
λ_d	d-axis flux linkage in the dq reference frame
λ_m	No-load magnetization flux linkage
λ_q	q-axis flux linkage in the dq reference frame
μ_0	Permeability of vacuum
μ_r	Relative permeability of material
ω_e	Angular electrical frequency
ϕ	Flux
ϕ_{3peak}	Average flux in stator tooth 3 in the d-axis
ϕ_{4peak}	Average flux in stator tooth 4 in the d-axis
ϕ_{ag}	Air-gap flux
ρ	Resistivity
$\theta_{initial}$	d-axis position for rotor
A	Area of stator tooth along the axle
a	Area of copper conductor
A_c	Total area of copper in a slot
A_{slot}	Total area of a slot
A_{stator}	Total area of the stator
A_s	Specific electric loading
B	Peak sinusoidal flux density

B_{3peak}	Average flux density in stator tooth 3 in the d-axis
B_{4peak}	Average flux density in stator tooth 4 in the d-axis
B_a	New remanence flux density
B_{peak}	Average flux density in stator tooth top in the d-axis
B_R	Old remanence flux density
B_T	Flux density
C_s	Ratio of stator tooth width to pole pitch
$cos(\theta)$ or PF	Power factor
D_{cu}	Diameter of copper conductor
D_g	Air-gap diameter
D_{ri}	Rotor inner diameter
D_{ro}	Rotor outer diameter
D_{si}	Stator inner diameter
D_{so}	Stator outer diameter
E	Induced voltage
E_{peak}	Peak back-EMF
E_{rms}	RMS back-EMF
f	Electrical frequency
f_e	Frequency of flux
F_{pm}	Magneto-motive force for a PM
g	Air-gap length
H_{ph}	Rotor pole length
H_{slot}	Stator slot opening width
H_{yr}	Rotor back-iron or yoke thickness
H_{ys}	Stator back-iron or yoke thickness
I_α	α-axis current in the $\alpha\beta$ reference frame
I_β	β-axis current in the $\alpha\beta$ reference frame
I_a	a-axis current in the abc reference frame
I_b	b-axis current in the abc reference frame
$I_{d(pk-pk)}$	Peak d-axis current in the dq reference frame
I_d	d-axis current in the dq reference frame
$I_{q(pk-pk)}$	Peak q-axis current in the dq reference frame
I_q	q-axis current in the dq reference frame
I_{rms}	RMS current
I_s	Total current in the dq reference frame
J_s	Current density
K_{cu}	Slot-fill factor

K_d	Flux leakage factor
K_{er}	Rotor embrace
K_{es}	Stator embrace
k_{ex}	Excess loss coefficient
k_e	Eddy current loss coefficient
k_h	Hysteresis loss coefficient
K_l	Aspect ratio
K_{pm}	Temperature coefficient
K_{sio}	Split ratio
L	Flux path length
l_a	PM thickness
L_{COIL}	Phase winding inductance
l_{COIL}	Phase winding length
L_d	d-axis inductance in the dq reference frame
l_{ph}	Length of copper conductor
L_q	q-axis inductance in the dq reference frame
l_{st}	Stack length
m	Number of phases
N_{cog}	Number of cogging torque periods
N_r	Number of rotor poles
n_r	Mechanical speed
N_s	Number of stator slots
N_t	Number of copper turns per phase
p	Number of pole pairs
P_{cu}	Copper loss
P_c	Core losses
P_{ex}	Excess losses
P_e	Eddy current losses
P_h	Hysteresis losses
P_{loss}	Total losses
P_{out}	Real output power
Q_{out}	Reactive output power
R	Reluctance of iron parts
R_{ag}	Air-gap reluctance
R_g	Air-gap radius
R_{ph}	Phase winding resistance
r_{ph}	Conductor radius

R_{ri}	Rotor inner radius
R_{ro}	Rotor outer radius
R_{si}	Stator inner radius
R_{so}	Stator outer radius
S	Cross sectional area
T_0	Ambient temperature
T_1	New temperature
T_{cog}	Cogging torque
T_{em}	Electromagnetic torque
T_{out}	Output torque
T_r	Rotor pole pitch
T_s	Stator pole pitch
$V_{d(pk-pk)}$	Peak d-axis voltage in the dq reference frame
V_d	d-axis voltage in the dq reference frame
$V_{q(pk-pk)}$	Peak q-axis voltage in the dq reference frame
V_q	q-axis voltage in the dq reference frame
V_s	Total voltage in the dq reference frame
$V_{t_{rms}}$	RMS terminal voltage
V_t	Terminal voltage
W_c	Magnetic field energy
X_L	Phase winding inductive reactance
Z	Total number of armature conductors
Z_{COIL}	Phase winding impedance

Abbreviations

DSEM	Doubly Salient Electrical Machine
FSPM	Flux-switching Permanent Magnet
FRM	Flux Reversal Machine
DSPM	Doubly Salient Permanent Magnet
GCD	Greatest Common Divisor
DFIG	Doubly-Fed Induction Generator
PMSG	Permanent Magnet Synchronous Generators
EESG	Electrically Excited Synchronous Generators
IG	Induction Generators
SCIG	Squirrel Cage Induction Generator
WRIG	Wound Rotor Induction Generator
SR	Switched Reluctance
PM	Permanent Magnet
DC	Direct Current
AC	Alternating Current
IPM	Interior Permanent Magnet
SPM	Surface Mounted Permanent Magnet
FEA	Finite Element Analysis
THD	Total Harmonic Distortion
SVPWM	Space Vector Pulse Width Modulation
RMS	Root Mean Square
SNLP	Sequential Non-linear Programming
ML	Machine Learning

Chapter 1

Introduction

This chapter contains a brief summary of the generators used in the wind industry and FSPM machine background, followed by the problem identification, primary and secondary objective outlining, methodology, limitations and the layout of this dissertation.

1.1 Background

Wind energy is one of the most prominent power generation solutions in the 21st century, providing clean, sustainable and cost effective energy conversion. One of the pioneers in the wind industry is Vestas, having more than 102 GW of wind turbines installed by them. This is approximately 17 % of the global installed wind capacity and their turbines range from 2-5.6 MW [1].

Generally, the type of generators that are used in wind turbines depends on the size of the rated output power. A study in [2] shows that Vestas, General Electric, Goldwind and Gamesa uses Doubly-Fed Induction Generators (DFIGs) and Permanent Magnet Synchronous Generators (PMSGs) for their wind turbine applications, whereas Enercon focusses on Electrically Excited Synchronous Generators (EESGs), Dongfang and Repower on DFIGs, and Suzlon and Siemens on Induction Generators (IGs). PMSGs are becoming more popular since their performance characteristics are improving with newer technologies and the cost of PM material and power converters are reducing. Furthermore, for direct-drive offshore wind turbines, this is particularly attractive as the gearbox costs are reduced and an added robustness layer is observed because of this.

In [2], wind energy conversion systems are classified as small ($<$ 2 kW), medium (2-100 kW) and large ($>$ 100 kW). It is further extended to the rotational speed being

either fixed, limited variable or variable speed. Note that the majority of the wind turbine manufactures are developing either DFIGs or PMSGs, corresponding to the variable speed class. This is expected since variable speed wind turbines can provide better efficiency over a wide range of wind speeds and a lot of research has been conducted on this class.

Table 1.1: Classification of Generators Based on Rotational Speed [2]

Fixed Speed	**Limited Variable Speed**	**Variable Speed**
Squirrel Cage Induction Generator (SCIG)	Wound Rotor Induction Generator (WRIG)	Doubly-Fed Induction Generator (DFIG)
		Electrically excited Synchronous generator (EESG)
		PM Synchronous generator (PMSG)

With the advancement of technologies and newer opportunities for Permanent Magnet (PM) machines in wind turbines, it's worth looking into more advanced and novel PM machines. Flux Switching Permanent Magnet (FSPM) machines are seen as more modern compared to standard PM machines, even though they've been around for more than a decade. It was originally developed by combining a PM and Switched Reluctance (SR) machine together, giving it benefits of both, and extensive research between FSPM and PM machines have been conducted in [3].

The FSPM machine is generally characterized by having a high power density, robust mechanical structure, sinusoidal back-EMF and good flux-weakening capabilities [4]. As for the application of FSPM machines in wind energy and since it has a doubly salient structure and contains PMs, it is very important to consider the cogging torque during the design phase as a low cogging torque assists the generator to start generating power at low wind speeds [5] and also reduces acoustic noise and vibrations. The main benefits that the FSPM machine takes from the SR and conventional PM machines are the robust rotor and easy controllability respectively. Figure 1.1 summarizes some benefits of the SR, PM and FSPM machines.

The output torque and rated speed of some of the FSPM machines that have been researched for this dissertation are summarized in Figure 1.2. The data points in Figure 1.2 show a trend that the output torque is lower at higher speeds. This ensures that the

power density of these machines can be increased without increasing the material costs, since the rated speed increases instead. This does however pose problems with heating and demagnetization of the PM machine's magnets. Cooling methods should therefore be taken into account to improve the machine's performance while being mindful of the financial implications these cooling solutions have.

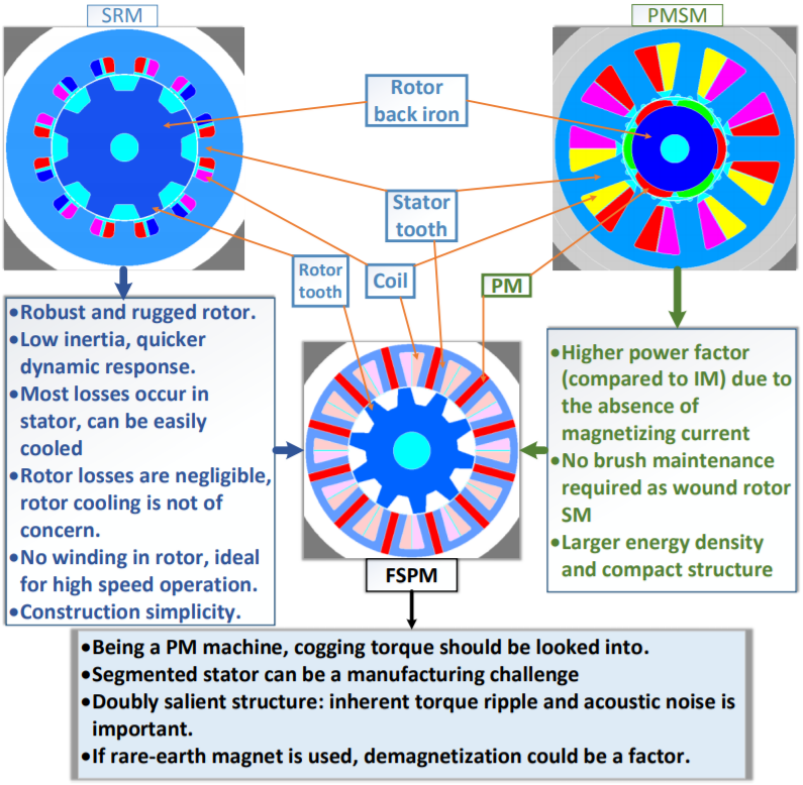

Figure 1.1: Benefits of SR, PM and FSPM machines [3]

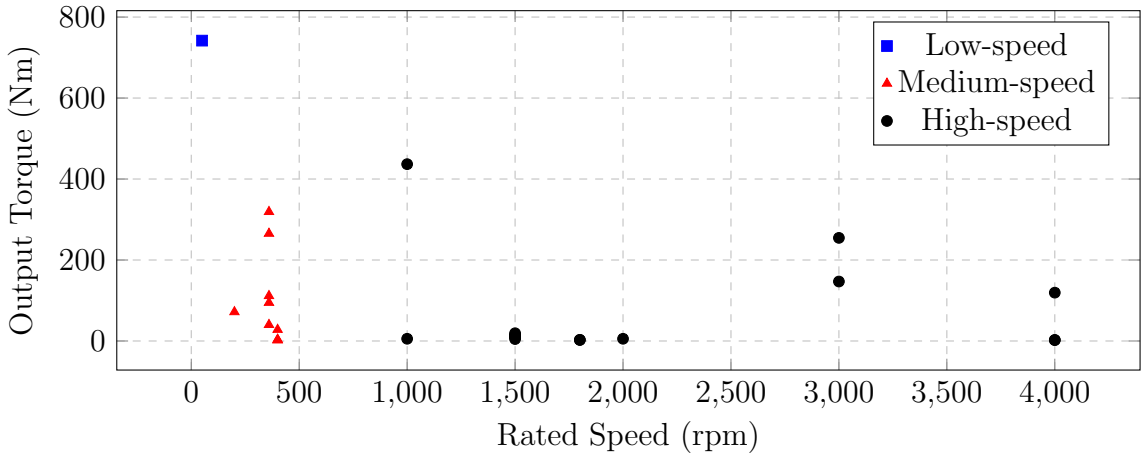

Figure 1.2: Output torque vs. rated speed from existing 3-phase FSPM machine research

FSPM machines are used for a number of different applications with te majority of the research focussing on wind energy and electric vehicles. This does not however mean that these are the only applications. Since the FSPM machine is derived from SR and PM machines, applications where those machines are used, will also be applicable to the FSPM machine.

1.2 Defining the Problem

After studying existing research on the FSPM machine and its design procedure, it became apparent that there's no set approach to assist designers in its development. This might be because researchers assume this process to be well-known. Nevertheless, even though the analytical approach is essentially only used for initial design purposes, it helps to understand why certain parameters have been set the way they are in the existing research. It also helps to think of new ideas to achieve certain results, and set up hypotheses based on the analytical equations instead of following a trial-and-error approach. The majority of the research on FSPM machines only show optimized results that's obtained from parametric studies. Even though this is very helpful to improve the performance of the machine, it can be further improved by using an optimizer. This is due to the fact that a parametric analysis studies the effect that a single parameter has on the objective (design requirements i.e. performance/geometrical constraints). Once more than one parameter is analysed (as with multi-objective optimization), the previously optimized result may not be at an optimum point in the design space. Therefore, a multi-parameter, multi-objective optimization has to be performed to determine the most optimum solution in the design space.

1.3 Objectives

The primary objectives for this dissertation are to successfully design and analyse an FSPM machine with an output power of 6 kW, a rated speed of 250 rpm and full-load terminal voltage of 220 V_{rms}. It's important to note that the designed FSPM machine will be implementation for validation at a later stage. Below is a list of secondary objectives:

- Analytically model an FSPM machine and show understanding of the development of the sizing equation.
- Perform 2-D numerical simulations for designing.

- Perform a parametric study to see the effect of single parameter changes on the back-EMF and cogging torque.
- Use an optimizer to find the most optimum point of the parameters in the entire design space where the parameters meet the design objectives.
- Minimize cogging torque and maximize the back-EMF.
- Perform a core loss analysis on the FSPM machine.

1.4 Methodology

This dissertation proposes a set approach for an initial design for the conventional radial field FSPM machine by means of scripts. Furthermore, the FSPM machine is numerically analysed using Ansys Maxwell, whereby parametric studies are performed to manually determine the optimum geometrical dimensions. This is followed by an optimization, which is used in the final stages to determine the best design solution in the entire design space. In order to provide a fair comparison between the solution of the parametrically optimized design and that obtained by using an optimizer toolbox, the initial design obtained from the parametrically optimized design is used as a starting point for the optimizer. This will ultimately reduce the computational time since the focus range that the optimizer must use is closely defined. The parametric studies include outer ribs added on the stator's outer diameter to ease assembly, and a stator tooth-tip widening study to reduce the saturation in the stator tooth-tips. Lastly, an in-depth core loss analysis is also performed and compared to the numerical core losses for validation.

1.5 Limitations

The limitations imposed in this dissertation are mostly related to the practical implementation. The FSPM machine will be connected to an existing Direct Current (DC) machine in the laboratory to drive it as a generator. The initial size of the shaft that I designed it for is 35 mm, however, this was changed to 40 mm when the focus shifted towards the implementation. Since the machine is for medium speed and a low slot-fill factor is chosen, a thermal analysis and complicated cooling methods are not required. Lastly, Covid-19 has caused significant manufacturing delays and has therefore forced a change in the initial scope to exclude the practical implementation.

1.6 Dissertation Layout

This dissertation is split into nine chapters:

- Chapter 1 contains the background and an introduction to FSPM machines. This includes the dissertation layout and methodology.
- Chapter 2 contains more detail on the FSPM machines and includes the general operating principles used, the different topologies that have been researched, optimal geometrical design parameters found in research, current design methods used for initial design purposes, and material selection for the PMs and cores.
- Chapter 3 contains information on PM machine drives and includes the general operating principles of a few popular topologies that have been researched.
- Chapter 4 contains an in-depth theoretical approach towards the formulation of the sizing equations of FSPM machines. This includes the back-EMF, rated current, torque, winding configurations, and cogging torque.
- In Chapter 5, the initial analytical design is performed using the scripts in Appendices A.1 and A.2. The numerical simulations are performed on the FSPM machine to meet the desired design constraints.
- In Chapter 6, a parametric design study is performed and numerically analysed.
- In Chapter 7, a suitable optimizer is chosen to automatically find the most optimum solution in the design space that conforms to the design constraints.
- In Chapter 8, an in-depth core loss analysis is performed.
- In Chapter 9, the concluding remarks and recommendations are made.

Chapter 2

Flux-Switching Permanent Magnet Machines

This chapter explores the operating principle of the conventional FSPM machine, the different FSPM machine topologies along with their benefits and shortcomings, discuss existing research that has been conducted on optimized parameters and the initial analytical design of any FSPM machine topology.

2.1 Operating Principle

Figure 2.1 shows a 12/10 conventional FSPM machine and its clear that concentrated windings are employed. Individual phases are wound in series, forming a wye-connection with a shared neutral point. Figure 2.2 shows that a stator pole consists of two stator teeth with a permanent magnet mashed between them, and an armature coil wound around it. The rotor and stator teeth are aligned (Position A), flux flows through coil X from the stator to the rotor. As the rotor and stator teeth become unaligned (Position B), no flux can flow through coil X. When a different rotor and stator tooth become aligned and flux flows through coil X from the rotor to the stator, the flux becomes reversed. This is the flux-switching characteristic that defines the FSPM machine. When a rotor tooth becomes aligned with a permanent magnet, the permeability of the PM becomes equal to that of a vacuum, resulting in maximum magnetic resistance and subsequently zero flux can flow through coil X. Since the back-EMF is directly proportional to the derivative of the flux, we expect zero volts to be induced in coil X during the peak flux positions i.e. aligned rotor and stator teeth positions. Similarly, during the changeover from aligned to unaligned positions, we expect the induced back-EMF to reach a maximum and minimum during the respective flux flowing positive and negative cycles.

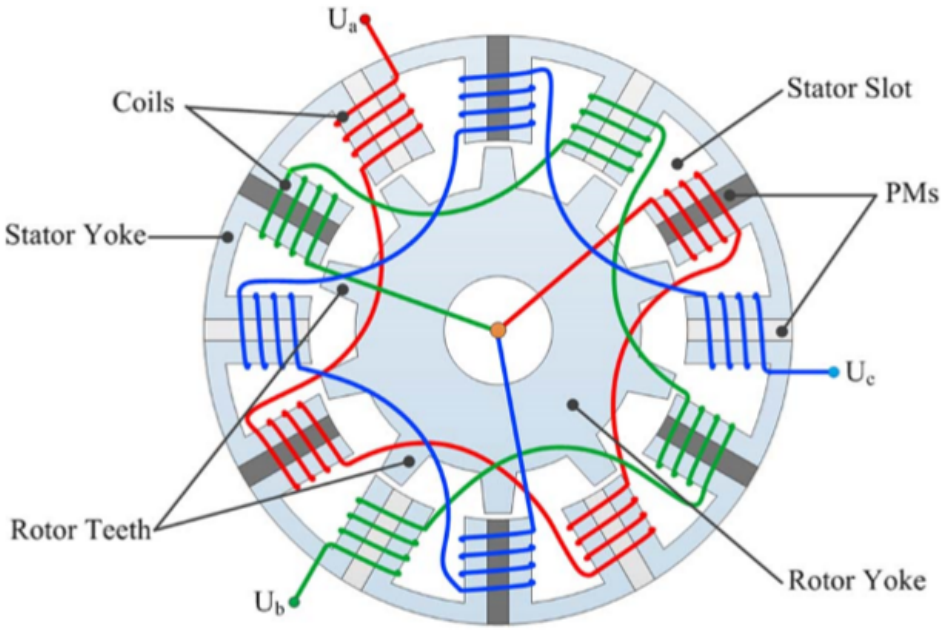

Figure 2.1: FSPM machine with all poles wound [4]

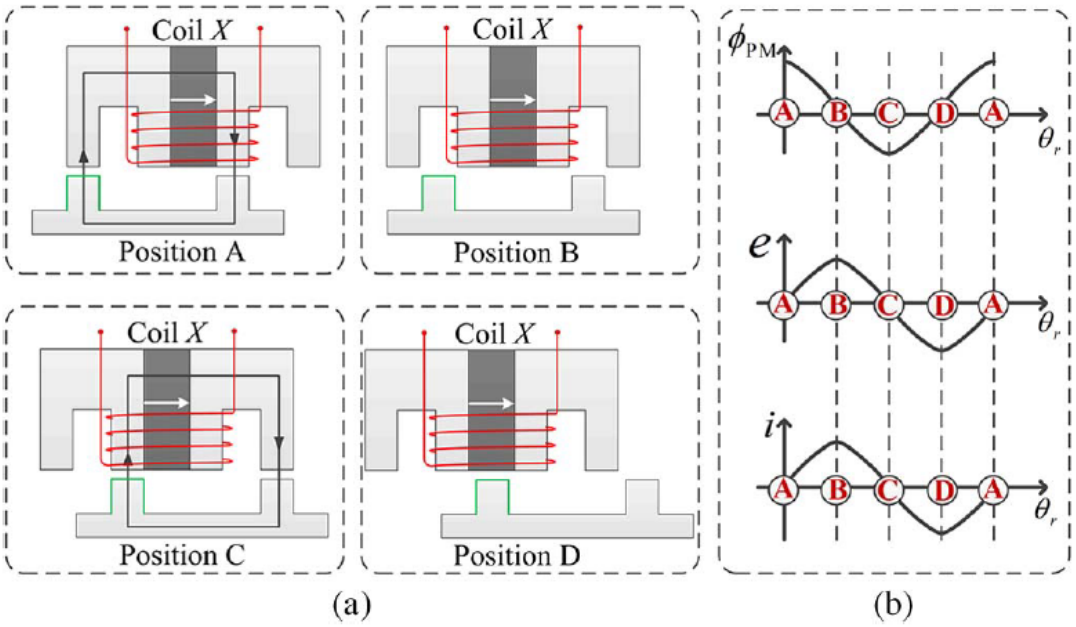

Figure 2.2: Operating principle of FSPM machines from generator-oriented perspective. (a) Rotor at four typical positions. (b) Ideal PM flux, back-EMF, and phase-current waveforms [4]

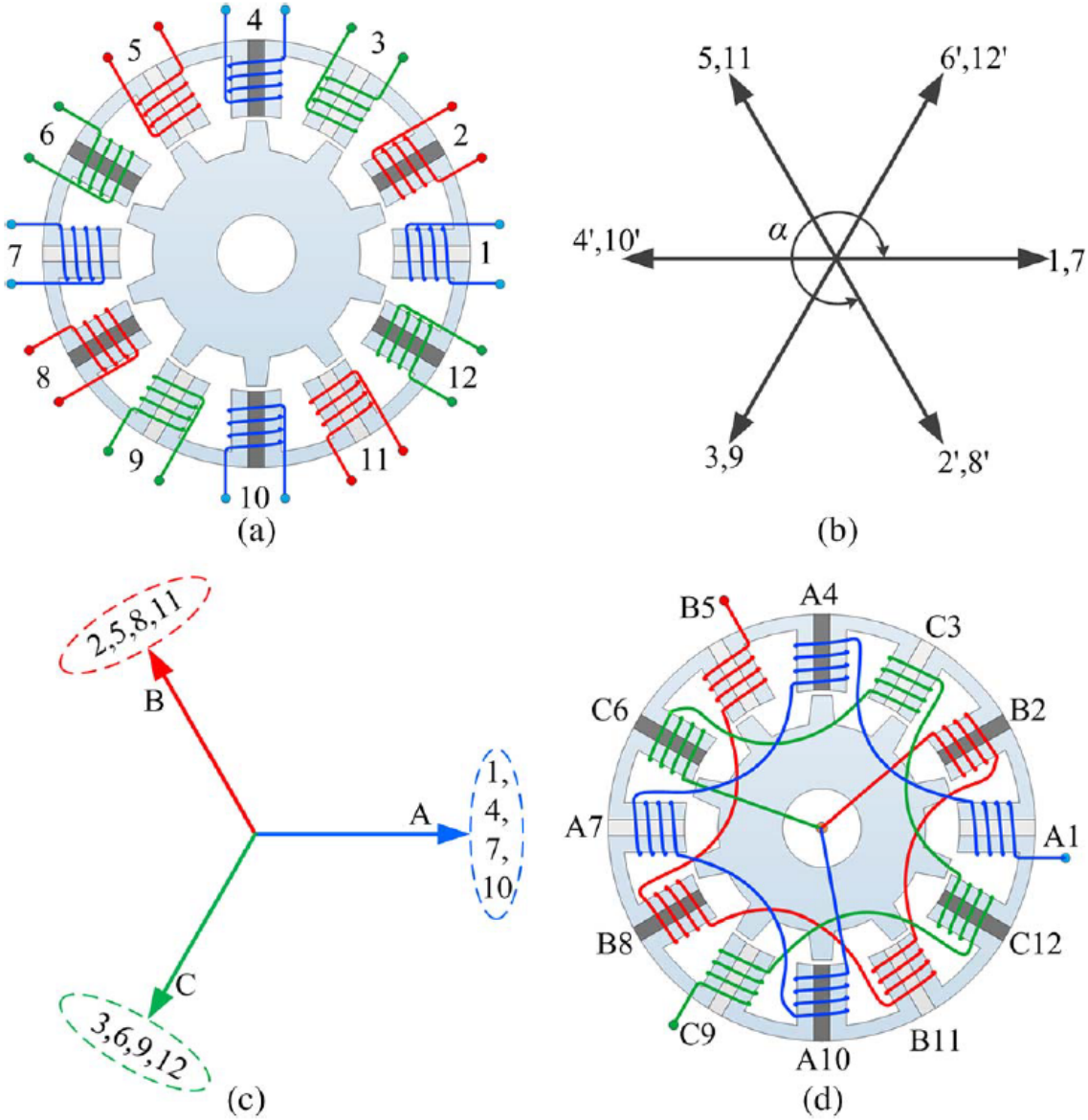

Figure 2.3: a) Numbered armature coils on the stator b) Coil-EMF vectors c) Phase coil vectors d) Phase winding connections [4]

2.2 Topologies

Various FSPM topologies are discussed in [6] and compared with the conventional FSPM. The general torque production on a FSPM relies on the doubly saliency of the rotor and stator, where the conventional FSPM utilizes high magnet volume due to the bigger stator and armature coils. The aim of [6] is to present alternative FSPM topologies to reduce the magnet volume while maintaining or increasing torque production, where the main comparisons are between topologies (a), (c), (d) and (e) as illustrated in Figure 2.4.

Figure 2.4 shows the structure of the different FSPM topologies and visually, some of the benefits can be seen. The conventional topology with alternative poles wounded in (b) makes it more fault tolerant [6] compared to the conventional topology with all poles wound. To reduce the magnet volume, the E-core in (d) was developed and to further increase the slot-area, the C-core was developed. From the general power equation for a FSPM in [7], the slot area is a scalar multiple for torque production, thus, a bigger slot area results in higher torque.

For both the E- and C-core machines, the rotor pole number are almost double that of the stator slot number, whereas in the conventional topology, this is close to the stator slot number. The multi-tooth topology in (c) reduces the magnet volume while improving the torque density. For the purpose of this research, DC and Hybrid excited topologies (f), (h), (i) and (j), are omitted. This decision is based on the fact that the purpose of the FSPM machine in this research is for a wind generator, so flux-adjustment capabilities are not of high importance and the excitation capabilities of a DC field coil cannot compete with that of magnets.

In [6], it is shown that the slot area of the conventional FSPM is lower than Surface Mounted Permanent Magnet (SPM) and Interior Permanent Magnet (IPM) machines, but that the same torque can be produced since the air-gap flux density is higher, which is the result of flux focusing and its higher rotor electric frequency. The bipolar flux causes the torque density to be higher than that of doubly salient PM machines that has unipolar flux at a fixed copper loss. Ultimately, the findings in [6] points to using either C-core, E-core or multi-tooth FSPM topologies due to the reduced magnet volume and increased torque density, compared to the conventional FSPM machine.

In terms of torque production between these four topologies, they rank as follows from highest to lowest: C-core, multi-tooth, E-core and conventional. It should be noted that the overload capability of the multi-tooth FSPM is poor, which leads to the C-core as the best FSPM topology to use in terms of torque production, since both of them have a similar performance up to the rated conditions. However, the C-core, E-core and multi-tooth FSPM machines all require an odd number of rotor poles which will cause an unbalanced magnetic force in the machine, which is unwanted as it leads to noise and vibrations.

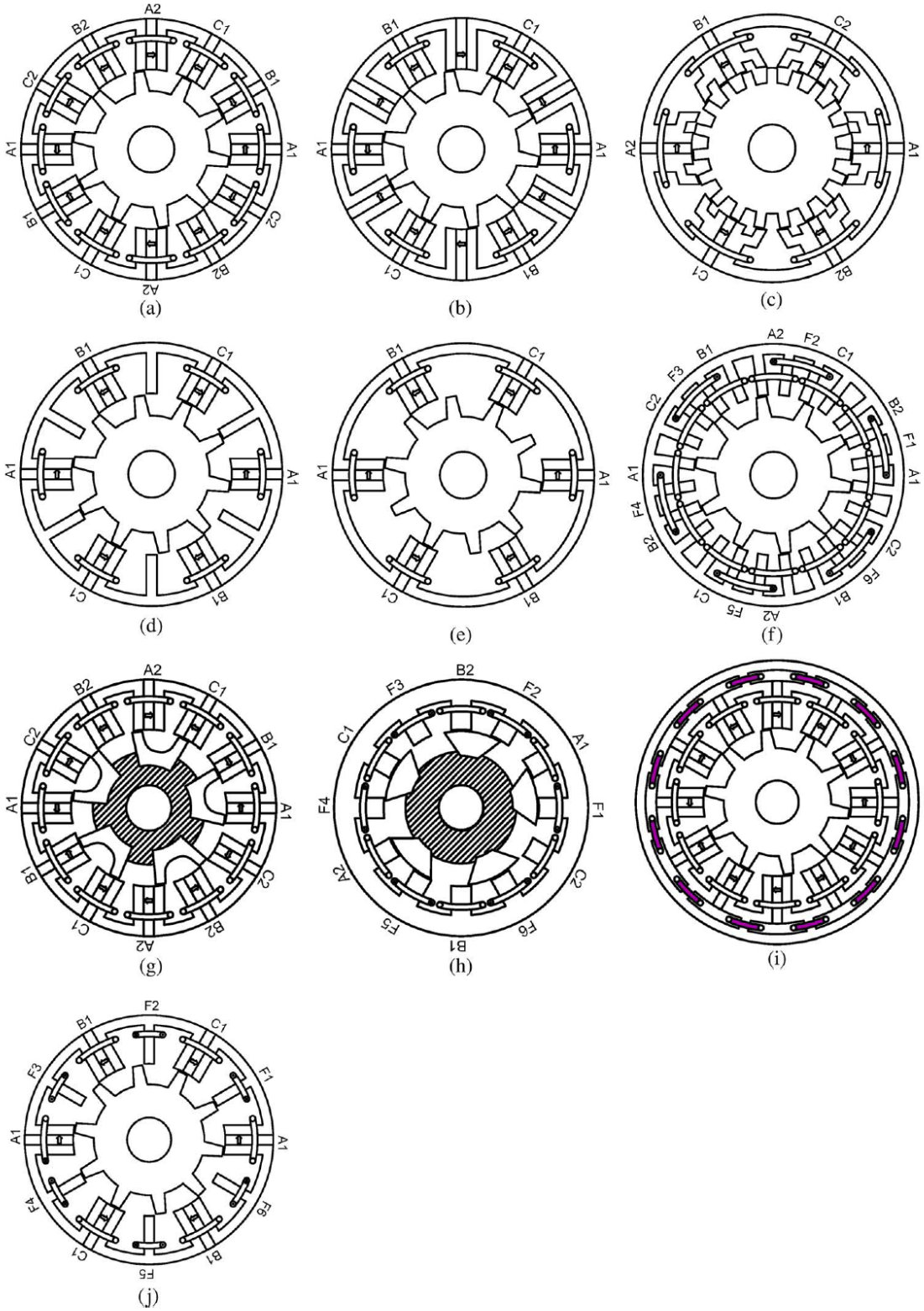

Figure 2.4: FSPM Topologies (a) Conventional with all poles wound. (b) Conventional with alternate poles wound. (c) Multi-tooth. (d) E-core. (e) C-core. (f) DC winding excited. (g) Modular rotor. (h) Modular rotor DC excited. (i) Hybrid excited. (j) Hybrid excited E-core [6]

2.3 Optimal Dimensions and Ratios

This section contains an overview of the initial dimensions that's used when designing an FSPM machine, as well as optimal ratios for the rotor pole width etc. that have been found by researchers.

2.3.1 Initial Geometrical Dimensions

For an initial design and with reference to Figure 4.1, the stator and rotor back-iron, stator slot opening, stator tooth width, rotor pole width and permanent magnet height are equal. Once the initial design has been performed using the parameters obtained in the analytical design, Finite Element Analysis (FEA) software is used to fine-tune the FSPM machine to obtain the desired performance characteristics. With reference to (4.13), the aforementioned geometrical parameters are equal, where T_s is the stator pole pitch and C_s the ratio of stator tooth width to pole pitch:

$$H_{ys} = H_{yr} = H_{slot} = \beta_s = \beta_r = \beta_{pm} = T_s C_s \tag{2.1}$$

2.3.2 Parameters under Investigation

Some of the key areas that researchers have looked at in depth during the designing of FSPM machines include the winding configurations, stator and rotor pole numbers, rotor pole width and split ratio (ratio of stator/rotor outer diameter to stator/rotor inner diameter) [6]. However, it has been stated in [5] that the split ratio and rotor pole width are the biggest influencing factors when it comes to the overall FSPM machine's performance, therefore, those two parameters are generally optimized first, where the rest of the optimizations can follow. The method used in a majority of the research to determine the optimal ratios involves performing parametric studies by means of FEA software, and studying the findings.

2.3.2.1 Rotor Pole and Stator Slot Number

It's been stated in [8–12] that the maximum torque is produced when the rotor pole number is equal to the stator slot number, and that the back-EMF waveforms are balanced and symmetrical when the following equation is adhered to:

$$\begin{cases} N_s = 6k_1, & k_1 \in N^* \\ N_r = N_s \pm k_2, & k_2 \in N^* \end{cases} \tag{2.2}$$

In order to get balanced symmetrical back-EMF, the following condition should be met [6, 8–10, 12, 13]:

$$\frac{N_s}{GCD(N_s, N_r)} = 6k, k \in N^* \tag{2.3}$$

As stated in [13], the rotor pole number should be an even number to avoid single sided magnetic pull. Since torque increases with the rotor pole number, the higher number is preferred, which also increases the stator frequency and is therefore suitable for low-speed high torque applications. It has also been noted in [8] that the rotor pole number has to be high enough to allow for the flux-switching to occur every half rotor pole pitch.

2.3.2.2 Rotor Pole Width

The optimized rotor pole width reduces as the rotor pole number increases, while the optimized ratio of rotor pole width to rotor pole pitch stays approximately 1/3 for all FSPM topologies [6]. An optimal ratio of rotor pole width has been found in [9] to be 1.6 times the slot opening width.

2.3.2.3 Split Ratio

The split ratio is sensitive to the stator slot number, but not so much on the rotor pole number due to the stator's back-iron and slot area [6]. There have been optimized ratios as given in [5], which indicates that a higher split ratio results in a higher power factor and that the optimal split ratio depends on the stator and rotor slot and pole numbers respectively. It can be seen from [14] that the optimal split ratio will also result in a minimum Total Harmonic Distortion (THD) and a maximum back-EMF at the expense of an increase in cogging torque. Therefore, a balance between the optimal results will have to be found, as some improvements come at the expense of other performance characteristics. In [9], the optimal split ratio was found to be 0.6.

2.3.2.4 Coil EMF Vectors

According to [4], if the electrical degrees between two adjacent coil-EMF vectors equal 0°, 90°, 180° or 270°, the stator coils cannot form three-phase symmetric windings. By choosing an equal number of rotor poles and stator slot numbers, the electrical degrees between two adjacent coil-EMF vectors will be equal to 90°, which will result in un-symmetrical three-phase windings. It has been stated in [4, 6, 9, 12] that the electrical degrees (α_e) of a FSPM machine in (2.5) is double that of a conventional fractional-slot PM machine in (2.4) for the same mechanical degrees (α_m), where p is the number of

pole pairs:

$$\alpha_e = p\alpha_m \tag{2.4}$$

$$\alpha_e = N_r\alpha_m \tag{2.5}$$

The coil EMF vectors and winding configuration for 12-slot FSPM machines have been derived in [9]:

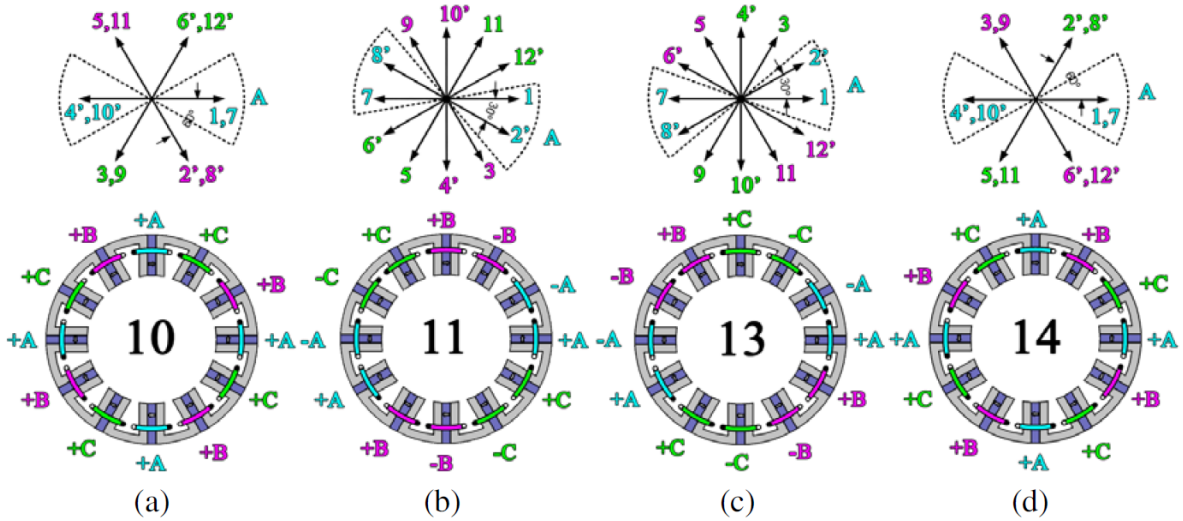

Figure 2.5: Coil EMF vectors and winding configuration for a 12 slot all-poles-wound FSPM machine with rotor pole numbers of a) 10, b) 11, c) 13 and d) 14 [9]

2.3.2.5 Airgap Length

Other design influences include that of the air-gap size, which indicates that a smaller air-gap relates to better electromagnetic performance.

2.3.2.6 Stator Iron Bridges

Stator iron bridges can be employed to link the stator segments together, making is easier to assemble, however, it should be as small as possible while considering the mechanical strength and production of the laminations, so that the leakage flux is kept at a minimum in these bridges [13].

2.3.2.7 Stator Tooth Tips

Stator tooth tips can be used to hold the armature windings in place and the frame eddy current losses, which is caused by the leakage flux outside of the stator, can be reduced

by adding slits in the frame [6].

2.3.2.8 Rotor Iron Losses

The rotor iron losses of FSPMs are generally high due to the fundamental wave moving synchronously with the rotor [13]. The modular rotor (g) in Figure 2.4 might help reduce the rotor's iron losses and further research will need to be done, as current research on this topology provides limited useful information.

2.3.2.9 Cogging Torque

The cogging torque of FSPM machines are high because of the high flux density in the air-gap due to the flux focusing effect [15]. Furthermore, it has been proposed and verified in [15] through simulation and experiments that by adding dummy slots on the rotor, cogging torque can be reduced considerably, from 3 Nm p-p to 0.38 Nm p-p. This method is convenient and allows designers to deviate from other cogging torque reduction methods such as pole arc optimization, skewing, magnet shifting and rotor teeth pairing [15]. Other methods focusing only on the rotor have been compared in [16] and comprises of rotor pole-pairing, -notching, -chamfering and -skewing. Ultimately, the rotor pole-pairing was found to be the best choice.

2.3.2.10 Stator Iron, Copper and Proximity Losses

A few other areas such as stator iron losses, which should be low in the stator back-iron due to the short magnetic circuit [17], should be considered during the design phase. Low copper losses are found in FSPMs since, similar to Switched Reluctance machines, the concentrated windings employed reduce copper consumption and provides short end-windings [18]. Proximity losses consist of eddy current losses and the skin effect [19]. The high pole numbers in FSPM machines causes a high frequency and narrow stator slots, which results in high slot leakage across the coils and therefore, high eddy currents in the conductors [19]. It's been recommended that the diameter of the conductor should be determined by using the short circuit current at maximum frequency, since that maximum loss for uncontrolled conditions occur. By increasing the conductor strands, it allows for an increase in slot area utilization and packing factor, hence reducing the overall proximity losses [19]. An investigation conducted by [20] has shown that the eddy current losses in the PM are maximized at the ends of the PM, with the most on the inner end. The eddy current losses in the PM increases approximately squared as the speed increases. Two methods of reducing the eddy current loss are proposed by [20] and states that it can be achieved by removing some of the PM material near the ends and the other method

involves segmenting the PM. Both methods work well and while the reduction of PM material also slightly reduces the phase flux, the radial segmentation of the PM leaves the phase flux unaffected [20].

2.3.3 Summary of Optimal Dimensions and Ratios

Research in [21] found the optimum stator back-iron thickness, rotor pole width and split ratio to be $0.7\beta_s$, 1.4-1.6β_r and 0.55-0.6 respectively. Table 2.1 contains all the parameters that have been optimized by researchers. While these optimal dimensions and ratios do help with the design process, it is not necessarily the optimised design for all FSPM machines. Therefore, parametric studies and an optimization are essential.

Table 2.1: Summary of Optimized Parameters

Parameter	**Value**
Slot-fill-factor (K_{cu})	0.4
Stator/Rotor Configuration (N_s/N_r)	12/10 - 12/14 - 6/13
Split ratio (K_{sio})	0.5 - 0.6
Stator back-iron thickness (H_{ys})	$0.7\beta_s$
Rotor pole width (β_r)	$1.6H_{slot}$

2.4 Design Methods

Some design methods and sizing equations have been discussed in [17, 22], however, none of these methods provide a clear understanding to the designer. This may be because the researchers expect that this knowledge should be known for FSPM machine designers, however, for people unfamiliar with the FSPM machine and its topologies, the method proposed in this dissertation provides a clear understanding of the formulation of the important sizing equation.

2.5 Material Selection

The materials in question that need to be selected under careful consideration includes that of the permanent magnets and the laminations used for the stator and rotor cores. Since FSPM machines benefit from the flux focussing effect and doubly salient structure, laminations with a high saturation flux density should ideally be selected. The material

that will be used for both the stator and rotor cores is the M400-50A silicon steel and NdFeB35 rare earth magnets for excitation. The properties of both materials are summarized in Tables 2.2 and 2.3.

Table 2.2: Properties of M400-50A Silicone Steel

Parameter	**Value**	**Units**
Density	7.7	kg/dm^3
Resistivity	42	$\mu\Omega cm$
Yield Strength	305	N/mm^2
Tensile Strength	445	N/mm^2
Young's Modulas RD	200 000	N/mm^2
Young's Modulas TD	210 000	N/mm^2
Hardness HV5 (VPN)	160	-
Thickness	0.5	mm

Table 2.3: Properties of NdFeB35 Rare-earth Magnets

Parameter	**Value**	**Units**
Remanence flux density	1.17	mT
Coercivity	867	kA/m
Intrinsic Coercivity	955	kA/m
Maximum Energy Product	263	kJ/m^3
Maximum Temperature	80	Degree Celsius

Chapter 3

Electrical Drives

This chapter explores the benefits of using drives, compares multiple PMSG drive topologies and studies the operating principle of the drives. The emphasis of this research is on the development of the generator and in order to provide proper control, the drive is needed. Therefore, the drive development is not as in-depth and many formulae cited are taken from appropriate research.

3.1 Operating Principle

One of the main advantages of the FSPM machine is that it can be controlled like the PMSG. The FSPM machine can be uncontrolled like an independent generator or controlled by connecting it to a drive. The uncontrolled FSPM machine has loads directly connected to each phase, however, the chances of unbalanced phases are higher and the efficiency of the machine will be lower compared to the efficiency with a drive. This is where the drive plays a big role, by having machine- and grid-side converters to automatically control the flow of current in the armature windings.

3.1.1 Independent Generator

By following the understanding of electromagnetic induction, a current will be induced into a conductor when a voltage is applied. Therefore, the voltage vector across the load will depend on the type of load i.e. resistive, capacitive, inductive or a combination of the aforementioned. It simply reduces the electric circuit to a voltage supply, the armature winding impedance and the load impedance, which can be easily solved. This means that the selection of the loads will determine the magnitude of the flow of current and influence the power factor and output torque.

3.1.2 Electrical Drive Controlled

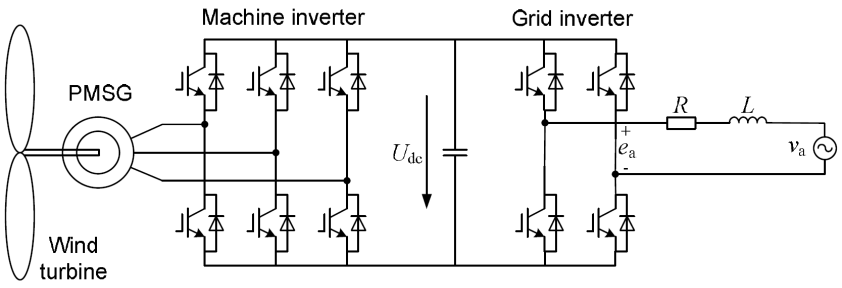

Figure 3.1: High-level overview of the machine- and grid-side converters [23]

The controlled drive scheme is much more complex than that of the independent generator. This is attributed to use of machine- and grid-side controllers as shown in Figure 3.1 and using the dq reference frame in certain control strategies.

3.2 Topologies

In [24], research has been conducted on the following strategies: Hysteresis Band Current Control, Voltage Oriented Control and the Flux Oriented Control. Whereas in [23], the more common Vector Oriented Control strategy has been investigated.

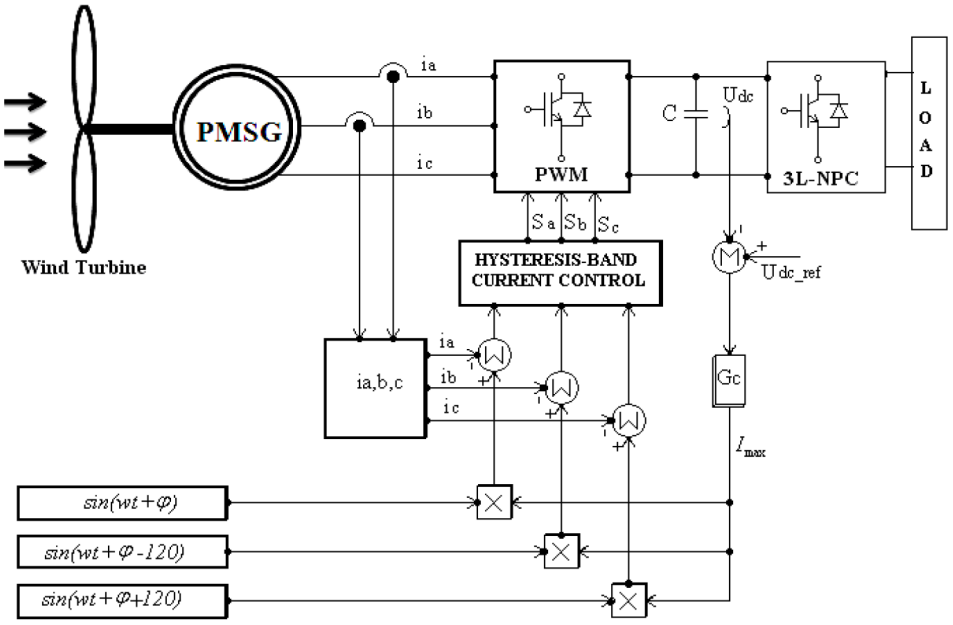

Figure 3.2: Hysteresis Band Current Control Strategy [24]

In Figure 3.2, the machine-side controller can use a hysteresis current controller to control the current that will be induced in the armature windings. However, due to the sinusoidal behaviour of Alternating Current (AC) signals, it would be difficult to control, therefore, the AC signals are converted from the abc/synchronous reference frame to the dq reference frame.

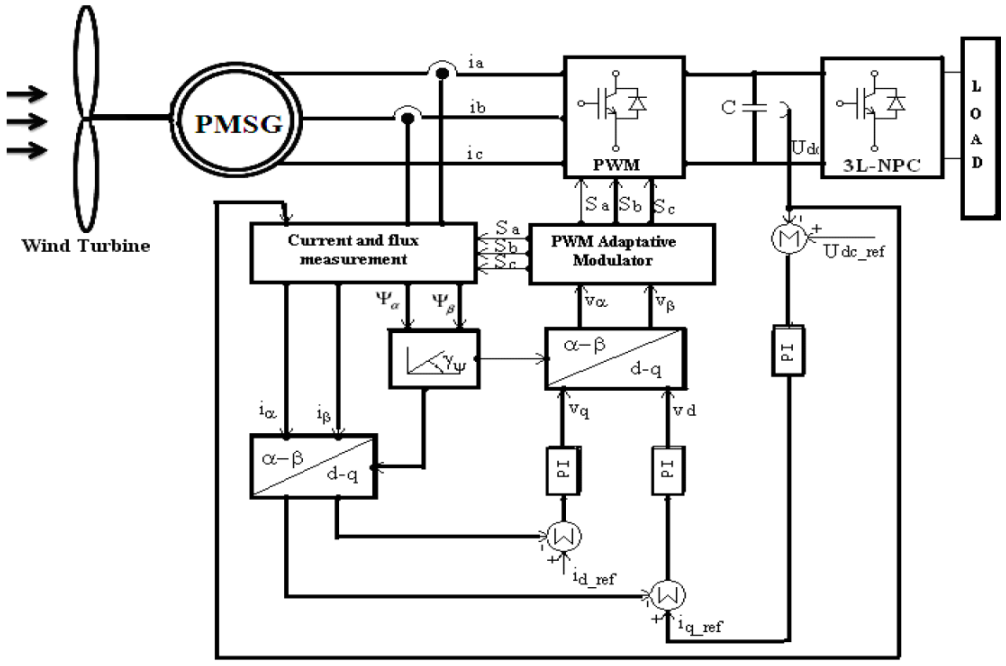

Figure 3.3: Field Oriented Control Strategy [24]

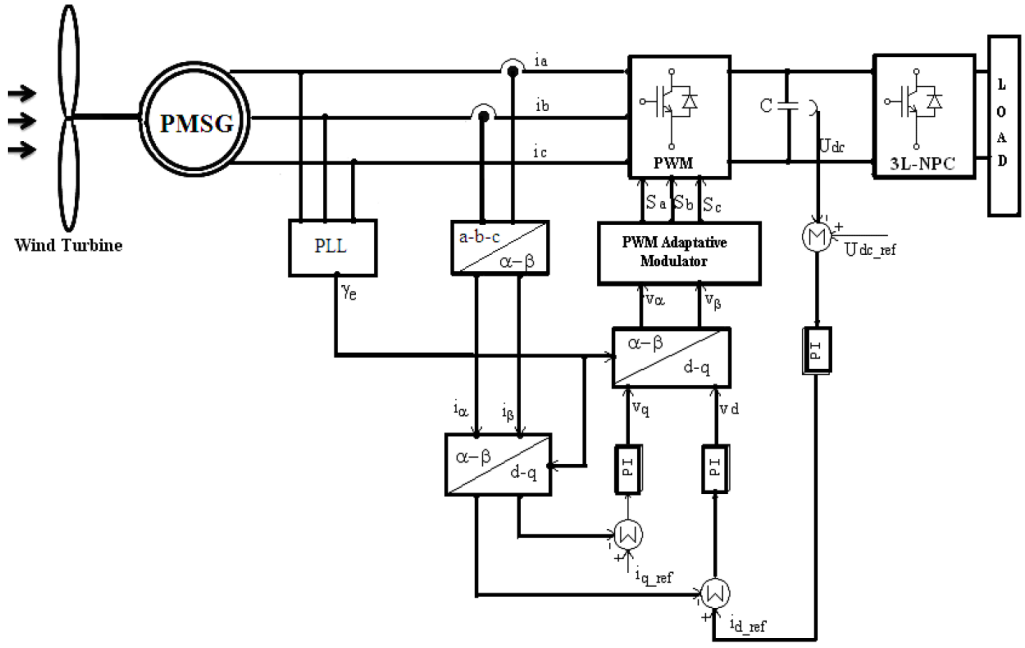

Figure 3.4: Voltage Oriented Control Scheme [24]

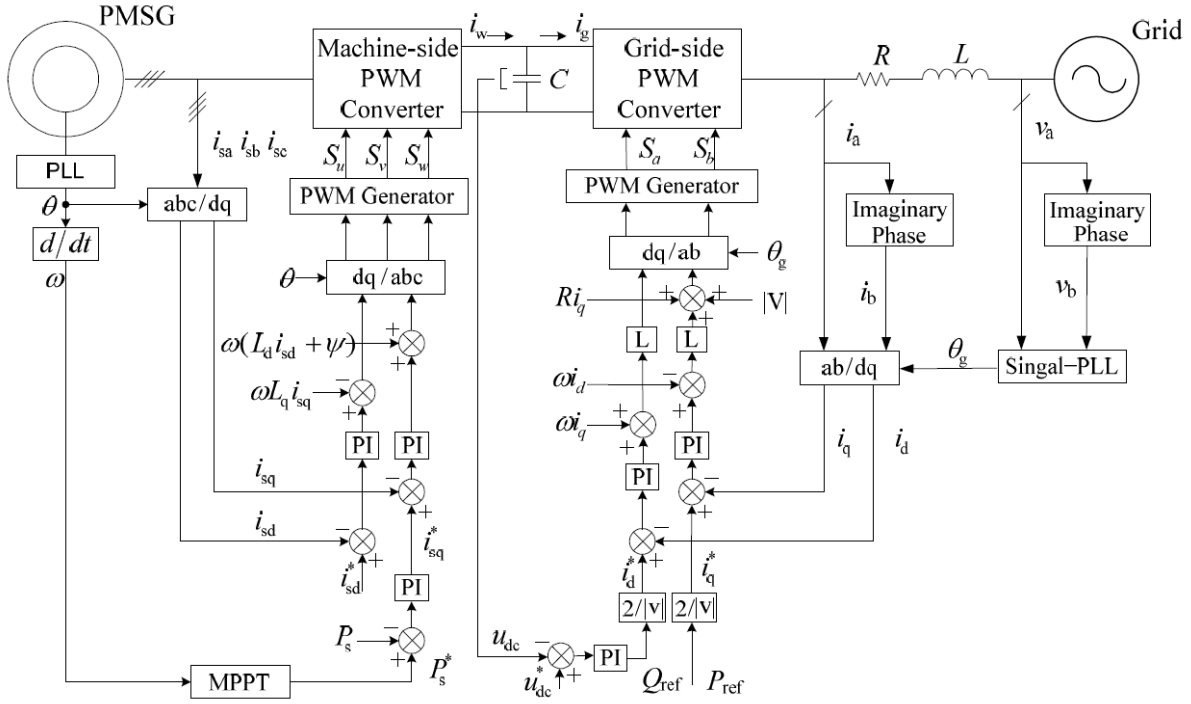

Figure 3.5: Vector Oriented Control Scheme [23]

By using the Vector Oriented Control Scheme in Figure 3.5, the dq reference frame converts the AC signals into DC, simplifying the control techniques to be used. To ensure that the maximum power is drawn from the machine at the lowest possible armature current, the I_d current reference should be set to zero. The I_q current reference will then be automatically changed by the controllers.

The grid-side converter also uses a vector orientated control scheme and in this case, the aim is to achieve a unity power factor. In order to achieve the unity power factor, the I_q current reference is set to zero, whereas the I_d current reference will then be automatically changed by the controllers.

The drive that will be investigated is the Vector Oriented scheme with $i_d = 0$ control and only the machine-side converter and its controllers will be developed, along with the dc-link capacitor selection. Since the grid-side converter won't be developed, the voltage across the dc-link capacitor and therefore, the loads, won't be controlled.

3.3 Reference Frame Conversions

A vector control strategy using Space Vector Pulse Width Modulation (SVPWM) has been proposed in [25]. A commercial controller developed in [26] discusses its operation and will reduce the development time involved of the drive.

From Figure 3.5, the current signals are converted from the abc to the dq reference frame. In order to do this, the abc signals have to be converted to the $\alpha\beta$ reference frame by using the Clarke Transformation [26]:

$$\begin{bmatrix} I_\alpha \\ I_\beta \end{bmatrix} = \begin{bmatrix} 1 & 0 \\ \frac{1}{\sqrt{3}} & \frac{2}{\sqrt{3}} \end{bmatrix} \begin{bmatrix} I_a \\ I_b \end{bmatrix} \tag{3.1}$$

To convert the current from the $\alpha\beta$ to the dq reference frame, the Park Transformation [26] has to be used:

$$\begin{bmatrix} I_d \\ I_q \end{bmatrix} = \begin{bmatrix} cos(\theta) & sin(\theta) \\ -sin(\theta) & cos(\theta) \end{bmatrix} \begin{bmatrix} I_\alpha \\ I_\beta \end{bmatrix} \tag{3.2}$$

These reference frames can be compared to each other:

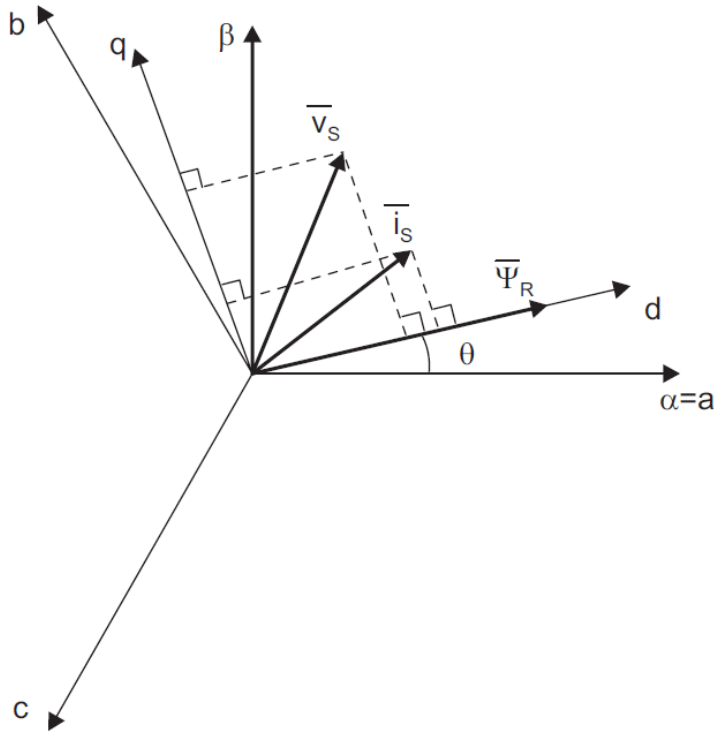

Figure 3.6: Comparison of the abc to the $\alpha\beta$ and dq reference frames [26]

From Figure 3.6, the following formulae for the total voltage and current in terms of the dq reference frame are derived:

$$I_s = \sqrt{I_d^2 + I_q^2} \tag{3.3}$$

$$V_s = \sqrt{V_d^2 + V_q^2} \tag{3.4}$$

The d- and q-axis currents can be found from the phase rms current by means of [27]:

$$I_d = \sqrt{2} I_{rms} sin(\alpha) \tag{3.5}$$

$$I_q = \sqrt{2} I_{rms} cos(\alpha) \tag{3.6}$$

3.4 Electromagnetic Modelling of a PM Machine

The modelling of an FSPM machine for control purposes involves transformations to the dq reference frame in order to control the dq signals. The dq equivalent electromagnetic torque [8, 18, 27–30], flux linkages and voltages are described in [24, 25, 31–33] as:

$$T_{em} = \frac{3}{2} N_r [\lambda_m I_q + (L_d - L_q) I_d I_q] \tag{3.7}$$

$$\begin{cases} \lambda_d = \lambda_m + L_d I_d \\ \lambda_q = L_q I_q \end{cases} \tag{3.8}$$

$$\begin{cases} V_d = \omega_e L_q I_q - R_{ph} I_d \\ V_q = \omega_e \lambda_m - \omega_e L_d I_d - R_{ph} I_q \end{cases} \tag{3.9}$$

It's clear that by forcing $I_d = 0$, the total electromagnetic torque can be solely controlled by I_q [8, 12, 34, 35]:

$$T_{em} = \frac{3}{2} N_r \lambda_m I_q \tag{3.10}$$

Lastly, the real and reactive output power and the power factor are determined from [31, 32]:

$$P_{out} = \frac{3}{2} (V_d I_d + V_q I_q) \tag{3.11}$$

$$Q_{out} = \frac{3}{2} (V_q I_d - V_d I_q) \tag{3.12}$$

$$PF = cos\left(\tan^{-1}\left(\frac{I_d}{I_q}\right) + \tan^{-1}\left(\frac{v_d}{v_q}\right)\right) \tag{3.13}$$

An analytical comparison with the FEA results for the self inductance in the dq reference frame have been discussed in [30]:

$$L_d = \frac{V_{d(pk-pk)}}{2\pi f_e I_{d(pk-pk)}} \tag{3.14}$$

$$L_q = \frac{V_{q(pk-pk)}}{2\pi f_e I_{q(pk-pk)}} \tag{3.15}$$

Chapter 4

Development of the FSPM Machine

The following chapter elaborates on the understanding in developing analytical equations that describes how the back-EMF, current and ultimately, the output power in an FSPM machine is developed.

The general power equation of an m-phase machine that's current controlled is described by [36], where ε is the ratio of back-EMF to full-load terminal voltage:

$$P_{out} = mV_{t_{rms}}I_{rms}cos(\theta) = m\frac{E_{rms}}{\varepsilon}I_{rms}cos(\theta) \tag{4.1}$$

4.1 Geometrical Data

The geometry of FSPM machines are important for understanding how and why the formulae were formulated.

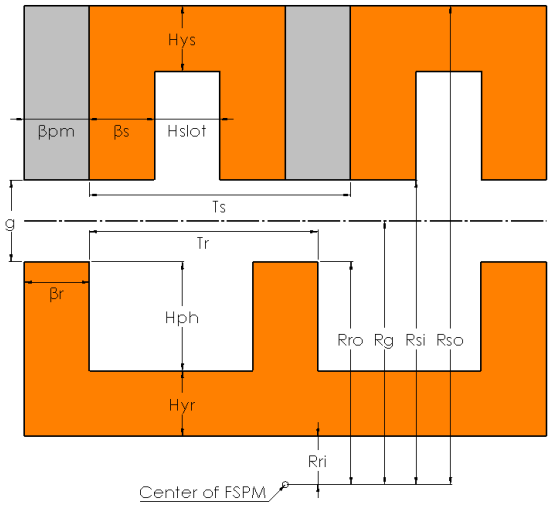

Figure 4.1: Geometry of conventional FSPM machine with labels

4.2 Back-EMF

In (4.1) above, the back-EMF can be derived by the physics principles of electromagnetic induction. From Lenz's law, the induced voltage is:

$$E = -\frac{d\phi}{dt} \tag{4.2}$$

Where ϕ is the flux. For a coil with an N-number of turns, (4.2) can be amended and forms Faraday's law:

$$E = -N_t\frac{d\phi}{dt} \tag{4.3}$$

During machine designing there are a lot of parameters the designer specifies to which he/she designs. For this particular section, the values of the current density, specific electric loading and slot-fill factor are chosen by the designer. However, these values affect each other and ultimately, the number of winding turns per phase. In order to satisfy all the conditions, these three parameters are used concurrently to determine the number of winding turns per phase that would realistically fit into the slot area.

4.2.1 Winding Turns Per Phase

The slot-fill factor is the ratio of copper to slot area:

$$K_{cu} = \frac{A_c}{A_{slot}} \tag{4.4}$$

The total area of copper in a slot can be found by multiplying the number of turns per phase with the area of a single conductor and then dividing by the number of stator poles per phase. Lastly, it gets multiplied by two to account for the turns on the adjacent stator poles:

$$A_c = \frac{2aN_tm}{N_s} \tag{4.5}$$

Calculating the slot area is a slightly longer process and reference is made to Figure 4.1. Firstly, the stator area is split between the back-iron and poles. The back-iron area is given by:

$$A_1 = \pi(R_{so})^2 - \pi(R_{so} - H_{ys})^2 \tag{4.6}$$

Next the stator pole area is calculated by:

$$A_2 = 3\beta_s(R_{so} - R_{si} - H_{ys}) \tag{4.7}$$

The total stator area is therefore the summation of A_1 with the number of stator poles times A_2:

$$A_{stator} = A_1 + N_s A_2 \tag{4.8}$$

The singular stator slot area is derived by subtracting the inner stator and total stator area from the outer stator area, and then dividing it by the number of stator poles:

$$A_{slot} = \frac{\pi(R_{so})^2 - \pi(R_{si})^2 - A_{stator}}{N_s} \tag{4.9}$$

After substituting (4.5) into (4.4) the number of winding turns per phase can be calculated based on the desired slot-fill factor:

$$N_t = \frac{K_{cu} N_s A_{slot}}{2am} \tag{4.10}$$

4.2.2 Flux

The flux can be described as the flux density multiplied by the area where that flux is flowing through. The flux density is not uniform through the given stator tooth area, therefore, the peak air-gap flux density is used in these derivations in order to establish the peak back-EMF equation. A cosine term is added since the overlapping stator and rotor tooth area is frequency dependant and maximum when they're in-line e.g cos(0). The flux is written as:

$$\phi = K_d B_{peak} A cos(\omega_e t) \tag{4.11}$$

The flux leakage factor is derived mathematically by using the measured field parameters and solving for K_d in (4.20).

The area of a stator tooth is the stack length, multiplied by the tooth width:

$$A = l_{st}\beta_s \tag{4.12}$$

The stator tooth width is defined as the stator pole pitch, multiplied by the tooth width to pole pitch factor. Note that the tooth width to pole pitch factor, C_s, for conventional

and c-core FSPM machines is what causes the difference in topology. This factor is 1/4 and 1/8 for conventional and c-core FSPM machines respectively:

$$\beta_s = T_s C_s \tag{4.13}$$

The stator pole pitch is the arc-length from one stator pole to an adjacent pole, based on the inner radius of the stator:

$$T_s = \frac{2\pi R_{si}}{N_s} = \frac{\pi D_{si}}{N_s} \tag{4.14}$$

After substituting (4.12) to (4.14) into (4.11), the flux equals:

$$\phi = \frac{K_d B_{peak} l_{st} \pi D_{si} C_s cos(\omega_e t)}{N_s} \tag{4.15}$$

4.2.3 Final Back-EMF Equation

Substituting (4.15) into (4.3) yields:

$$E = \frac{-N_t K_d B_{peak} l_{st} \pi D_{si} C_s}{N_s} \frac{dcos(\omega_e t)}{dt} \tag{4.16}$$

By solving the differential and taking the absolute of (4.16), the maximum back-EMF becomes:

$$E_{peak} = \frac{N_t K_d B_{peak} l_{st} \pi D_{si} C_s \omega_e}{N_s} \tag{4.17}$$

The angular frequency equals 2πf with units in rad/sec. The electrical frequency, f, is determined by the multiplication of the rotor speed and pole number [4, 8, 10, 12, 27, 29, 32, 37–40]. Since the rotor speed is given in rpm, it must be divided by 60 to convert it to rps:

$$\omega_e = 2\pi \frac{N_r n_r}{60} \tag{4.18}$$

The final peak back-EMF equation equals:

$$E_{peak} = \frac{N_t K_d B_{peak} l_{st} \pi^2 D_{si} C_s N_r n_r}{30 N_s} \tag{4.19}$$

The rms back-EMF can therefore be described by dividing the peak back-EMF by $\sqrt{2}$:

$$E_{rms} = \frac{N_t K_d B_{peak} l_{st} \pi^2 D_{si} C_s N_r n_r}{30\sqrt{2} N_s} \tag{4.20}$$

4.3 Magnetic Circuit Modelling

The magnetic circuit model will be used to determine the flux density at the rated condition for the FSPM machine. This model is similar to that of an electric circuit, however, for magnetic circuits to make it easier to understand. The comparison between electrical and magnetic circuit elements are shown in Table 4.1 [41].

Table 4.1: Comparison between electrical and magnetic circuit elements

Electrical Circuit	**Magnetic Circuit**
Voltage	Magneto-motive Force (MMF)
Current	Flux
Resistance	Reluctance

The development of a lumped parameter model for a FSPM machine in [22] includes fringing effects, enabling this model to be more accurate in determining the flux in the respective geometrical parts. This allows for an analytical method to produce an estimate of the flux density in the stator teeth and ultimately, a full analytical approximation of the FSPM machine's back-EMF. As will be seen, this analytical approximation of the flux density establishes the reasons why the dimensions of the rotor geometry and air-gap length affect the electromagnetic torque/output power of the generator.

The laws of Ohm and Kirchoff for electrical circuits can be applied in a similar fashion to magnetic circuits. The lumped parameter model works by segmenting the stator, rotor, PMs and air-gap into permeances, whereby nodal analysis is used to determine the flux at each node as illustrated in [22, 34]. The flux can finally be used to determine the flux density in the stator teeth.

From general magnetic circuit design theory, the flux density is defined by the flux per unit area:

$$B_T = \frac{\phi}{S} \tag{4.21}$$

The magneto-motive force is given by the number of winding turns multiplied by the

current in the conductor, however, for this application, there's no electromagnets, only permanent magnets. Therefore, the MMF for the PMs is derived from [22, 34] which is partly dependent on the magnetic properties:

$$F_{pm} = \frac{l_a B_a}{\mu_{pm}\mu_0} \tag{4.22}$$

For a PM, there's a specific flux density associated with it, called the remanence flux density. Since temperature affects this value, the operating temperature must be specified and the new remanence flux density at ambient temperature for the PM can thus be calculated by [22]:

$$B_a = B_R(1 + K_{pm}(T_1 - T_0)) \tag{4.23}$$

The reluctance of the iron parts are calculated by dividing the flux path length with the multiplication of the material's permeability with the cross sectional area [22, 34, 42]:

$$R = \frac{L}{\mu_r \mu_0 S} \tag{4.24}$$

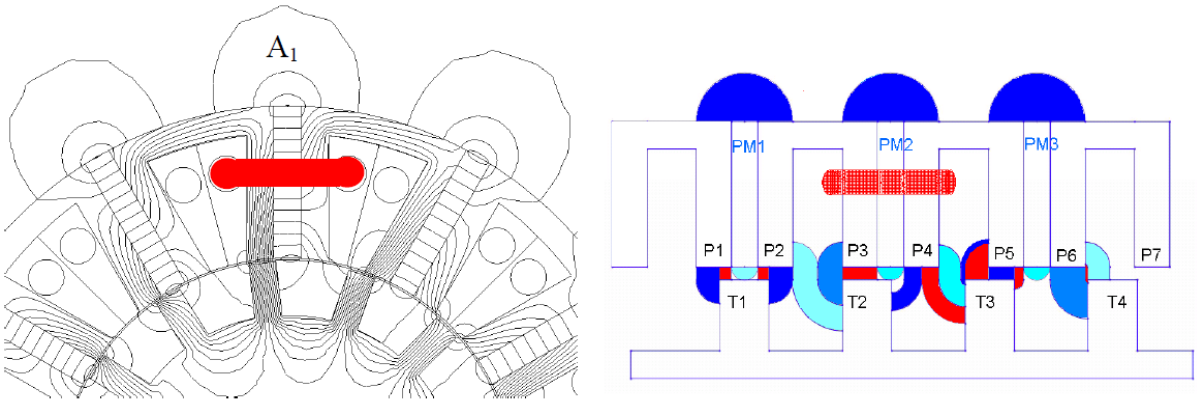

Figure 4.2: a) Flux lines contributing to the stator pole in its aligned position with the b) approximate air-gap leakage flux paths [22]

The determination of the air-gap reluctances are slightly different since the flux leakage is taken into account. In order to determine the reluctance of these individual flux leakage paths, reference is made to Figure 4.2b and Figure 4.3.

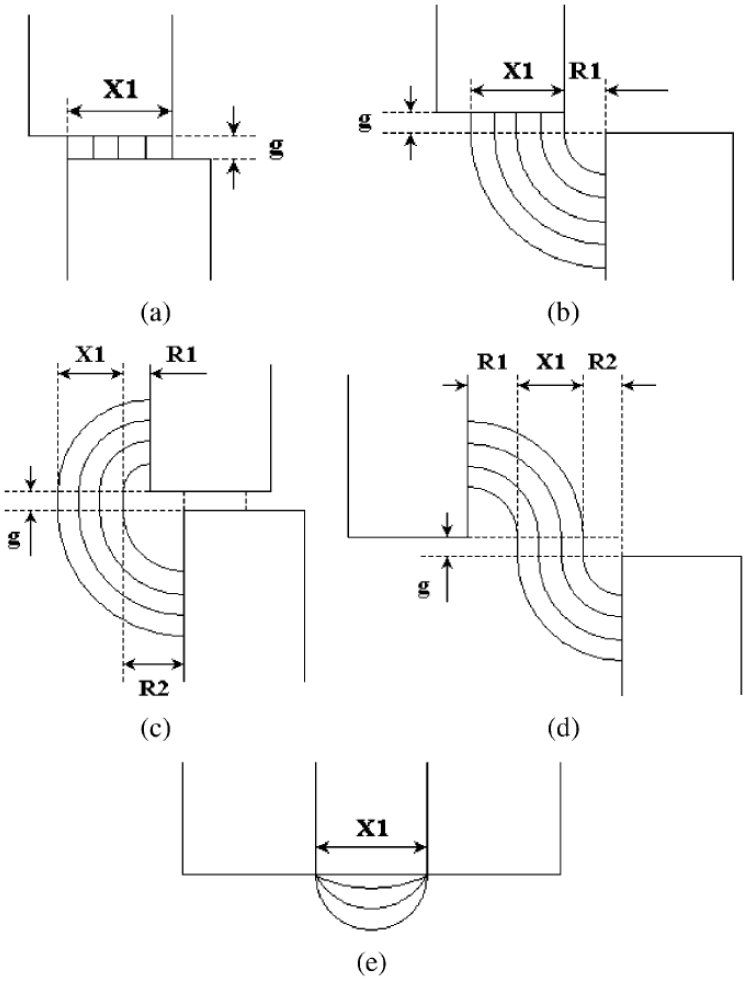

Figure 4.3: Air-gap leakage flux path approximates [34]

The air-gap reluctances can therefore be approximated as indicated in Figure 4.3 [34]:

$$
\begin{aligned}
(a) \qquad & R_a = \frac{g}{\mu_0 l_{st} X_1} \\
(b) \qquad & R_b = \frac{\pi ln(1 + \frac{\pi X_1}{\pi R_1 + 2g})}{2\mu_0 l_{st}} \\
(c) \qquad & R_c = \frac{\pi ln(1 + \frac{2\pi X_1}{\pi (R_1 + R_2) + 2g})}{\mu_0 l_{st}} \\
(d) \qquad & R_d = 2g + \frac{\pi (R_1 + R_2 + X_1)}{2\mu_0 l_{st} X_1} \\
(e) \qquad & R_e = \frac{1}{0.26\mu_0 l_{st}}
\end{aligned}
\tag{4.25}
$$

From Figure 4.3 and the equations in (4.25), it's clear that the magnetic circuit modelling can only be used for analyses after the FEA results have been obtained, since the air-gap reluctances' parameters are unknown from an analytical point of view. It's only

necessary to model three stator poles for the lumped parameter model, since, as seen in Figure 4.2a, the flux lines that contribute to the induced voltage of the coil in its aligned position, is only from the stator poles surrounding the aligned one. By closely observing the flow of these flux lines, it's clear that only three PMs are contributing to flux in the middle stator pole.

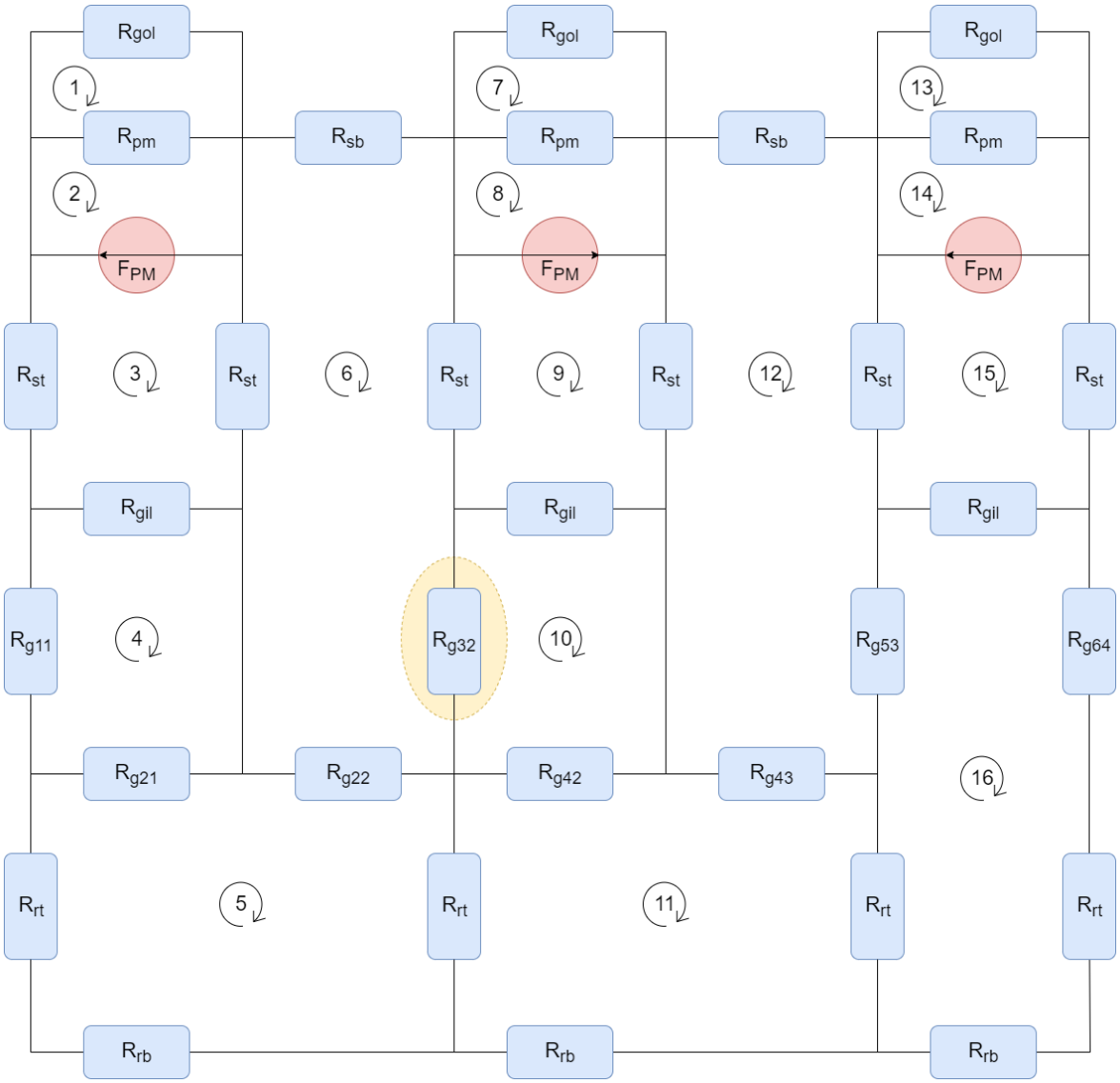

Figure 4.4: Magnetic circuit model using reluctances, MMF and flux [22]

The magnetic circuit model in Figure 4.4 is analysed by using mesh analyses. This requires the formulation of 16 equations in order to determine the flux in the desired air-gap, which is highlighted in yellow.

The equations in (4.26) are derived from Figure 4.4.

$$
\begin{aligned}
(1)\quad & 0 = \phi_1(-R_{pm} - R_{gol}) + \phi_2(R_{pm}) \\
(2)\quad & F_{pm} = \phi_1(-R_{pm}) + \phi_2(R_{pm}) \\
(3)\quad & F_{pm} = \phi_3(-2R_{st} - R_{gil}) + \phi_4(R_{gil}) + \phi_6(R_{st}) \\
(4)\quad & 0 = \phi_3(R_{gil}) + \phi_4(-R_{g11} - R_{gil} - R_{g21}) + \phi_5(R_{g21}) \\
(5)\quad & 0 = \phi_4(R_{g21}) + \phi_5(-2R_{rt} - R_{g21} - R_{g22} - R_{rb}) + \phi_6(R_{g22}) + \phi_{11}(R_{rt}) \\
(6)\quad & 0 = \phi_3(R_{st}) + \phi_5(R_{g22}) + \phi_6(-R_{sb} - 2R_{st} - R_{g32} - R_{g22}) + \phi_9(R_{st}) + \phi_{10}(R_{g32}) \\
(7)\quad & 0 = \phi_7(-R_{pm} - R_{gol}) + \phi_8(R_{pm}) \\
(8)\quad & F_{pm} = \phi_7(R_{pm}) + \phi_8(-R_{pm}) \\
(9)\quad & F_{pm} = \phi_6(-R_{st}) + \phi_9(2R_{st} + R_{gil}) + \phi_{10}(-R_{gil}) + \phi_{12}(-R_{st}) \\
(10)\quad & 0 = \phi_6(R_{g32}) + \phi_9(R_{gil}) + \phi_{10}(-R_{g32} - R_{gil} - R_{g42}) + \phi_{11}(R_{g42}) \\
(11)\quad & 0 = \phi_5(R_{rt}) + \phi_{10}(R_{g42}) + \phi_{11}(-2R_{rt} - R_{rb} - R_{g42} - R_{g43}) + \phi_{12}(R_{g43}) + \phi_{16}(R_{rt}) \\
(12)\quad & 0 = \phi_9(R_{st}) + \phi_{11}(R_{g43}) + \phi_{12}(-R_{sb} - R_{g43} - 2R_{st} - R_{g53}) + \phi_{15}(R_{st}) + \phi_{16}(R_{g53}) \\
(13)\quad & 0 = \phi_{13}(-R_{pm} - R_{gol}) + \phi_{14}(R_{pm}) \\
(14)\quad & F_{pm} = \phi_{13}(-R_{pm}) + \phi_{14}(R_{pm}) \\
(15)\quad & F_{pm} = \phi_{12}(R_{st}) + \phi_{15}(-2R_{st} - R_{gil}) + \phi_{16}(R_{gil}) \\
(16)\quad & 0 = \phi_{11}(R_{rt}) + \phi_{12}(R_{g53}) + \phi_{15}(R_{gil} + \phi_{16}(-2R_{rt} - R_{rb} - R_{g53} - R_{g64} - R_{gil})
\end{aligned}
\tag{4.26}
$$

To determine the flux density in the air-gap, ϕ_6 and ϕ_{10} needs to be computed. To simplify the computation process, the equations in (4.26) are written in matrix form:

$$
\begin{bmatrix} F_1 \\ F_2 \\ \vdots \\ F_{16} \end{bmatrix} = \begin{bmatrix} R_{1,1} & R_{1,2} & R_{1,3} & \dots & R_{1,16} \\ R_{2,1} & R_{2,2} & R_{2,3} & \dots & R_{2,16} \\ \vdots & \vdots & \vdots & \ddots & \vdots \\ R_{16,1} & R_{16,2} & R_{16,3} & \dots & R_{16,16} \end{bmatrix} \begin{bmatrix} \phi_1 \\ \phi_2 \\ \vdots \\ \phi_{16} \end{bmatrix} \tag{4.27}
$$

To calculate ϕ_6, substitute column 6 in the original R-matrix with the F-matrix and take its determinant:

$$
\det R(:,6) = \begin{vmatrix} R_{1,1} & \dots & R_{1,5} & F_1 & R_{1,7} & \dots & R_{1,16} \\ R_{2,1} & \dots & R_{2,5} & F_2 & R_{1,7} & \dots & R_{2,16} \\ \vdots & \ddots & \vdots & \vdots & \vdots & \ddots & \vdots \\ R_{16,1} & \dots & R_{16,5} & F_{16} & R_{16,7} & \dots & R_{16,16} \end{vmatrix} \tag{4.28}
$$

Then, divide by the determinant of the original R-matrix:

$$\phi_6 = \frac{\begin{vmatrix} R_{1,1} & \dots & R_{1,5} & F_1 & R_{1,7} & \dots & R_{1,16} \\ R_{2,1} & \dots & R_{2,5} & F_2 & R_{1,7} & \dots & R_{2,16} \\ \vdots & \ddots & \vdots & \vdots & \vdots & \ddots & \vdots \\ R_{16,1} & \dots & R_{16,5} & F_{16} & R_{16,7} & \dots & R_{16,16} \end{vmatrix}}{\begin{vmatrix} R_{1,1} & R_{1,2} & R_{1,3} & \dots & R_{1,16} \\ R_{2,1} & R_{2,2} & R_{2,3} & \dots & R_{2,16} \\ \vdots & \vdots & \vdots & \ddots & \vdots \\ R_{16,1} & R_{16,2} & R_{16,3} & \dots & R_{16,16} \end{vmatrix}} \tag{4.29}$$

Repeat this process for ϕ_{10}, but by substituting column 10 with the F-matrix. Once the two calculations have been completed, subtract the two values to find the direction and resultant flux value in the air-gap:

$$\phi_{g32} = |\phi_{10} - \phi_6| \tag{4.30}$$

The flux density in the air-gap can therefore be calculated by (4.21) since the flux and the area of the air-gap are both known.

4.4 Induced Current

It is important to understand how the machine is going to be controlled, as this affects how the simulations will be performed and the induced currents are generated. There are two general methods of controlling generators: (1) as an independent generator and by (2) connecting it to the grid. For this research, the FSPM machine is controlled by using the machine-side controller before connecting it to a load. The chosen current density will affect the value of the specific electric loading. For this reason, the specific electric loading can be formulated. To do this, it is important to understand the current formula. Based on [7, 17, 43, 44], the specific electric loading is determined by the total armature ampere conductors divided by the armature periphery at the air-gap:

$$A_s = \frac{I_{rms} Z}{\pi D_g} \tag{4.31}$$

Z is the total number of armature conductors and can be determined by multiplying the number of phases by twice the number of turns per phase to account for conductors in a

slot from a 2D perspective:

$$Z = 2mN_t \tag{4.32}$$

By going a step further, the current density is the ratio of Root Mean Square (RMS) current flowing through a conductor to its area:

$$J_s = \frac{I_{rms}}{a} \tag{4.33}$$

After rearranging and substituting (4.33, 4.32) into (4.31), the specific electric loading is determined by:

$$A_s = \frac{2maN_tJ_s}{\pi D_g} \tag{4.34}$$

Note that in order to make I_{rms} the subject of (4.34), rearrange (4.33) and replace aJ_s in (4.34) with I_{rms}:

$$I_{rms} = \frac{A_s\pi D_g}{2mN_t} \tag{4.35}$$

4.5 Losses

The total losses in a PM machine results from a combination of copper, core, windage and friction losses. For simplicity, only the copper and core losses are derived in this dissertation. The core losses are more in-depth and discussed in Chapter 8.

The copper losses in an m-phase machine are described by:

$$P_{cu} = m{I_{rms}}^2R_{ph} \tag{4.36}$$

Copper losses are generically associated with the resistance of a conductor and is derived from:

$$R_{ph} = \frac{\rho l_{ph}}{a} \tag{4.37}$$

The cross sectional shape of the stator poles are in fact rectangular and by assuming that the phase windings are wound rectangularly, the length of a single coil can be derived. This means that it is simply the circumference of the stator pole multiplied by the number of turns:

$$l_{ph} = 2(l_{st} + 3\beta_s)N_t \tag{4.38}$$

The cross sectional area of the conductor is simply:

$$a = \pi {r_{ph}}^2 \tag{4.39}$$

After substituting (4.13, 4.14, 4.38, 4.39) into (4.37), the winding resistance can be expressed as:

$$R_{ph} = \frac{2\rho(l_{st} + \frac{3\pi D_{si} C_s}{N_s})N_t}{\pi {r_{ph}}^2} \tag{4.40}$$

By substituting (4.40) into (4.36), the total copper losses is expressed as:

$$P_{cu} = m {I_{rms}}^2 \frac{2\rho(l_{st} + \frac{3\pi D_{si} C_s}{N_s})N_t}{\pi {r_{ph}}^2} \tag{4.41}$$

Based on the losses described, an approximation of the total losses in an FSPM machine is the summation of the copper and core losses.

$$P_{loss} = P_{cu} + P_c = m {I_{rms}}^2 \frac{2\rho(l_{st} + \frac{3\pi D_{si} C_s}{N_s})N_t}{\pi {r_{ph}}^2} + P_c \tag{4.42}$$

4.6 Sizing Equation

Substituting the back-EMF (4.20) and current (4.35) equations into (4.1) yields the following output power equation:

$$P_{out} = \frac{K_d B_{peak} l_{st} \pi^3 D_{si} C_s N_r n_r A_s D_g cos(\theta)}{20\sqrt{2} m \varepsilon N_s} \tag{4.43}$$

To make the sizing equation more relatable to those find in other research, parameters such as the split ratio and aspect ratio are defined and substituted into (4.43). The split ratio is defined as the ratio of the stator inner to outer diameter:

$$K_{sio} = \frac{D_{si}}{D_{so}} \tag{4.44}$$

The aspect ratio is defined as the ratio of the effective stack length to stator inner diameter:

$$K_l = \frac{l_{st}}{D_{si}} \tag{4.45}$$

To simplify the power equation, $D_g \approx D_{si}$. Substituting this approximation and (4.44, 4.45) into (4.43), and making D_{so} the subject of the new formula, the final sizing equation is obtained:

$$D_{so} = \sqrt[3]{\frac{20\sqrt{2}m\varepsilon P_{out}N_s}{K_d B_{peak}\pi^3 K_{sio}^3 C_s N_r n_r A_s cos(\theta)}} \tag{4.46}$$

4.7 Winding Configurations

The winding configurations of FSPM machines are extremely important as it affects the maximum achievable back-EMF and if the magnetic forces will be balanced. As defined in (2.5), the electrical degrees of FSPM machines is simply the mechanical degrees multiplied by the number of rotor poles. The mechanical displacement between adjacent stator poles is simply:

$$\alpha_m = \frac{360^\circ}{N_s} \tag{4.47}$$

The phase windings are split into opposite sectors. For an odd number of phases including two-phases, each sector is determined by dividing 360° with twice the number of phases. For an even number of phase excluding two-phases, a single sector is determined by dividing 360° with the number of phases [12]:

$$\alpha_{sector} = \begin{cases} \frac{360^\circ}{2m}, & m = odd, m = 2 \\ \frac{360^\circ}{m}, & m = even, m \neq 2 \end{cases} \tag{4.48}$$

For both the even- and odd-phase number selection, the sectors for their remaining phases are rotated by [12]:

$$\alpha_{sector} = \frac{360^\circ n}{m}, \quad n = 1, 2, ..., m-1 \tag{4.49}$$

A derivation of the 12/14 FSPM machine's winding configurations is performed to show the understanding behind it. The electrical degrees, as defined by (2.5), is:

$$\alpha_e = \frac{360^\circ N_r}{N_s} = 420^\circ \tag{4.50}$$

This value should be -90° $< \alpha_e <$ 90°, therefore, subtract $360k_3$°, $k_3 \in N^0$ from it until the condition is satisfied. This leads to $\alpha_e = 60^\circ$. Since we have 12 stator poles and the PMs for FSPM machines are magnetized with alternating adjacent north and south combinations, this can be seen in Figure 4.5 below:

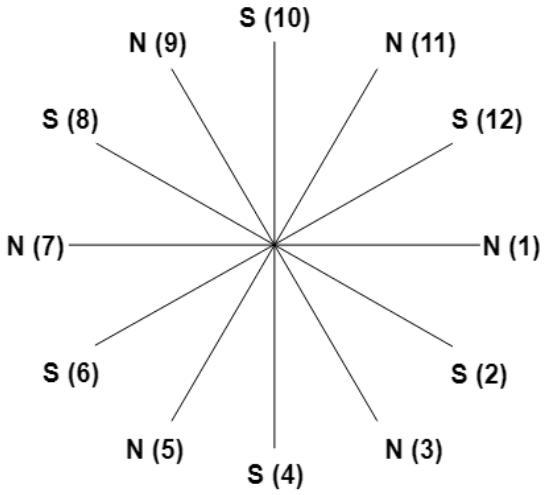

Figure 4.5: PM magnetization direction and pole number for a 12 stator slot FSPM

Since the electrical degrees is 60°, the individual coil EMF vectors will be separated by 60° as shown in Figure 4.6 below. Note that for positive and negative electrical degree angles, the direction of the coils are anticlockwise and clockwise respectively.

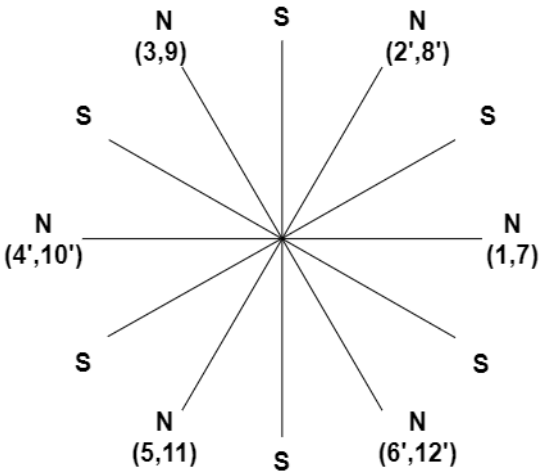

Figure 4.6: Coil EMF vectors for a 12/14 FSPM

The coil EMF vectors shown in Figure 4.6 clearly shows that since the magnetization direction of the PMs for coils 2, 4, 6, 8, 10 and 12 are opposite to coils 1, 3, 5, 7, 9 and 11. Calculating the sector angle from (4.48) yields:

$$\alpha_{sector} = \frac{360^\circ}{2m} = 60^\circ \tag{4.51}$$

This is visually shown in Figure 4.7. The sector only encloses coils 1, 7, 4 and 10 for phase A. Note that the sectors are in the direction of ascending coil numbers.

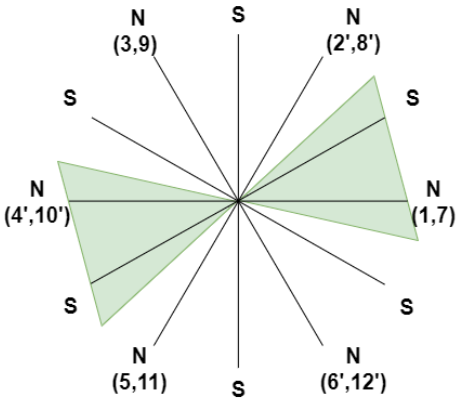

Figure 4.7: Sectors indicated by green area for a 12/14 FSPM

To separate these coil EMF vectors into the individual phases, the vectors in the diagram can simply be rearranged, with opposite polarized coils flipped by 180 electrical degrees as shown in Figure 4.8. For a balanced three phase machine, phases B and C are +120 and -120 electrical degrees respectively displaced from phase A. As indicated in Figure 4.8, the coils are wound in the same direction to ensure that the series connected phase windings conduct in the same direction. For cases where the coils are wound in opposite directions, an apostrophe will be used as an indication.

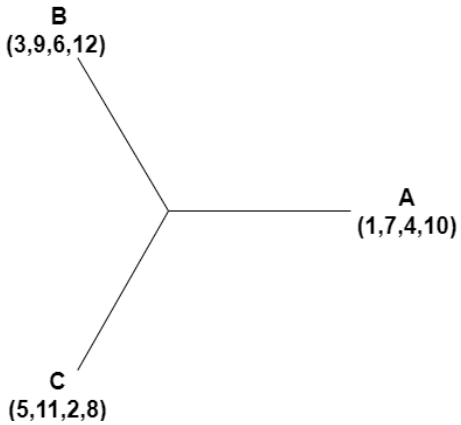

Figure 4.8: Coil EMF vectors for a 12/14 FSPM grouped by phase

4.8 Cogging Torque

As mentioned in Chapter 1, cogging torque is unwanted for generators and the aim is to minimize it as much as possible. Cogging torque is given by the change in the magnetic field energy with respect to the rotor's mechanical position [16, 45–51]:

$$T_{cog} = -\frac{\partial W_c}{\partial \theta} \tag{4.52}$$

In its most fundamental form, cogging torque is derived in [28, 48, 52] as:

$$T_{cog} = -\frac{1}{2}\phi_{ag}^2 \frac{\partial R_{ag}}{\partial \theta} \tag{4.53}$$

It's indicated in (4.53) that the cogging torque is dependant on the air-gap flux and the rate of change of the air-gap reluctance with respect to the rotor's position. This explains why cogging torque reduction techniques include reducing the PM material, which significantly reduces the cogging torque, as it's reducing the air-gap flux and it's a squared multiple. Other techniques related to pole shaping and skewing are effectively aimed at reducing the change of air-gap reluctance, which is inherently high due to the saliency of the rotor poles.

The number of cogging torque periods is determined by dividing the number of stator poles with the highest common factor between the rotor and stator pole number [15, 28, 46, 53, 54]:

$$N_{cog} = \frac{N_s}{HCF(N_s, N_r)} \tag{4.54}$$

Furthermore, the mechanical angle corresponding to each cogging torque period is derived as [15, 46, 53, 54]:

$$\alpha_{cog} = \frac{360^\circ}{N_{cog} N_s} \tag{4.55}$$

Chapter 5

Initial FSPM Machine Design

This chapter is an in-depth application of the theory developed in the earlier chapters. Scripts were developed to assist with the analytical design, by plotting thousands of combinations that easily show the designer which initial machine dimensions to choose in order to meet the desired rated conditions and design constraints.

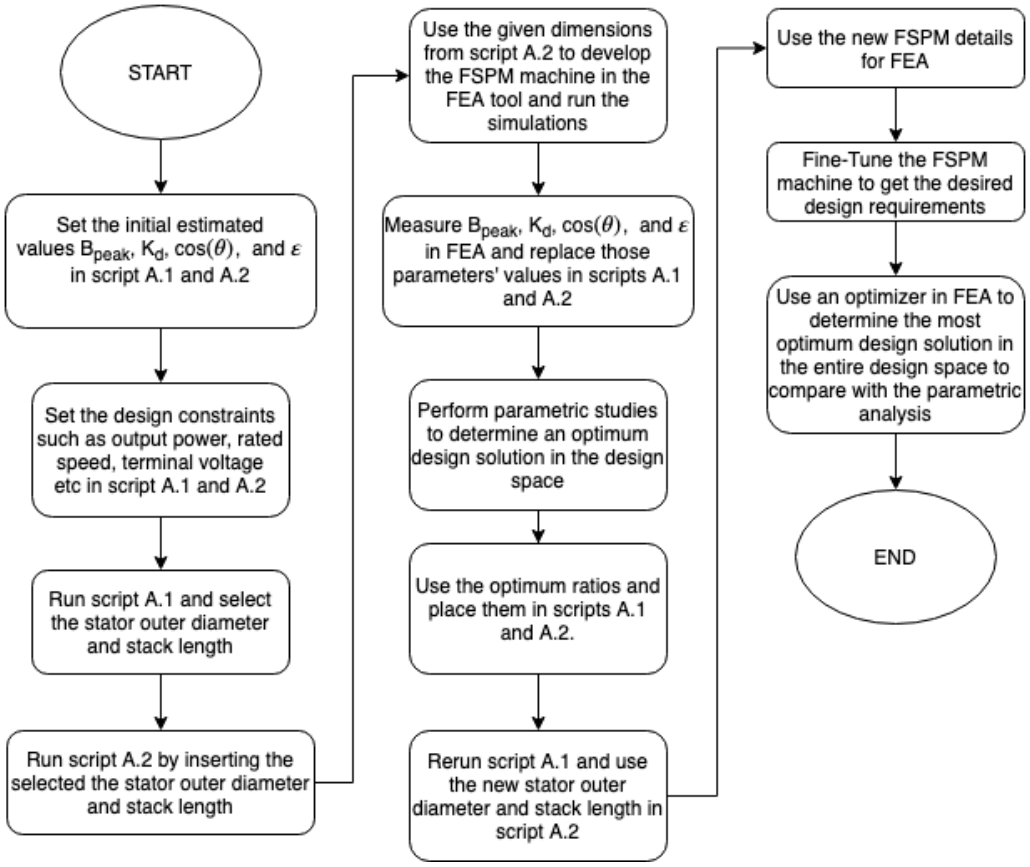

Figure 5.1: Design process followed in this dissertation

5.1 Analytical Design

The conventional FSPM machine's design specifications are summarized in Table 5.2. Note that the rotor's inner diameter, D_{ri}, is limited by the available shaft size that is used for testing. By using the code in Appendix A.1, the plot in Figure 5.2 shows the possible combinations of stator outer diameter and stack length to achieve the design requirements. From Figure 5.2, to meet the design requirements, the initial dimensions for the stator outer diameter and stack length are chosen to be 0.218 and 0.266 meters respectively. Using these dimensions in the script in Appendix A.2, sets the design data in Table 5.3.

Table 5.1: Initial Estimation of Parameters

Parameter	**Constraints**	**Units**
ϵ	0.9	-
$cos(\theta)$	0.88	-
B_{peak}	2	T
K_d	0.7	-
D_{cu}	1.626	mm

Table 5.2: Design Constraints of a Conventional FSPM Machine

Parameter	**Constraints**	**Units**
P_{out}	6	kW
V_t	220	V_{rms}
n_r	250	rpm
g	1	mm
m	3	-
N_s/N_r	12/14	-
J_s	5	A/mm^2
K_{cu}	0.4	-
C_s	0.25	-
D_{ri}	35	mm

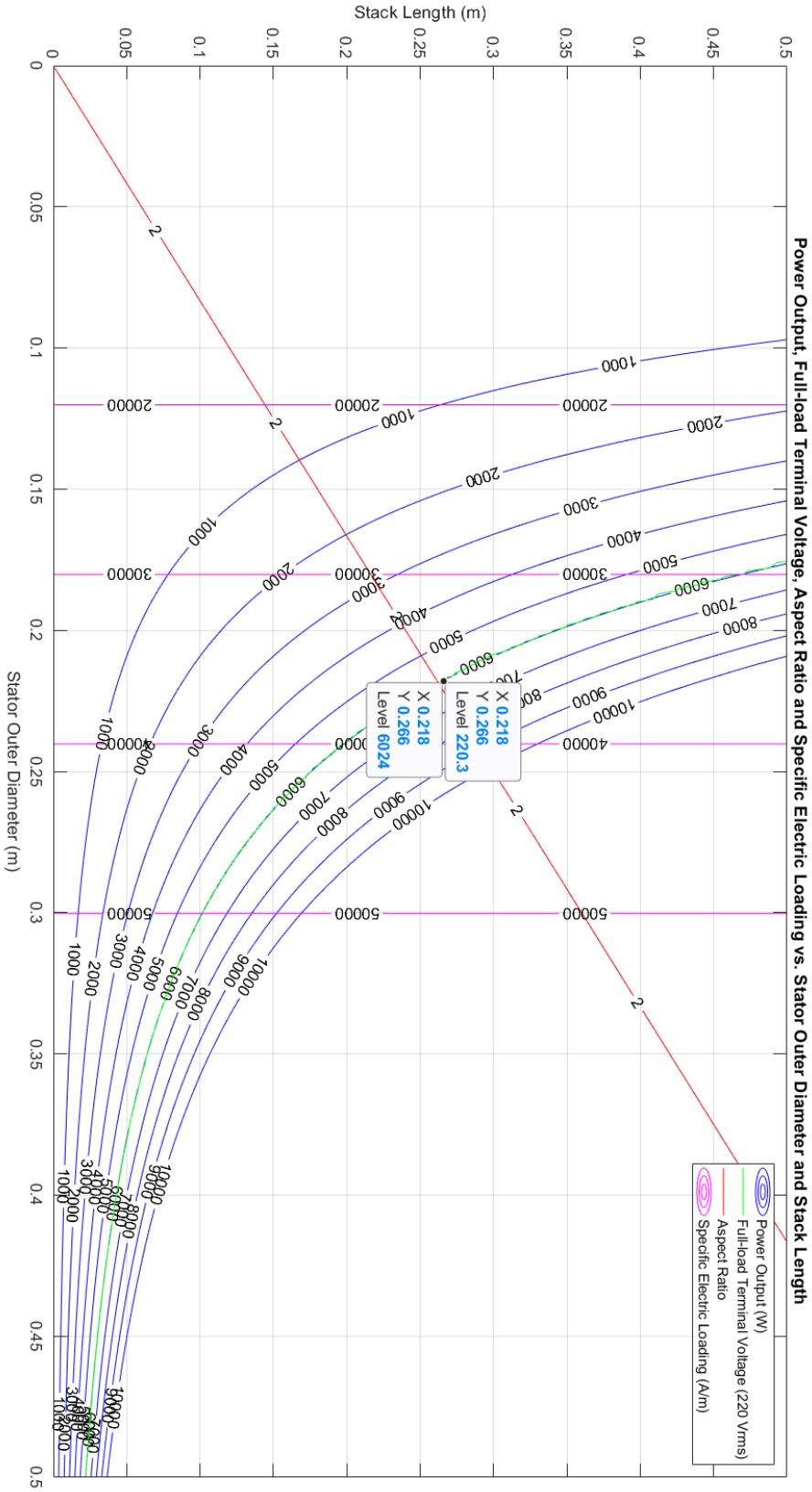

Figure 5.2: Stack length vs. stator outer diameter to achieve design requirements based on initial estimates of K_d, B_{peak} and ϵ

Table 5.3: Design Data of a Conventional FSPM Machine

Parameter	Design Data	Units
P_{out}	6.024	kW
V_t	220.3	V_{rms}
D_{so}	0.218	m
D_{si}	0.1308	m
D_{ro}	0.1288	m
D_{ri}	0.035	m
D_g	0.1298	m
l_{st}	0.266	m
N_t	240	-
β_s	0.0086	m
β_r	0.0086	m
H_{ys}	0.0086	m
H_{yr}	0.0086	m
β_{pm}	0.0086	m
A_s	36572	A/m
I_{rms}	10.3564	A
R_{ph}	1.0576	Ω
K_{es}	0.75	-
K_{er}	0.2962	-
K_{sio}	0.6	-

5.2 Numerical Analysis of the FSPM Machine

This section contains the information related to the numerical simulations of the FSPM machine. This includes details from the setup, to the parametric and sensitivity analyses, to the final machine's optimization as well as the reasoning behind design choices based on the results.

5.2.1 Setup

The first step is to determine the back-EMF waveform to ensure that it is sinusoidal in order to compare it with the analytical calculations. The simulations were performed using the current excitation method and assigning 0 A to each of the three phases. The

FSPM machine was initially set in its d-axis position as calculated below to ensure that the overlapping area between the rotor poles and stator teeth for a single phase are at a maximum.

$$\theta_{initial} = \frac{\frac{360^\circ}{N_r}}{\frac{N_s}{m}} \tag{5.1}$$

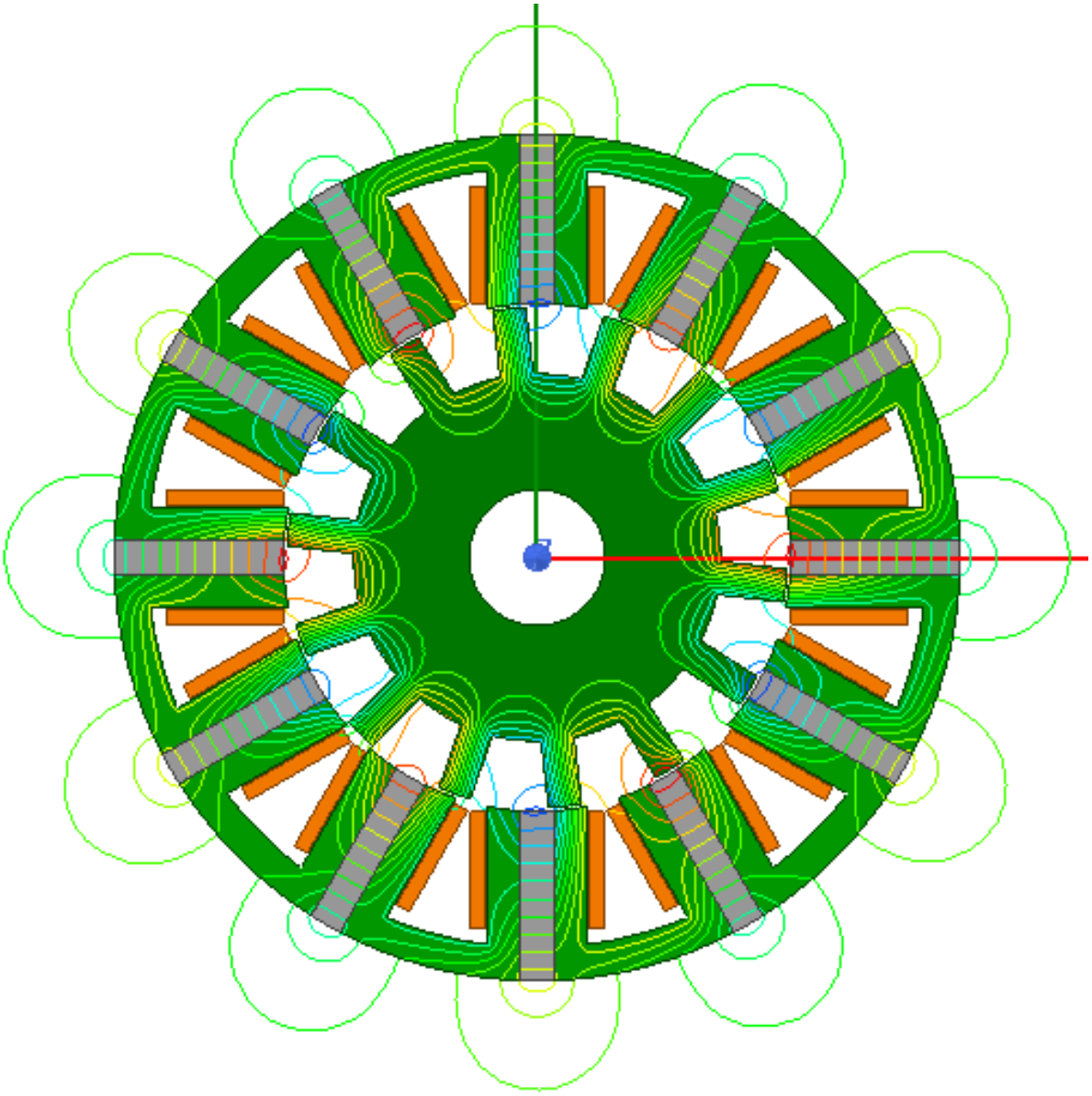

Figure 5.3: 12/14 FSPM in the d-axis position including flux lines

Proof of the d-axis position is also indicated in Figure 5.4 where the starting position of -6.43 mechanical degrees results in a negative maximum flux.

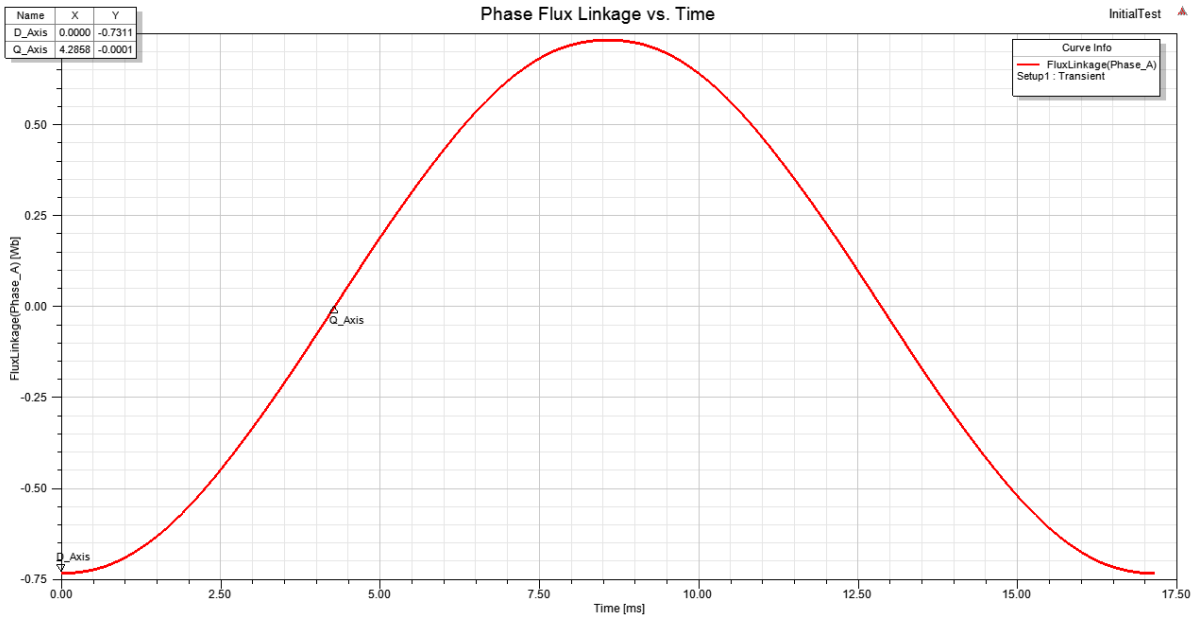

Figure 5.4: Phase flux indicating d- and q-axis positions

5.2.2 Initial Results

These results include an analysis of the back-EMF, cogging torque, no-load air-gap flux density, full-load current and terminal voltage, as well as the output power.

5.2.2.1 No-Load

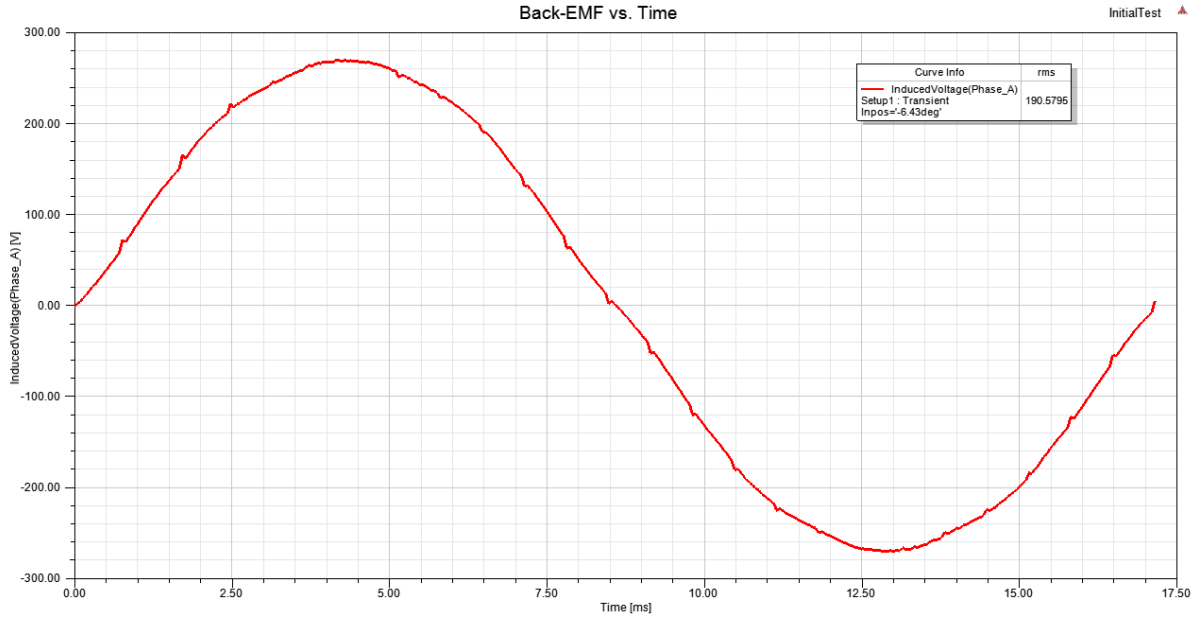

Figure 5.5: Phase A back-EMF of initial design

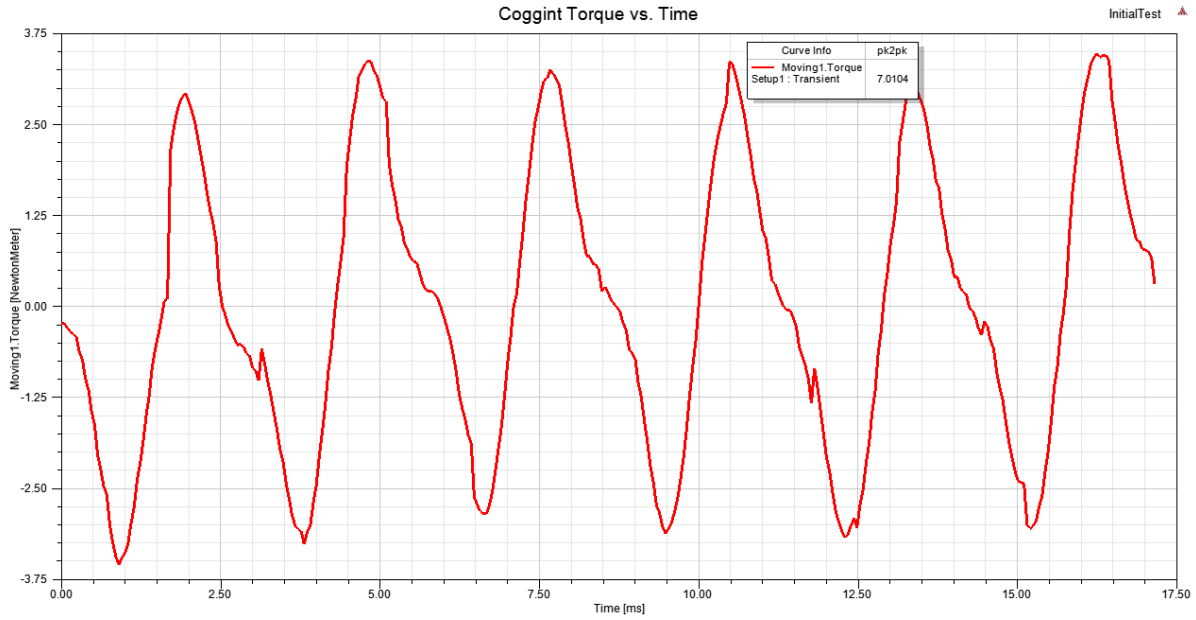

Figure 5.6: Cogging torque

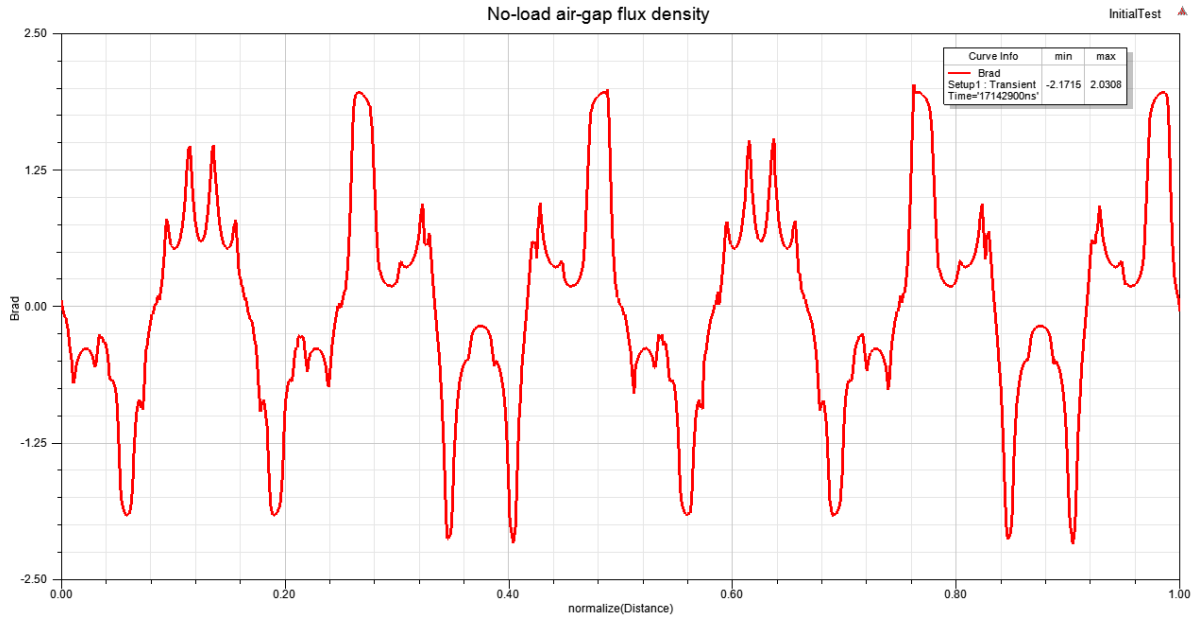

Figure 5.7: No-load air-gap flux density

The no-load air-gap flux density in Figure 5.7 is very asymmetrical and peaks at 2.0308 T and -2.1715 T.

5.2.2.2 Full-Load

The current excitation method is adopted to mimic the drive at its rated condition in the dq reference frame. The induced currents for a three-phase machine are displaced

$(0°, -2\pi/3°, 2\pi/3°)$ as follows:

$$\begin{cases} I_a = I_{peak} sin\left(2\pi ft + \gamma\right) \\ I_b = I_{peak} sin\left(2\pi ft - \frac{2\pi}{3} + \gamma\right) \\ I_c = I_{peak} sin\left(2\pi ft + \frac{2\pi}{3} + \gamma\right) \end{cases} \tag{5.2}$$

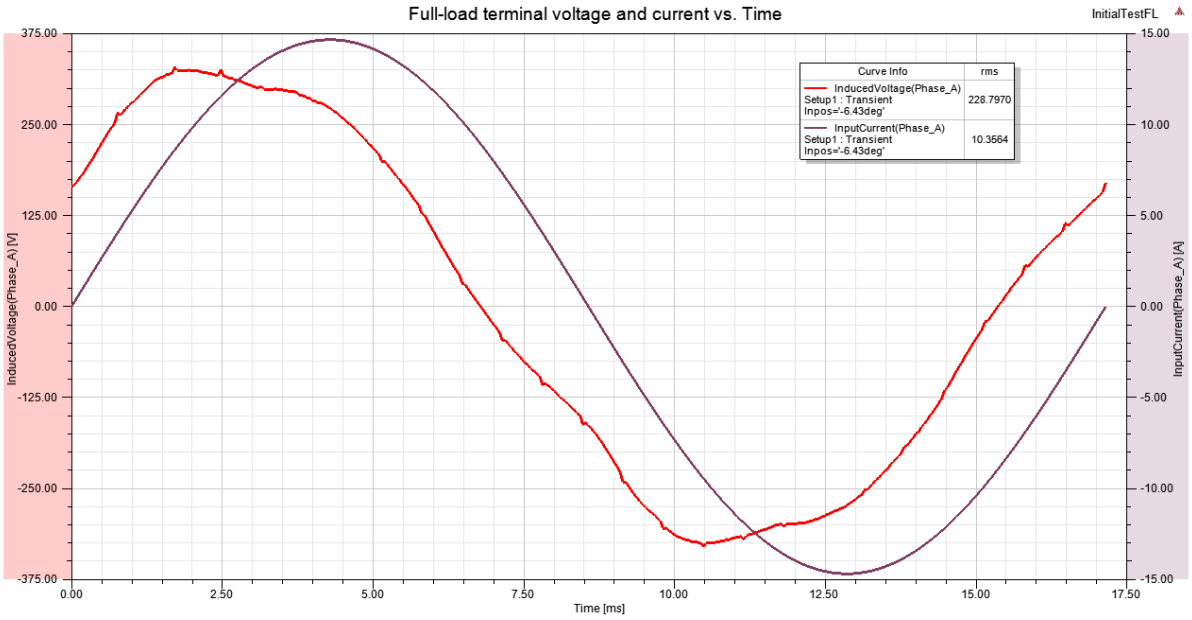

Figure 5.8: Phase A Full-load Voltage and Current

By using the current angle of 0° to obtain the maximum torque under $I_d = 0$ control, the terminal voltage and rated current is shown above. This indicated that the back-EMF voltage of 190.5795 V_{rms} is in fact lower than the terminal voltage of 228.797 V_{rms}. This increase in voltage across the terminal is attributed to the fact that the FSPM machine is simulated as a motor, and hence, the terminal voltage phasor's magnitude is greater than that of the back-EMF phasor's magnitude.

Figure 5.9: Output Power

The initial design values for the back-EMF using the estimated parameters in Table 5.1 shows the following errors:

Table 5.4: Initial Design Data Comparison

Parameter	**Analytical**	**FEA**	**% Error**	**Units**
E_{rms}	198.27	190.5795	-3.88	V_{rms}
V_{rms}	220.3	228.797	+3.94	V_{rms}
P_{out}	6.024	5.778	-4.08	kW
B_{peak}	2	2.1715	+8.58	T
K_d	0.7	0.62	-11.43	-
ϵ	0.9	0.833	-7.44	-
$cos(\theta)$	0.88	0.79	-10.23	-

From Table 5.4, it is clear that the estimated parameters B_{eak}, K_d, ϵ, and $cos(\theta)$ lead to the differences between the analytical and FEA results. After substituting the estimated values with the measured ones into the script in Appendix A.2, the analytical output power is 5.6158 kW, which is 2.81% less than the 5.778 kW measured in FEA. The error in output power is relatively small and most likely due to the the harmonic components associated with the waveforms that's not considered in the analytical formulae, and the calculation of the losses for the output power determination. The results however, are

satisfactory as it acts as an initial design whereby fine-tuning can commence using the FEA software.

Before fine-tuning the design, and since the full-load terminal voltage and output power are respectively higher and lower than what is designed for, it's advisable to rerun the script in Appendix A.1 with the measured values of B_{eak}, K_d, ϵ, and $cos(\theta)$. Even though these parameters will slightly change again for new geometrical parameters, it will provide a design that's closer to the requirements of 6 kW and 220 V_{rms}. Due to the parameters affecting each other's optimal values, the easiest way to fine-tune the terminal voltage and output power are by varying the stack length and current density respectively. This is not ideal and is why an optimizer is required to find the optimal solution in the design space.

Chapter 6

Parametric Design and Analysis

The following chapter includes the studying of parameter changes and its effects on the back-EMF and cogging torque of an FSPM machine. The optimal ratios obtained are used to design an FSPM machine that meets the design specifications. These results are also used to provide the optimizer in chapter 7 with a range of values where the optimal design should lie within.

Parametric studies are performed to manually determine the optimised geometrical values to meet the desired design specifications. With the help of the analytical formulae presented in this dissertation, conclusions are made based on the analytical proof to support the results obtained. Multiple parametric studies have been conducted in [6, 16, 28, 46, 47, 50] and the optimal ratios have been noted. These ratios are highly dependant on the number of rotor pole and stator slot combinations. Comparisons between the ratios are summarized in Table 2.1 and those obtained from the parametric study is made.

Since an outer rib on the stator needs to be added, it's effects on the electromagnetic performance are studied first. This is followed by the rotor tooth width to ensure a sinusoidal back-EMF waveform is obtained for analytical comparisons, the stator back-iron, permanent magnet thickness, and rotor yoke thickness. For each study, the back-EMF and cogging torque variations are presented and discussed. In this dissertation, the goal is to find the ratios that maximizes the back-EMF and minimizes the cogging torque. The optimum ratios obtained in these studies are used in the parametrically optimized FSPM machine design which should provide a better representation of the analytical design. Furthermore, these optimal ratios are used in the optimization chapter as the starting point to reduce the simulation time in order to find the most optimum solution.

6.1 Stator Outer Rib

Initially, a rib needed to be added to the stator's outer diameter to link all the U-shaped laminations to simplify the assembly process. A 2 mm rib length was chosen as it's thick enough and provides a 1.7% increase in back-EMF at the expense of a slightly higher cogging torque. The increase in back-EMF is attributed to lower flux leakage on the stator outer rib and a reduction in peak flux density in the core. During the parametric study, the stator's outer diameter is fixed, therefore, the variation in cogging torque is due to the fact that as the outer rib's length changes, it changes the amount of PM volume which has a direct impact on the flux and flux leakage.

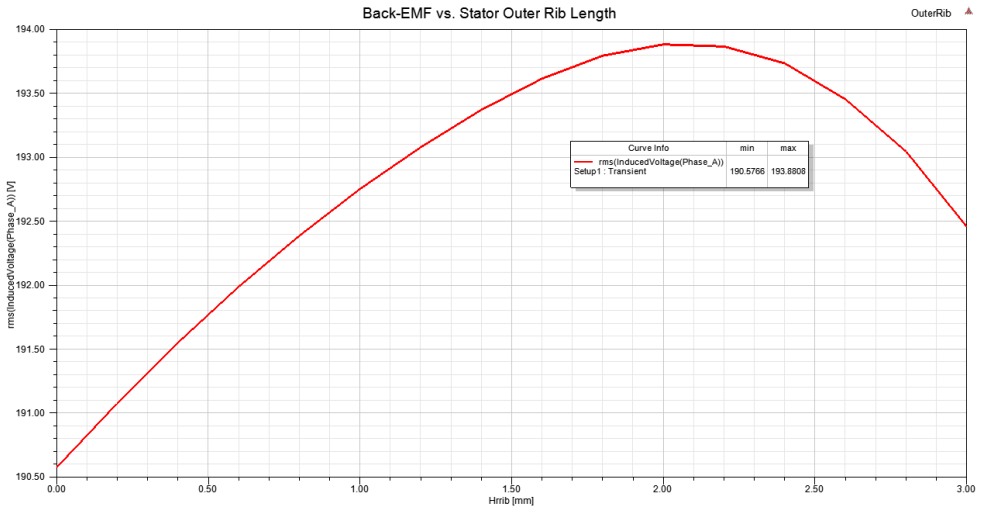

Figure 6.1: Back-EMF vs. the rib length on the stator's outer diameter

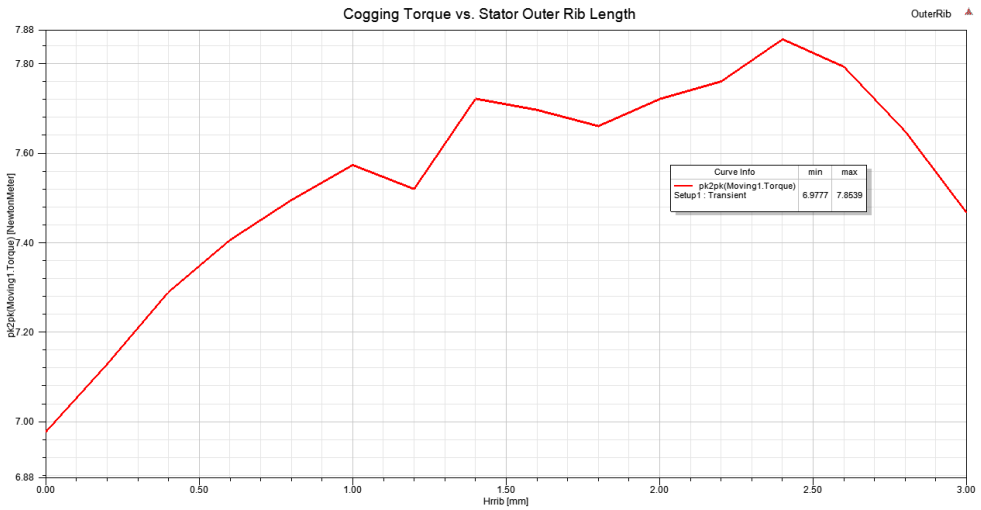

Figure 6.2: Cogging torque vs. the rib length on the stator's outer diameter

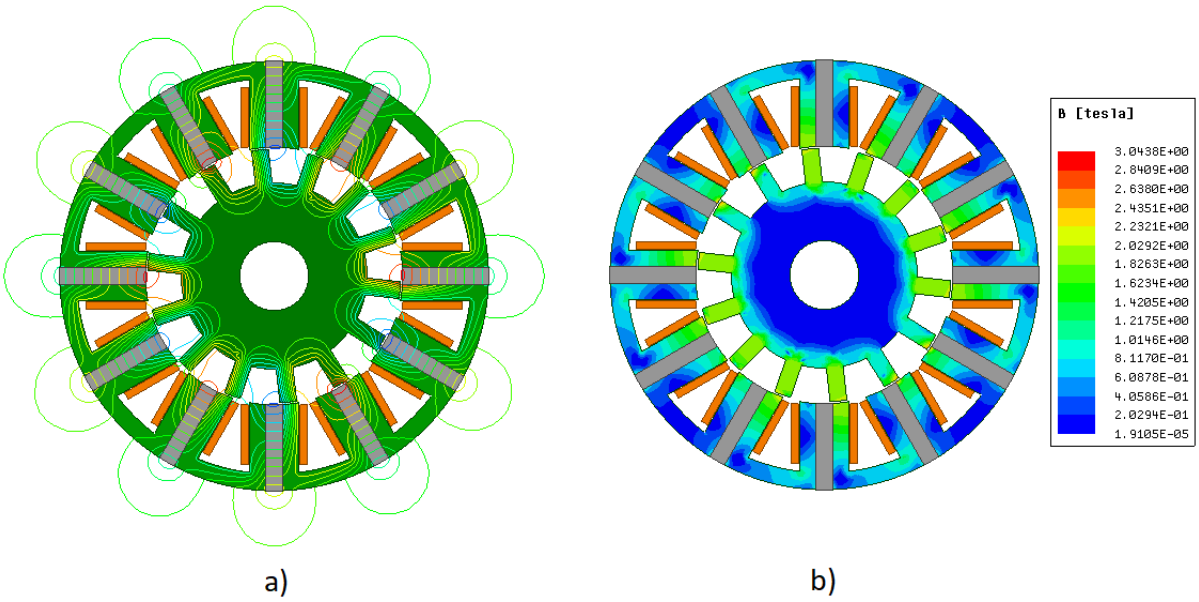

Figure 6.3: Nominal FSPM a) Flux lines and b) Flux density in the d-axis position

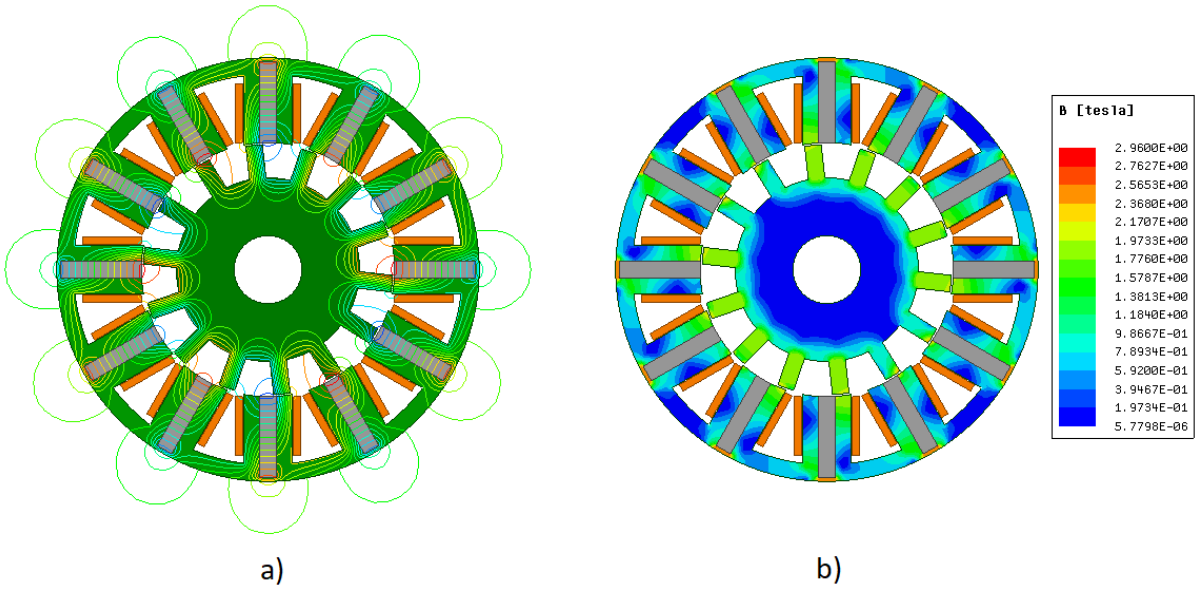

Figure 6.4: FSPM with 2mm outer rib a) Flux lines and b) Flux density in the d-axis position

6.2 Rotor Pole Width

A ratio of 1.4 times the nominal was chosen since a 4.27% increase in back-EMF and a 34.41% decrease in cogging torque are observed over the nominal results. The increase in back-EMF is attributed to a bigger overlapping area between the stator teeth and rotor poles for a given phase, and the decrease in cogging torque due to the reduction in the change of reluctance with respect to the rotor's position.

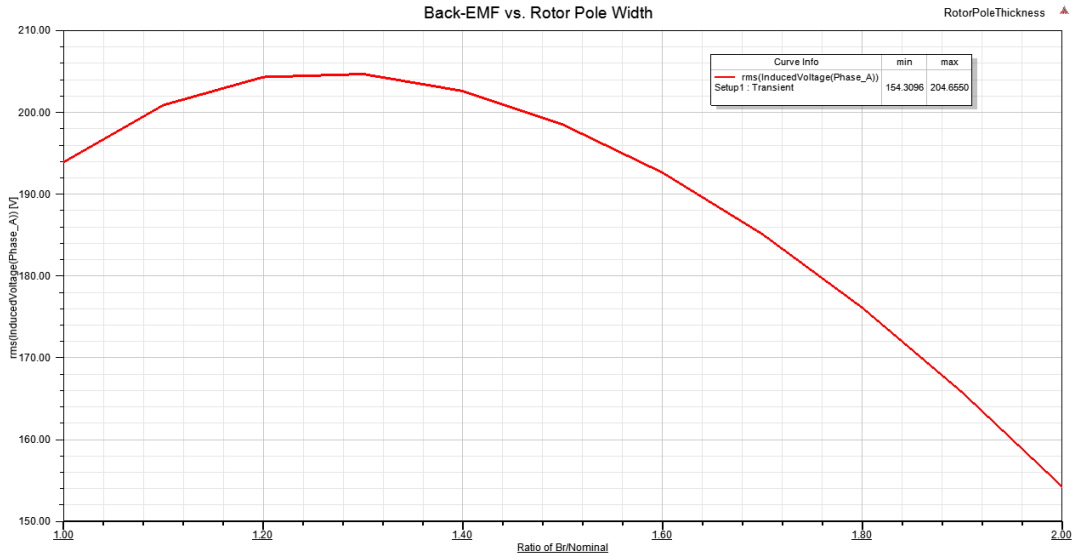

Figure 6.5: Back-EMF vs. the ratio of new rotor pole thickness to the nominal

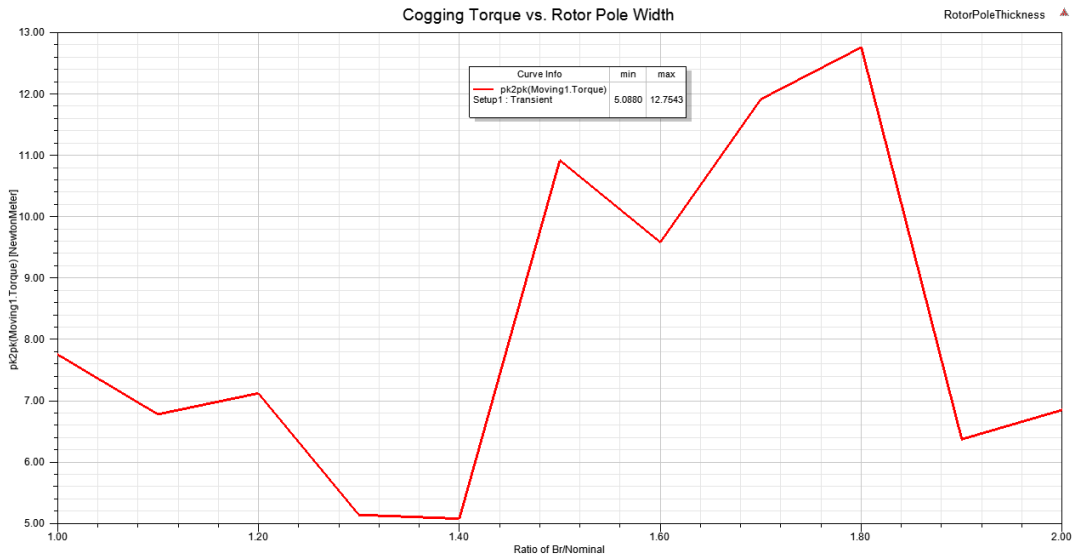

Figure 6.6: Cogging torque vs. the ratio of new rotor pole thickness to the nominal

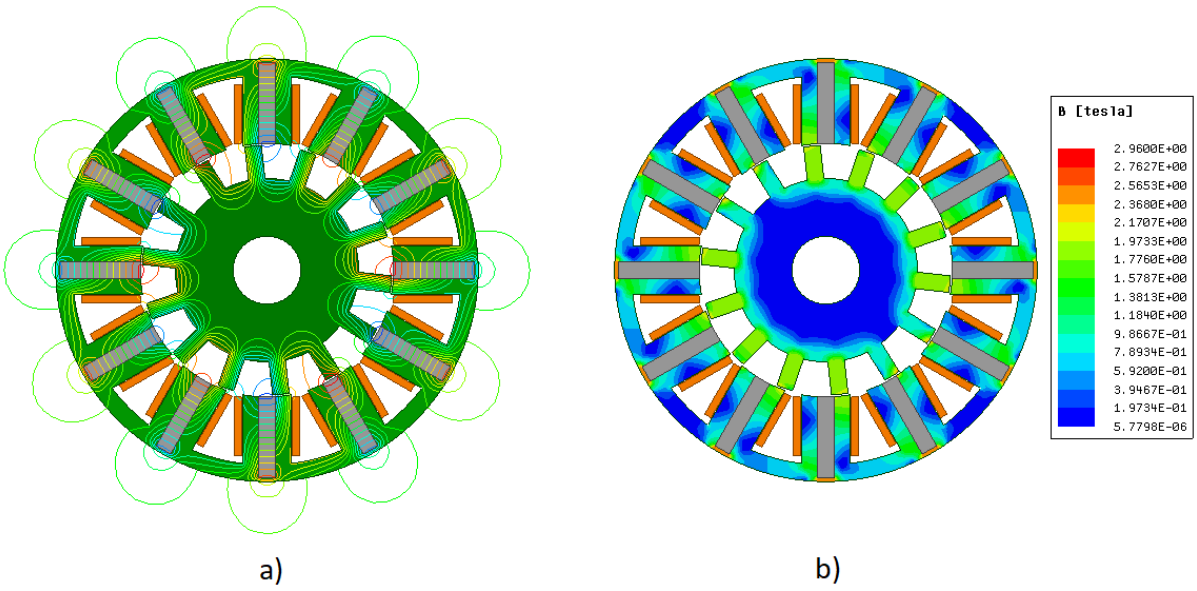

Figure 6.7: FSPM with 2mm outer rib a) Flux lines and b) Flux density in the d-axis position

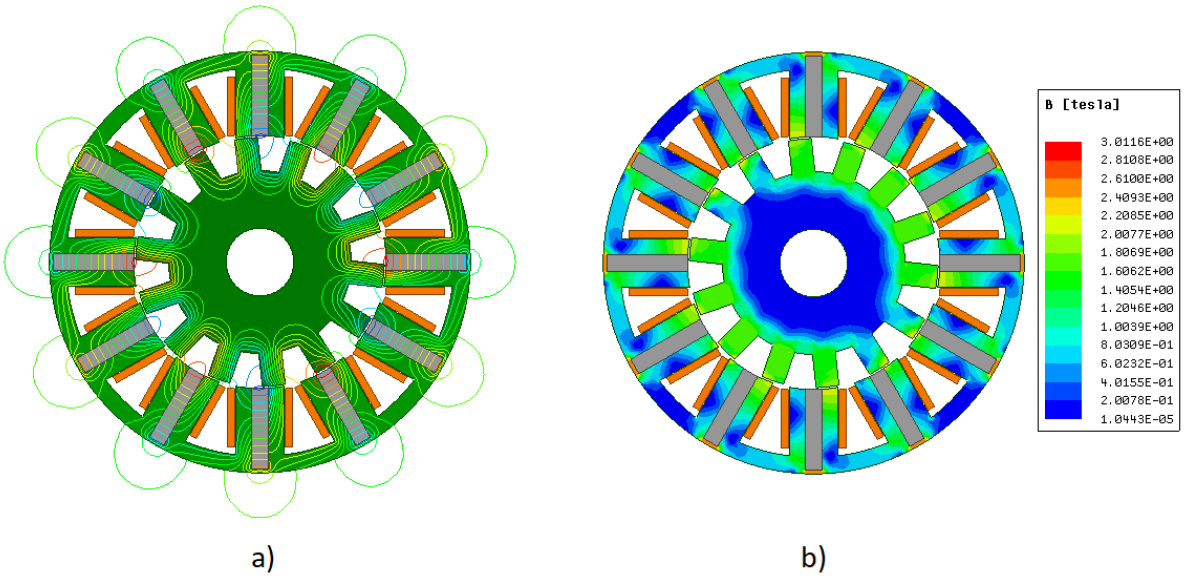

Figure 6.8: FSPM with 1.4 times the nominal rotor pole thickness a) Flux lines and b) Flux density in the d-axis position

6.3 Stator Back-Iron

The nominal ratio was chosen since only a 0.09% increase in back-EMF and a 1.97% decrease in cogging torque are observed at a ratio of 1.1 over the nominal results. The small increase in back-EMF is likely due to the reduction in leakage flux as the stator back-iron becomes unsaturated and the decrease in cogging torque due to the increase in the magnetic circuit's reluctance which reduces the air-gap flux.

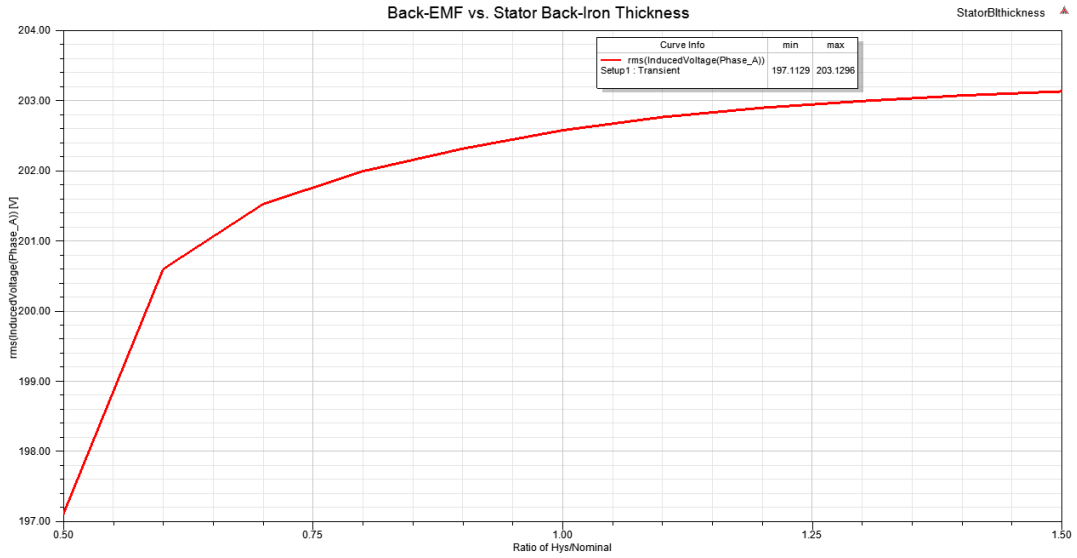

Figure 6.9: Back-EMF vs. the ratio of new stator back-iron thickness to the nominal

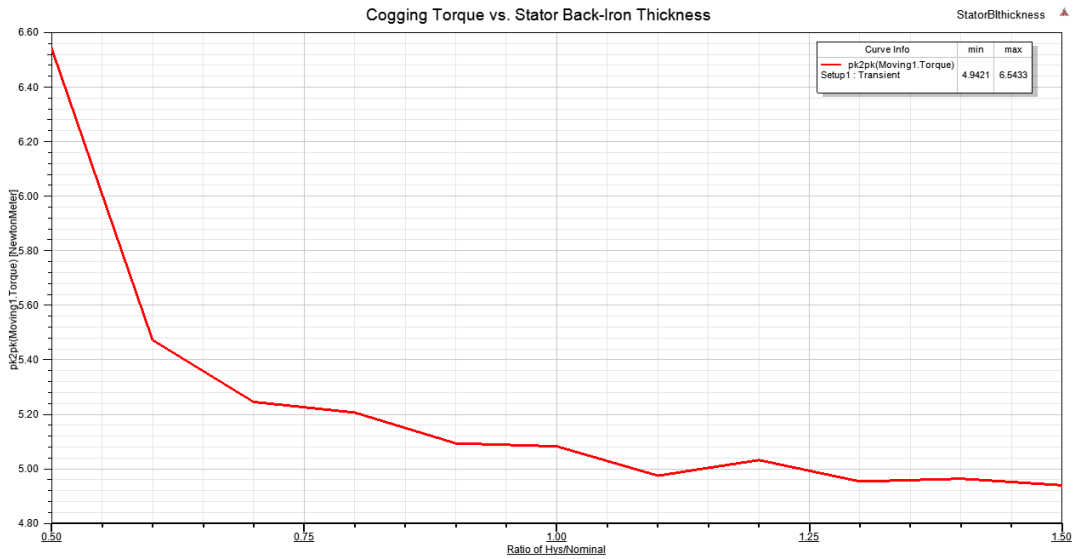

Figure 6.10: Cogging torque vs. the ratio of new stator back-iron thickness to the nominal

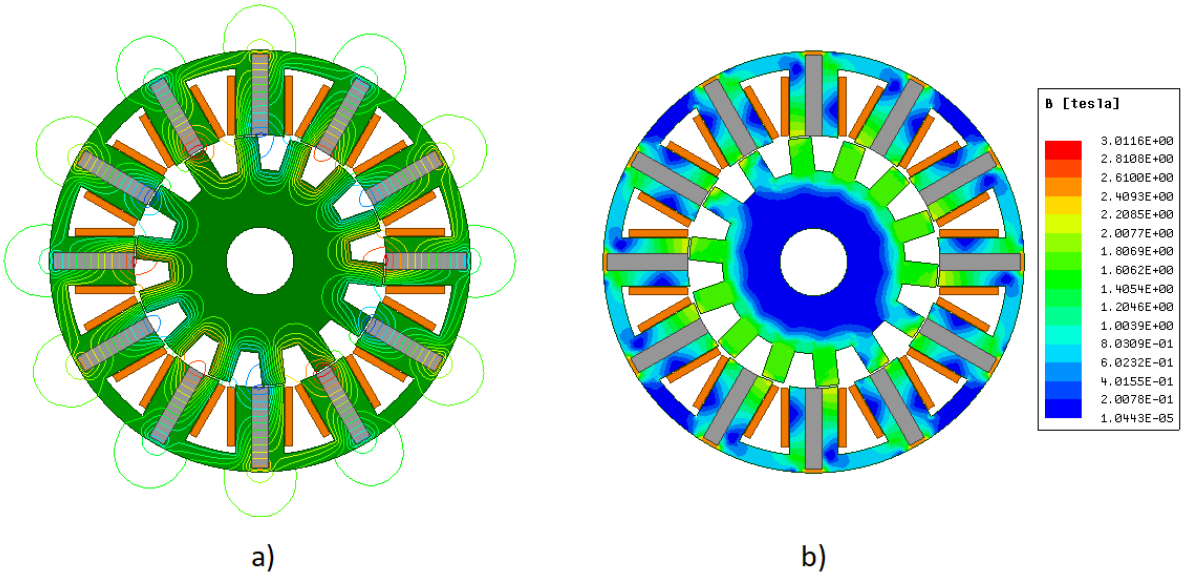

Figure 6.11: FSPM with 1.4 times the nominal rotor pole thickness a) Flux lines and b) Flux density in the d-axis position

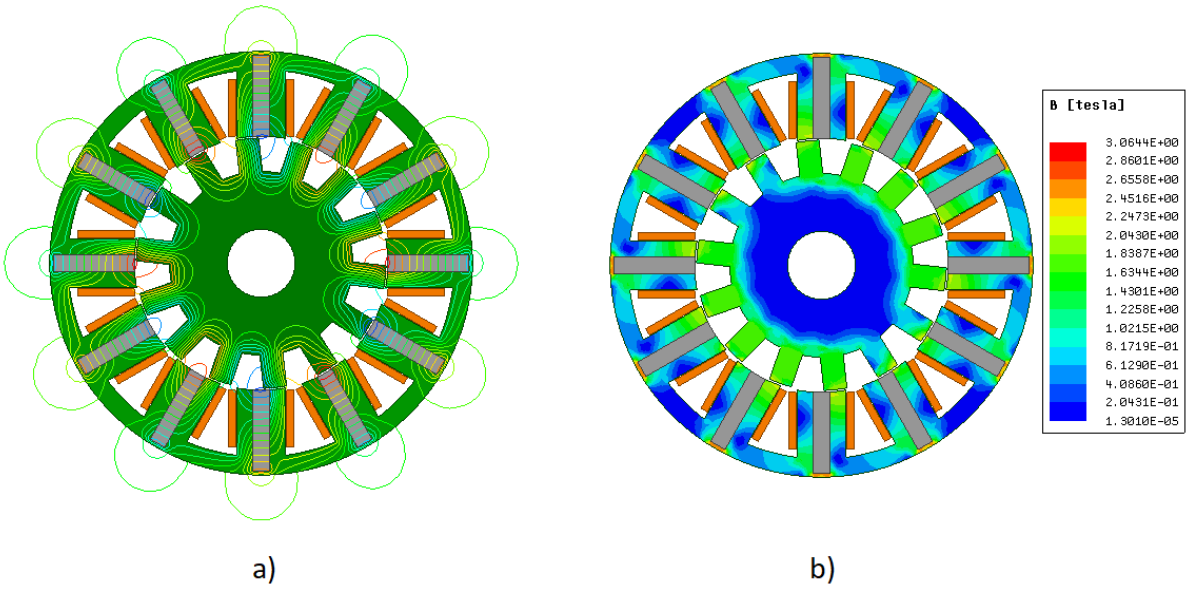

Figure 6.12: FSPM with 1.1 times the nominal stator back-iron thickness a) Flux lines and b) Flux density in the d-axis position

6.4 Permanent Magnet Thickness

The stator pole arc length was kept the same as the nominal arc length, therefore, a reduction in PM thickness increases the stator tooth width. A ratio of 0.8 times the nominal was chosen since a 9.02% increase in back-EMF and no change in cogging torque are observed over the nominal results. The increase in back-EMF is due to a reduction in leakage flux and unsaturated stator tooth tops.

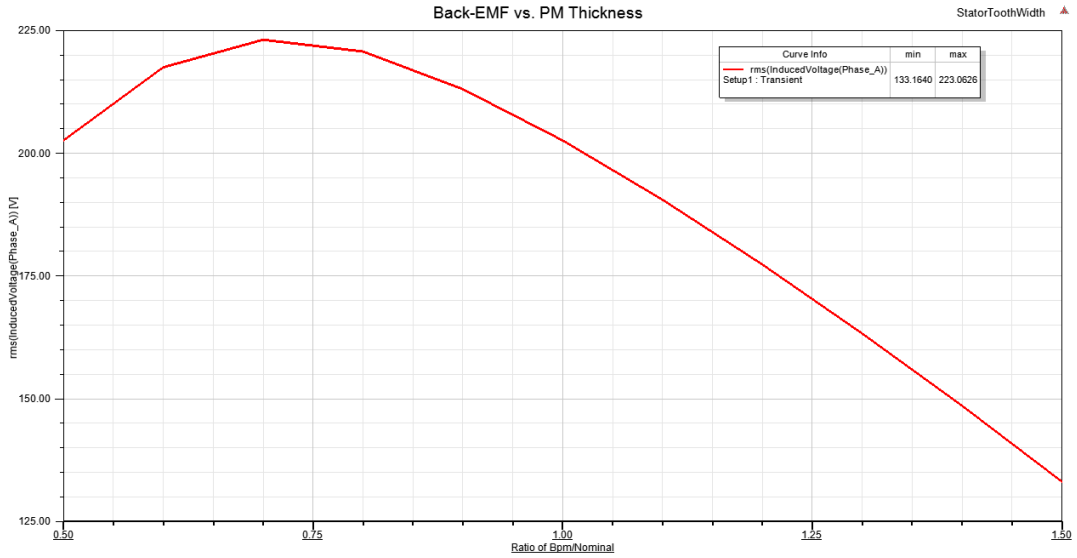

Figure 6.13: Back-EMF vs. the ratio of new PM thickness to the nominal

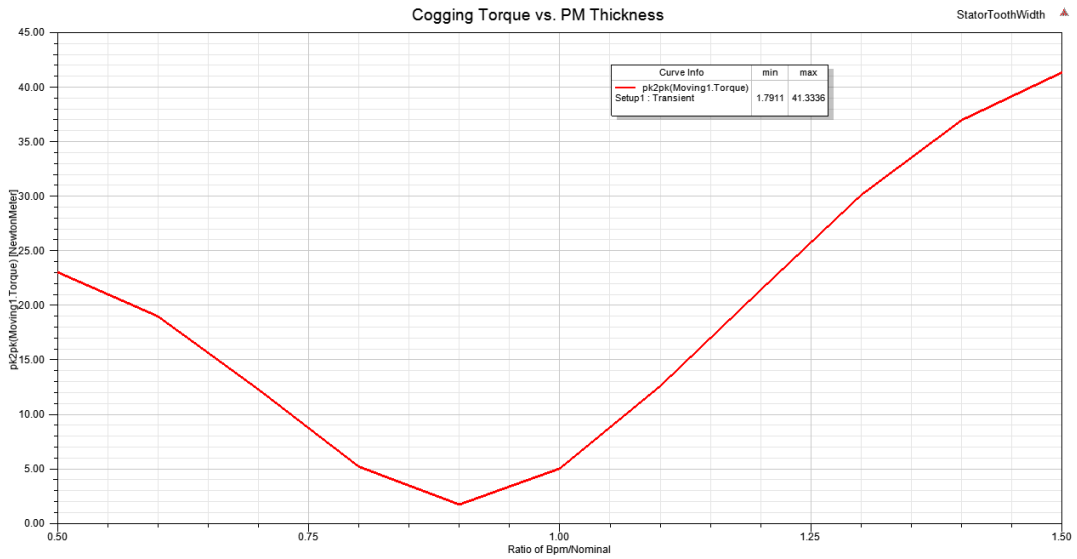

Figure 6.14: Cogging torque vs. the ratio of new PM thickness to the nominal

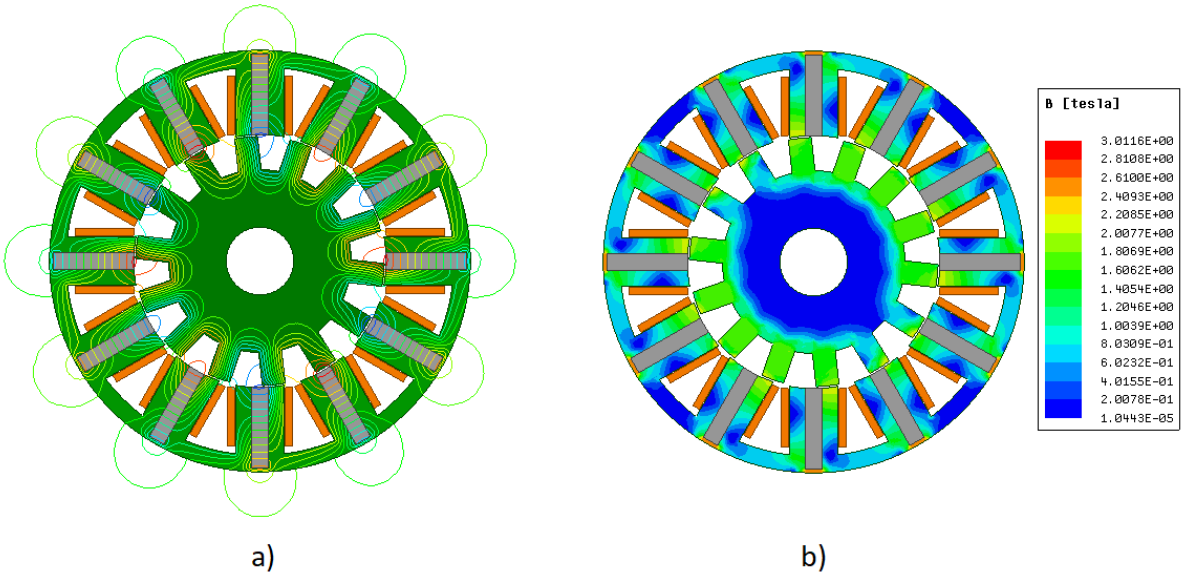

Figure 6.15: FSPM with 1.4 times the nominal rotor pole thickness a) Flux lines and b) Flux density in the d-axis position

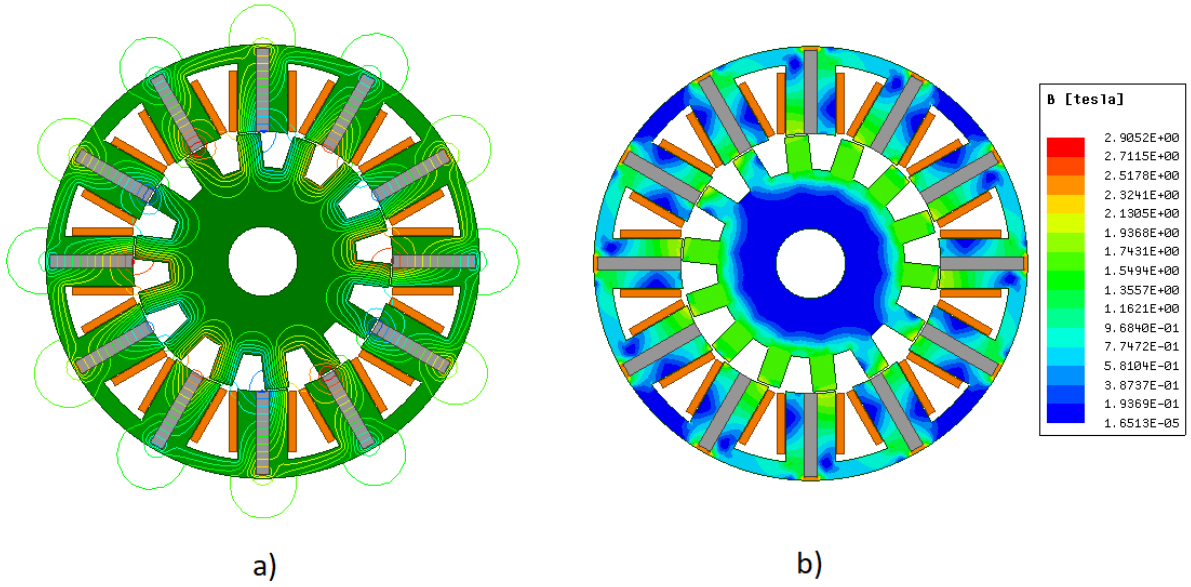

Figure 6.16: FSPM with 0.8 times the nominal permanent magnet thickness a) Flux lines and b) Flux density in the d-axis position

6.5 Rotor Yoke Thickness

A ratio of 1.3 times the nominal was chosen since a 1.13% decrease in back-EMF and a 28.08% decrease in cogging torque are observed over the nominal results. The decrease in back-EMF is attributed to a bigger magnetic circuit reluctance for a given phase and more leakage flux, and the decrease in cogging torque due to the reduction in the magnetic circuit flux.

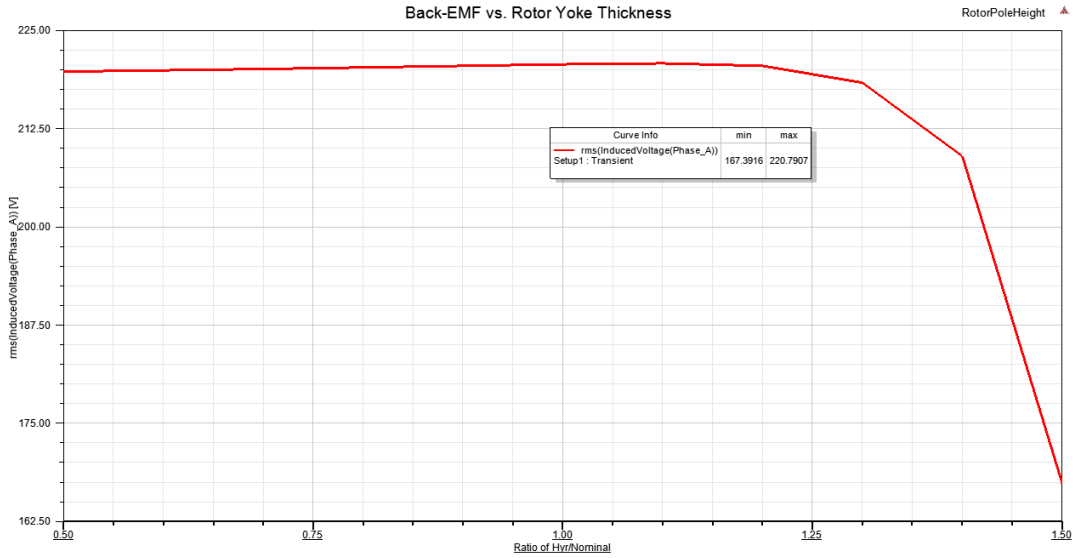

Figure 6.17: Back-EMF vs. the ratio of new rotor yoke thickness to the nominal

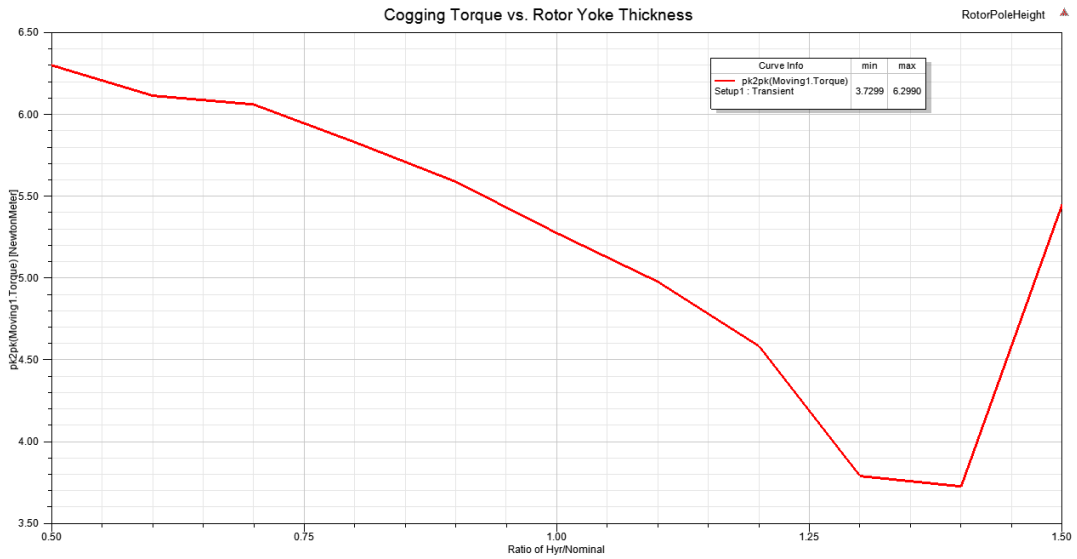

Figure 6.18: Cogging torque vs. the ratio of new rotor yoke thickness to the nominal

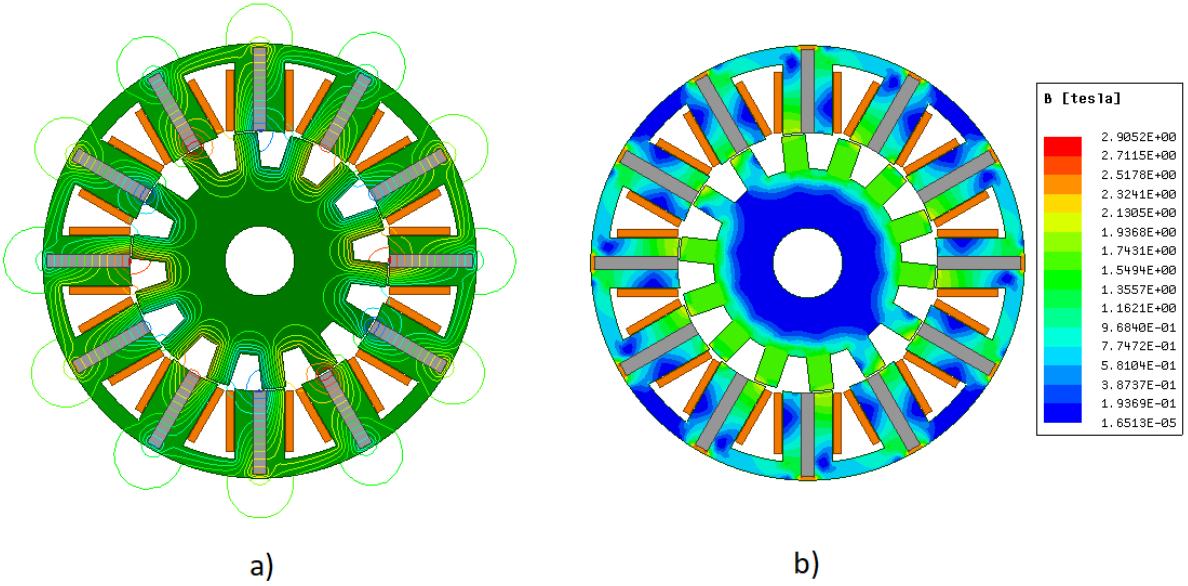

Figure 6.19: FSPM with 0.8 times the nominal permanent magnet thickness a) Flux lines and b) Flux density in the d-axis position

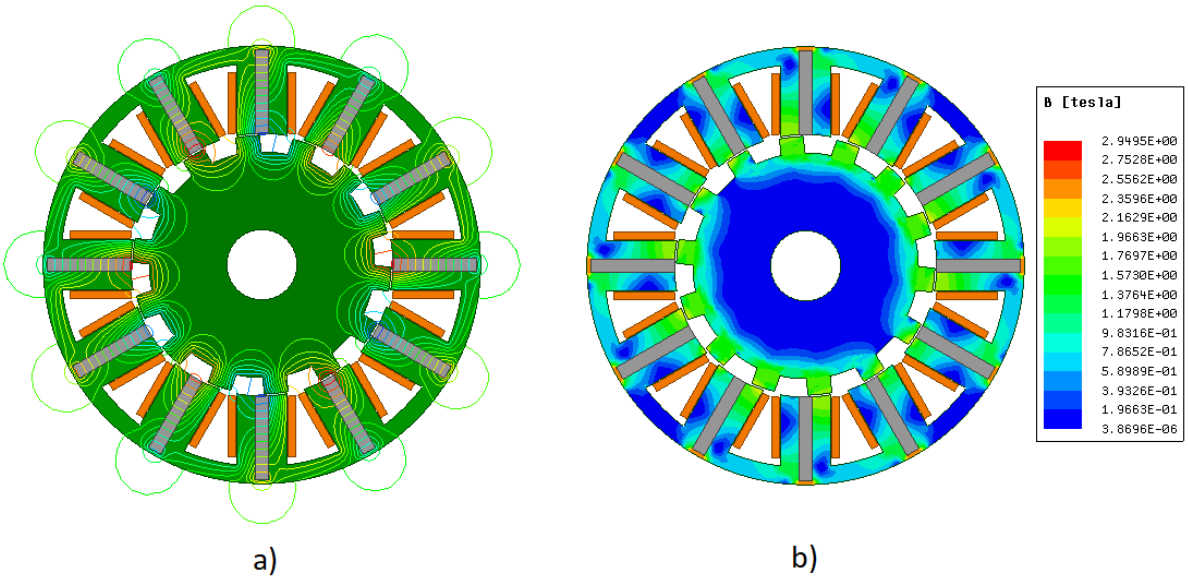

Figure 6.20: FSPM with 1.3 times the nominal rotor yoke thickness a) Flux lines and b) Flux density in the d-axis position

6.6 Summary

The no-load and full-load performance characteristics for the FSPM machine using these optimized ratios and the stator outer diameter rib are documented below.

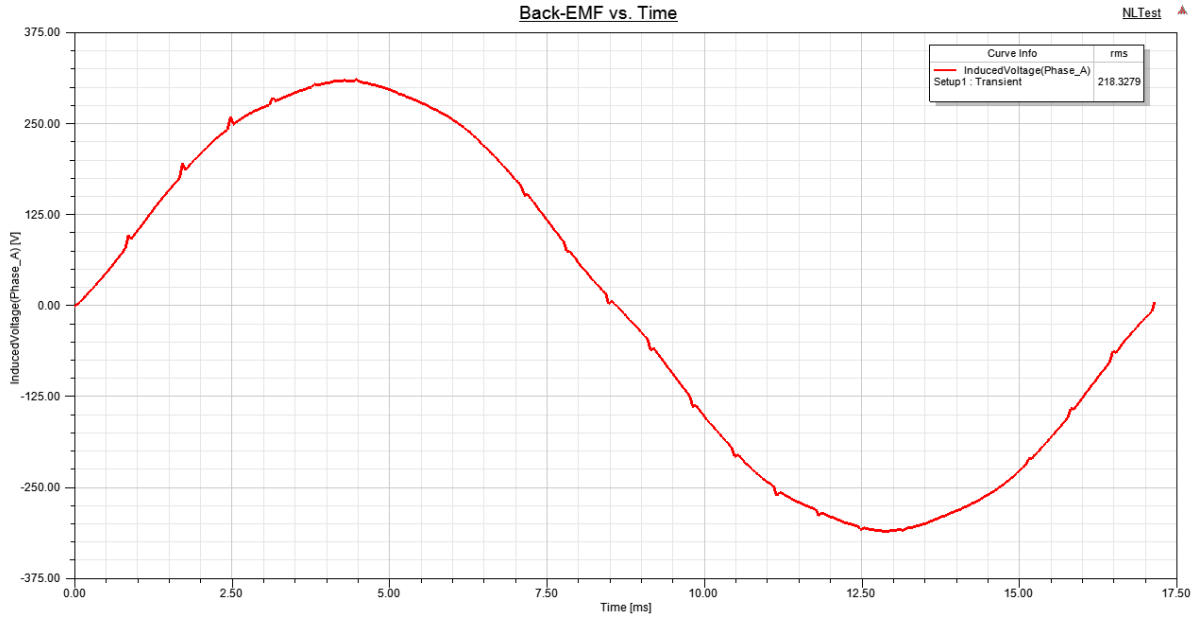

Figure 6.21: Back-EMF of parametrically optimized FSPM machine

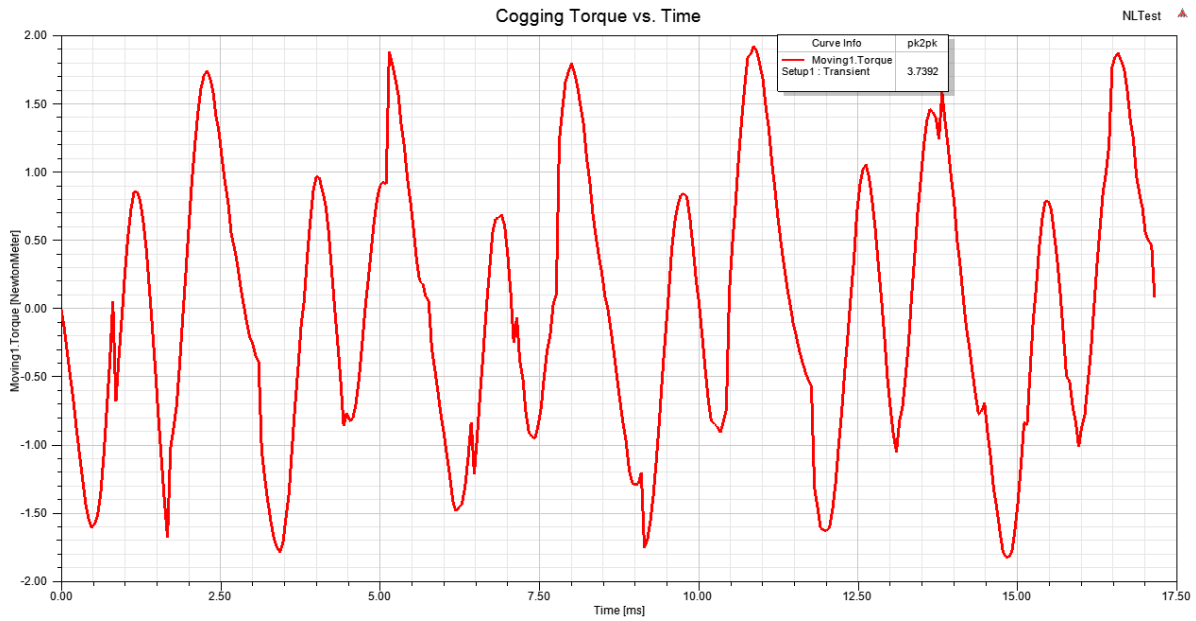

Figure 6.22: Cogging torque of parametrically optimized FSPM machine

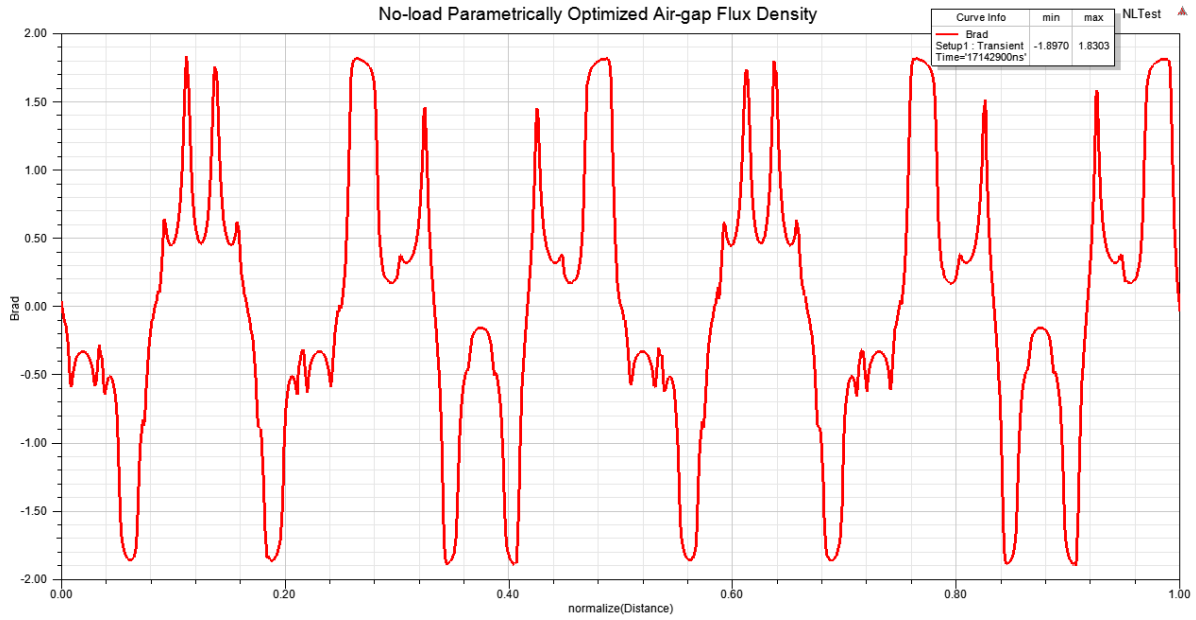

Figure 6.23: No-load air-gap flux density of parametrically optimized FSPM machine

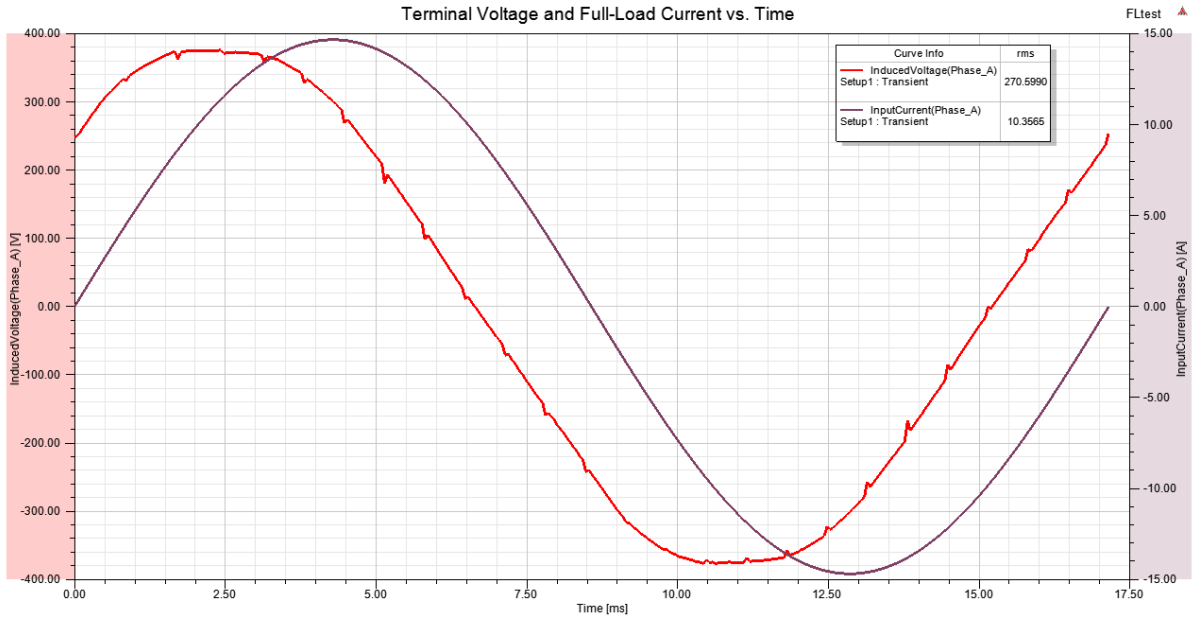

Figure 6.24: Full-load terminal voltage of parametrically optimized FSPM machine

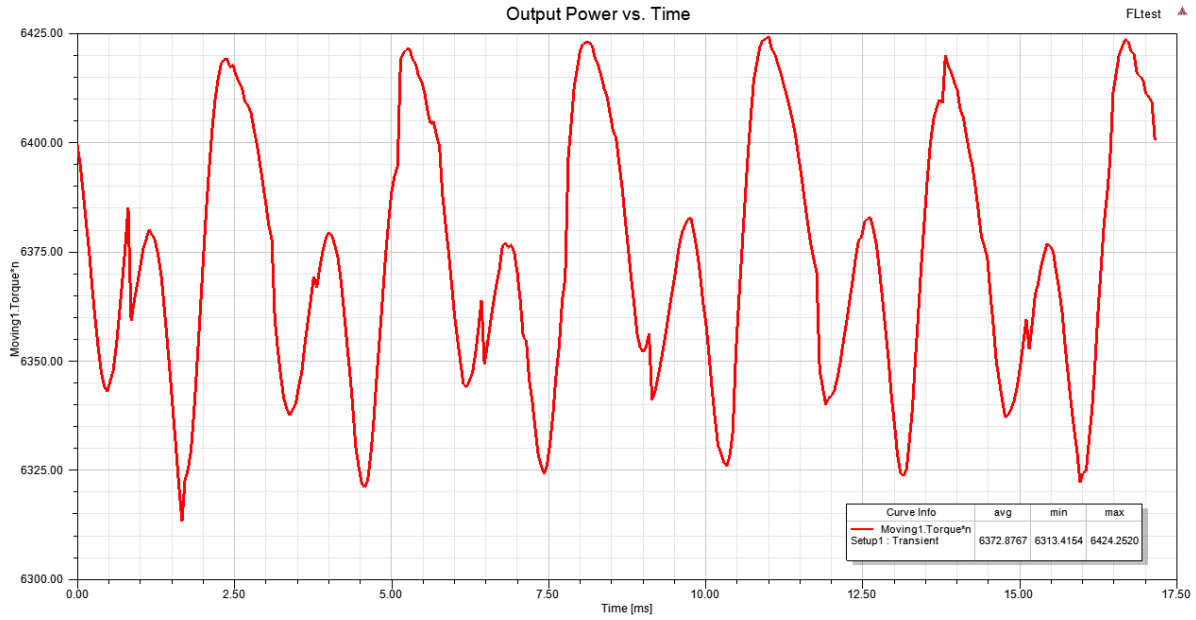

Figure 6.25: Output power of parametrically optimized FSPM machine

Table 6.1 summarizes the initial design's performance to the parametrically optimized. The optimum ratios obtained from the parametric analysis are summarized in Table 6.2 and includes the length of the stator's outer diameter rib.

Table 6.1: Initial vs. Parametrically Optimized (PO) FSPM Machine's Performance

Parameter	**Initial FSPM**	**PO FSPM**	**% Change**	**Units**
E_{rms}	190.5795	218.3279	+14.56	V_{rms}
T_{cog}	7.0104	3.7392	-46.66	Nm_{pk-pk}
V_{rms}	228.797	270.557	+18.25	V_{rms}
P_{out}	5.778	6.373	+10.3	kW
B_{peak}	2.1715	1.897	-12.64	T
K_d	0.62	0.7387	+19.15	-
ϵ	0.833	0.807	-3.12	-
$cos(\theta)$	0.79	0.758	-4.05	-

Table 6.2: Optimal Geometric Ratios Obtained from Parametric Analysis

Parameter	Optimal Ratio	Units
H_{ribSO}	2	mm
β_r	1.4	-
H_{ys}	1	-
β_{pm}	0.8	-
H_{yr}	1.3	-

6.7 Design Using Optimal Parametric Ratios

The new ratios in Table 6.2 are used in the script in Appendix A.1 to analytically determine the stack length and stator outer diameter. These estimates will change for the new design, but it will provide a closer approximation than the initial estimates.

Table 6.3: Estimation of Parameters

Parameter	Constraints	Units
ϵ	0.807	-
$cos(\theta)$	0.758	-
B_{peak}	1.897	T
K_d	0.7387	-

Upon rerunning the script in Appendix A.1, it's evident that with the rated current is too low for the dimensions to provide an output power of 6 kW and a full-load voltage of 220 V_{rms} as depicted in Figure 6.26. According to (4.33), this means that the conductor size or current density has to increase. Since the design constraint of 5 A/mm^2 is in place, the conductor size is first increased.

The next bigger conductor size from Appendix C is 1.829 mm, meaning that the current density J_s needs to be reduced to obtain the correct output power at a full-load terminal voltage of 220 V_{rms}. Reducing the current density is acceptable since this will improve cooling in the conductors, however, changing the current will also have an effect on the full-load terminal voltage. Figure 6.27 shows the new dimensions for $D_{ac} = 1.829$ mm and $J_s = 4.65\ A/mm^2$.

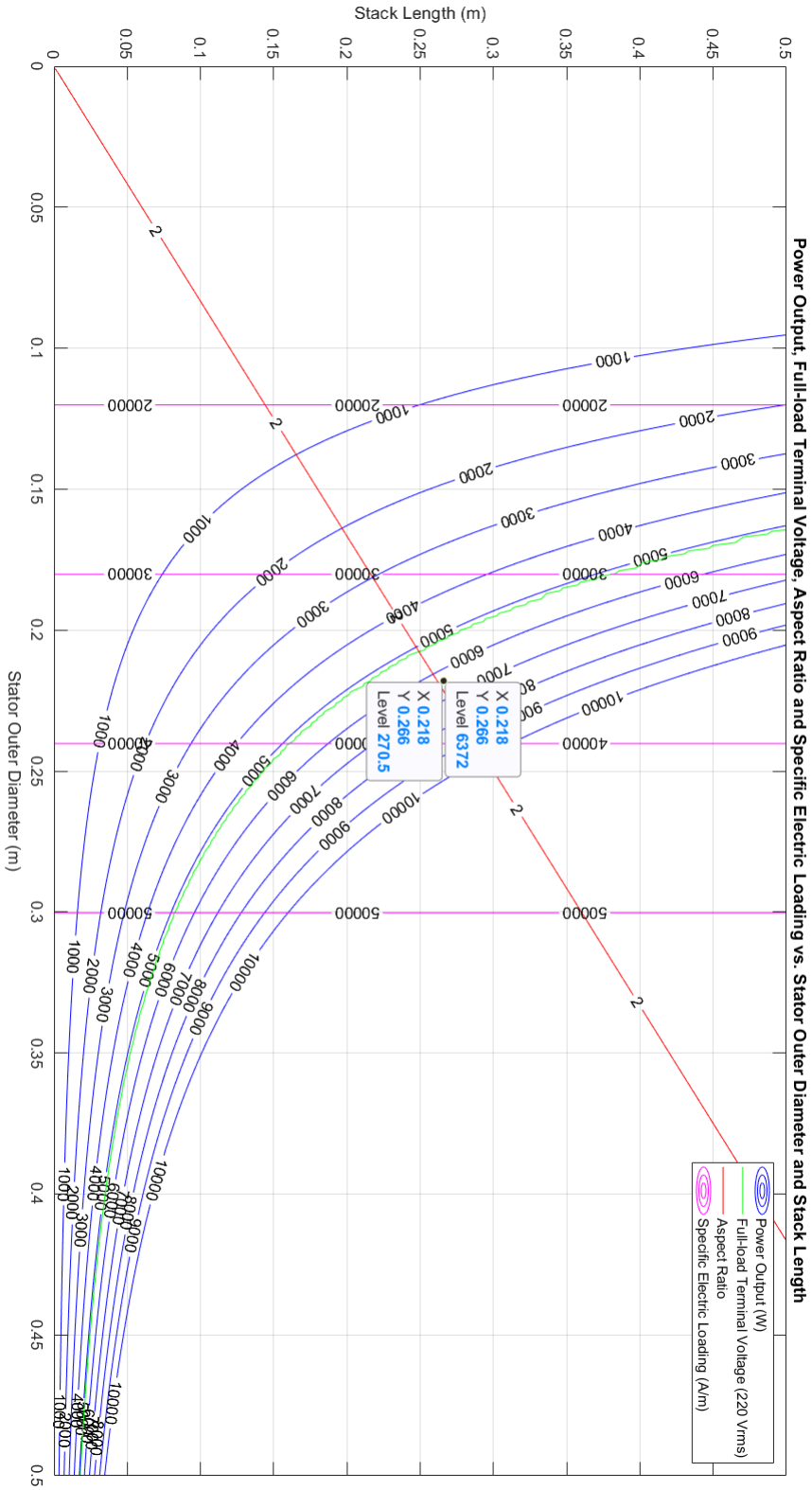

Figure 6.26: Stack length vs. stator outer diameter to achieve design requirements based on parametrically optimized ratios and estimates of K_d, B_{peak}, ϵ, $cos(\theta)$, H_{ribSO}, β_r, H_{ys}, β_{pm} and H_{yr}

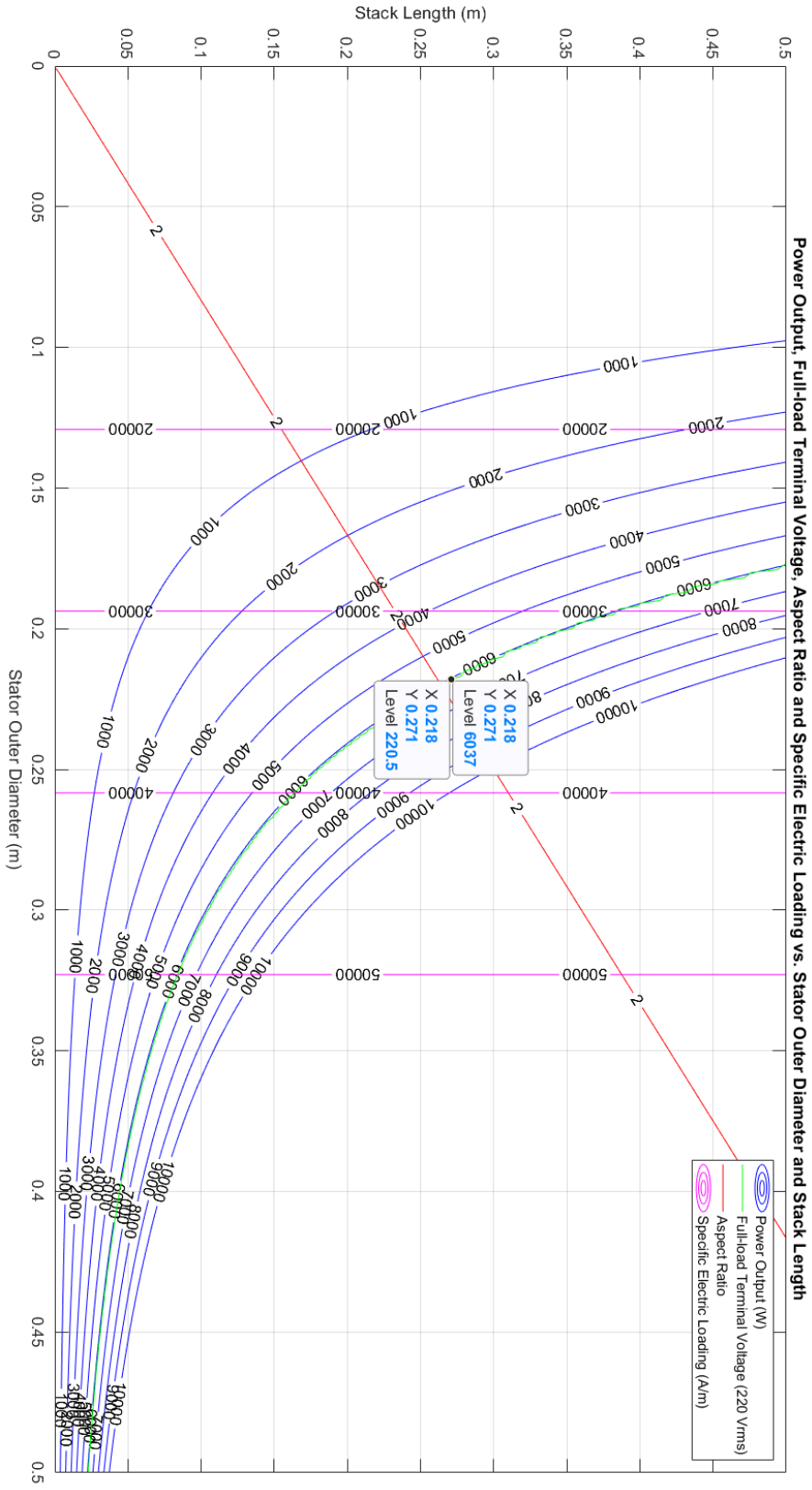

Figure 6.27: Stack length vs. stator outer diameter using $D_{ac} = 1.829$ mm and $J_s = 4.65$ A/mm^2

The new dimensions output the following design data:

Table 6.4: Analytical Design Data Using Parametrically Optimized Ratios

Parameter	**Design Data**	**Units**
P_{out}	6.037	kW
V_t	220.5	V_{rms}
D_{so}	0.218	m
D_{si}	0.1308	m
D_{ro}	0.1288	m
D_{ri}	0.035	m
D_g	0.1298	m
l_{st}	0.271	m
N_t	192	-
β_s	0.0094	m
β_r	0.012	m
H_{ys}	0.0086	m
H_{yr}	0.0387	m
β_{pm}	0.0068	m
A_s	34012	A/m
I_{rms}	12.0394	A
R_{ph}	0.6863	Ω
K_{es}	0.75	-
K_{er}	0.4147	-
K_{sio}	0.6	-

6.7.0.1 No-Load Results

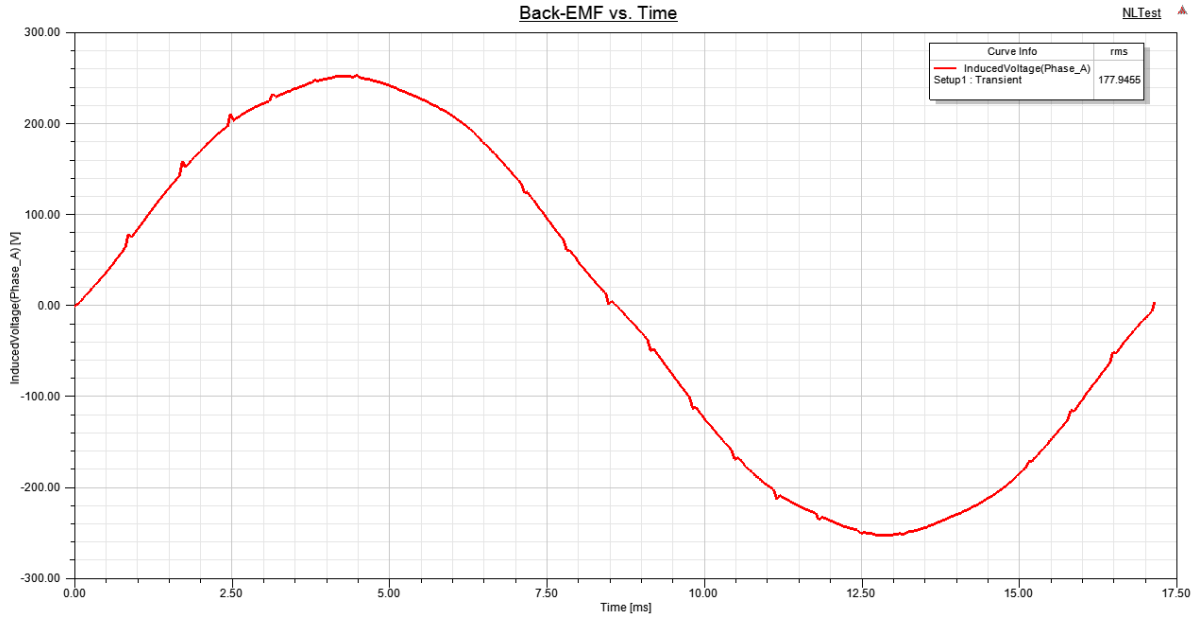

Figure 6.28: Back-EMF using ratios in Table 6.3 and dimensions in Table 6.4

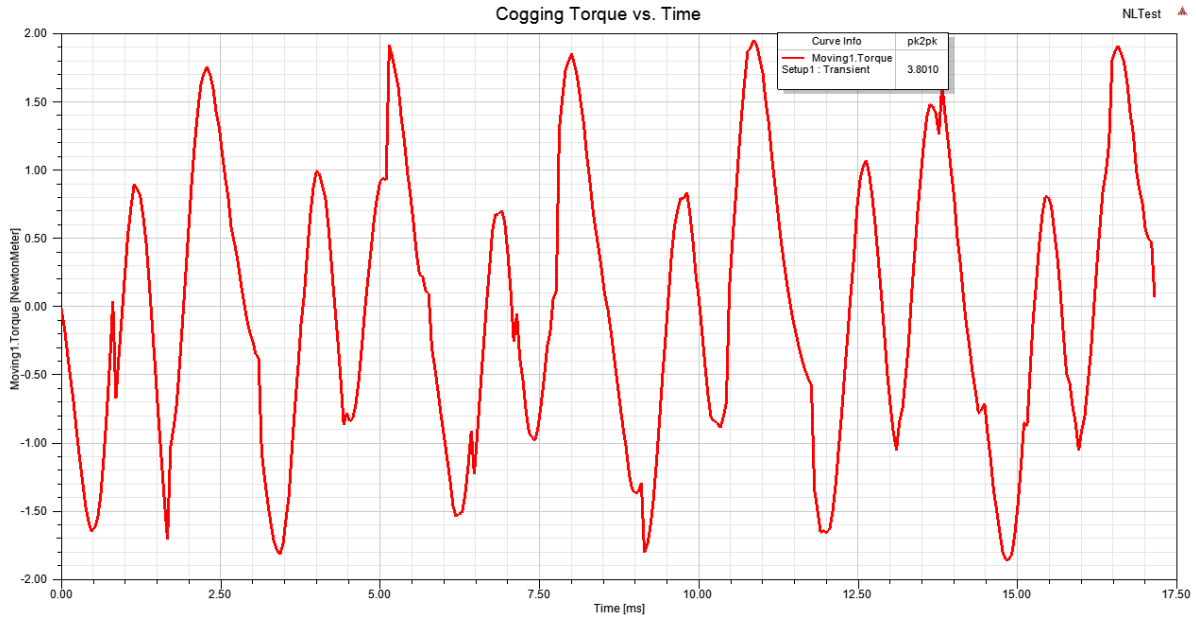

Figure 6.29: Cogging torque using ratios in Table 6.3 and dimensions in Table 6.4

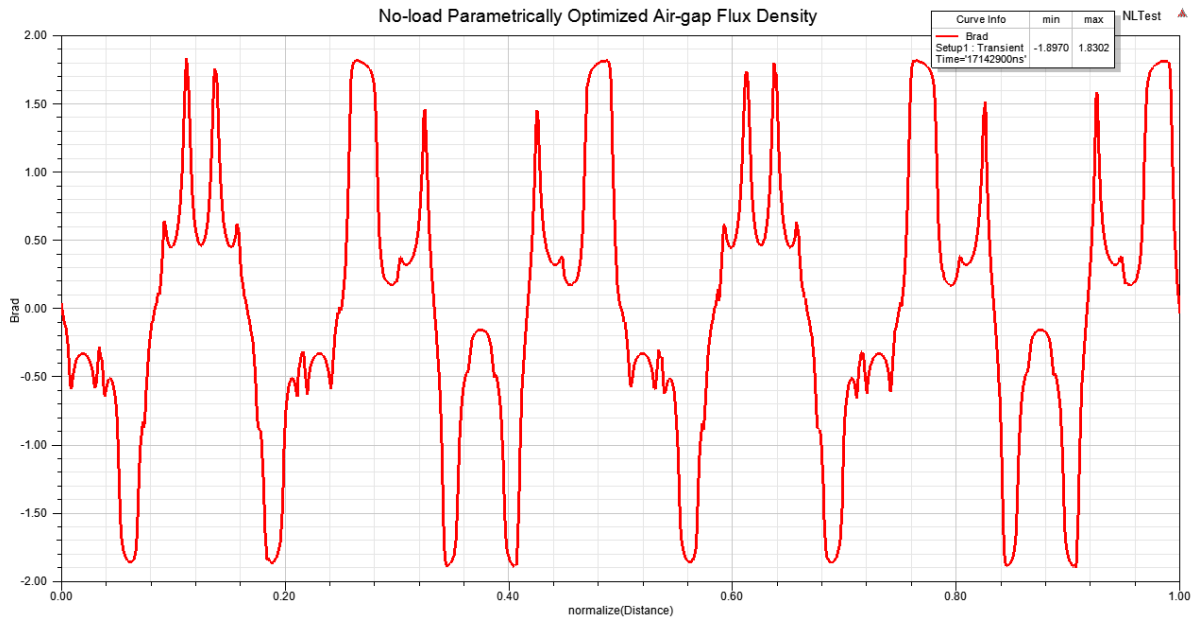

Figure 6.30: No-load air-gap flux density using ratios in Table 6.3 and dimensions in Table 6.4

6.7.0.2 Full-Load Results

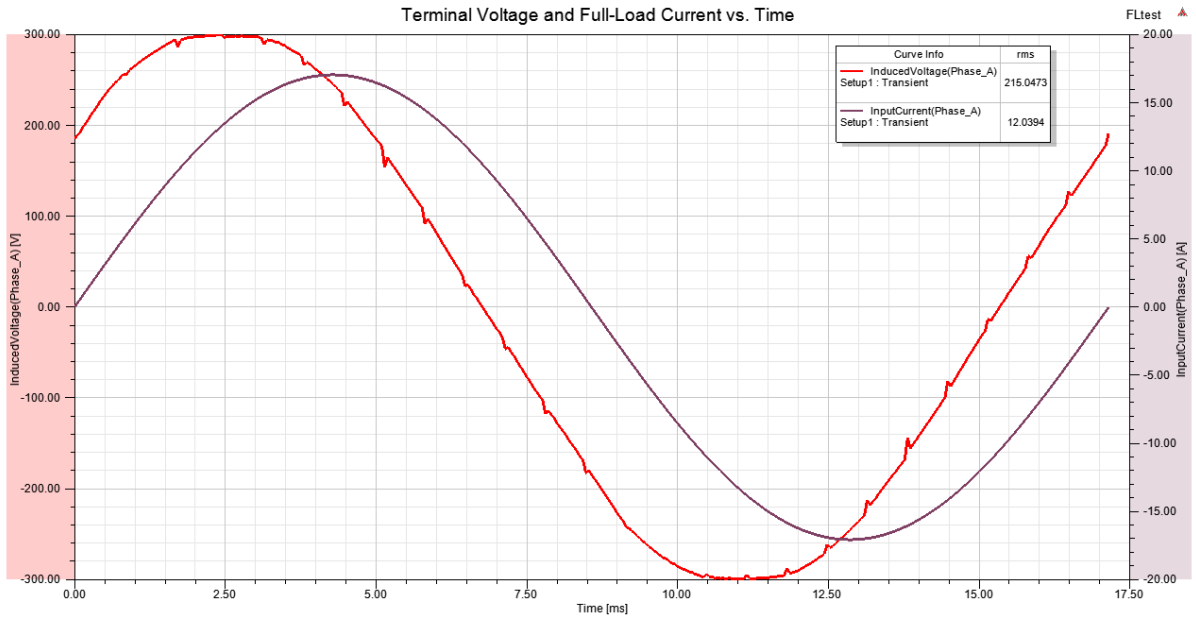

Figure 6.31: Full-load terminal voltage using ratios in Table 6.3 and dimensions in Table 6.4

Figure 6.32: Output power using ratios in Table 6.3 and dimensions in Table 6.4

Table 6.5: New Analytical vs. Parametrically Optimized (PO) FSPM Machine's Performance Characteristics

Parameter	**Analytical**	**PO FSPM**	**% Difference**	**Units**
E_{rms}	177.9495	177.9455	0	V_{rms}
V_{rms}	220.5074	215.0473	-2.48	V_{rms}
P_{out}	6.037	6.091	+0.89	kW
B_{peak}	1.897	1.897	0	T
K_d	0.7387	0.7387	0	-
ϵ	0.807	0.8275	+2.54	-
$cos(\theta)$	0.758	0.79	+4.22	-

The results in Table 6.5 confirm that all the parameters except for the terminal voltage are within close proximity to the design constraints. A parametric study on the length of the FSPM machine is therefore conducted and shown below in Figures 6.33 and 6.34. A terminal voltage of 220 V_{rms} is obtained when the stack length is 1.023 times the nominal, however, as expected, the output power increases from 6.091 kW to 6.23 kW, which is a 2.3% increase in output power. Therefore, constant back-and-forth adjustments will ensue if only the stack length and current density is changed and why an optimizer would prove to be valuable.

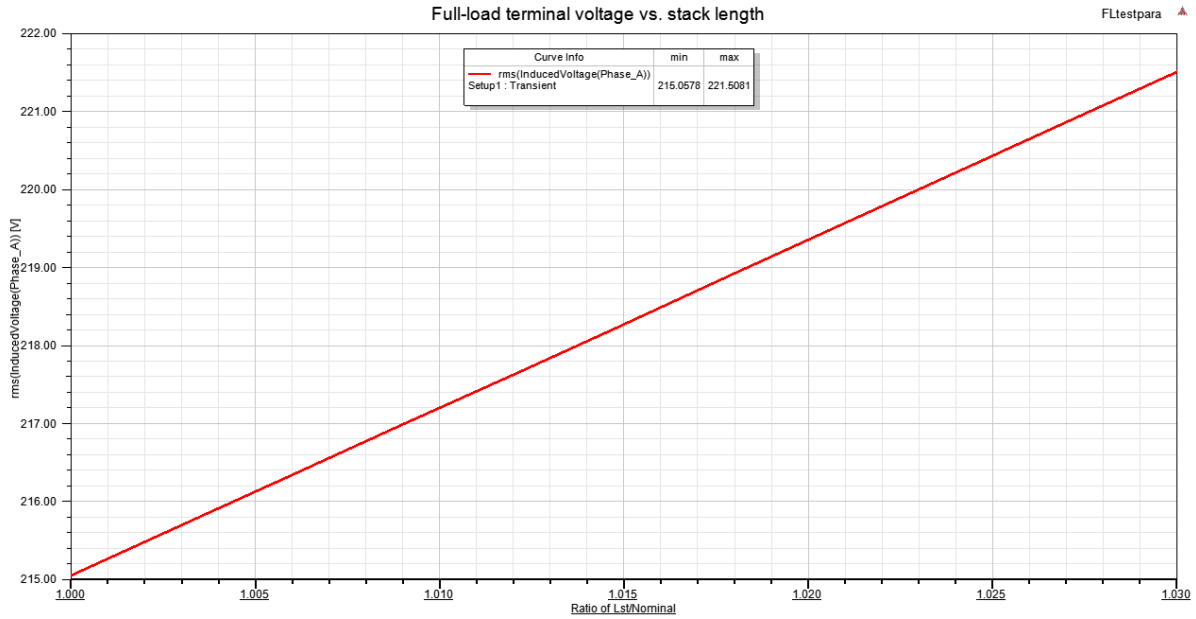

Figure 6.33: Parametric study of full-load terminal voltage vs. stack length

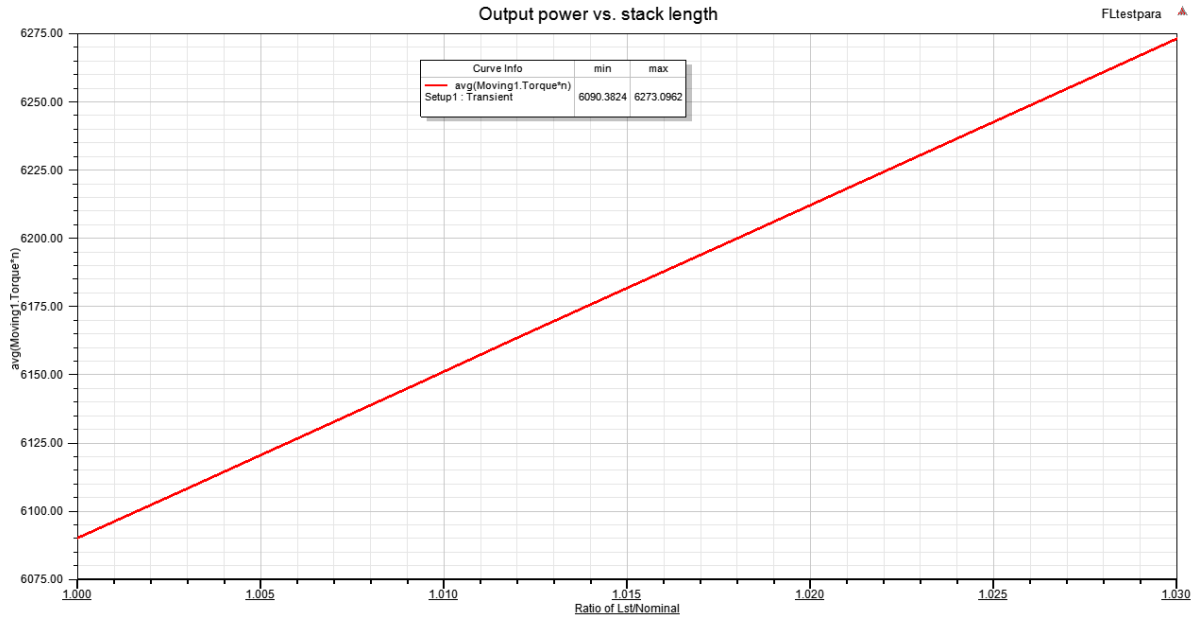

Figure 6.34: Parametric study of output power vs. stack length

The final design specifications for a parametrically optimized FSPM machine with a stack length of 1.023 times the nominal are summarized from Figures 6.35-6.38 and in Table 6.6.

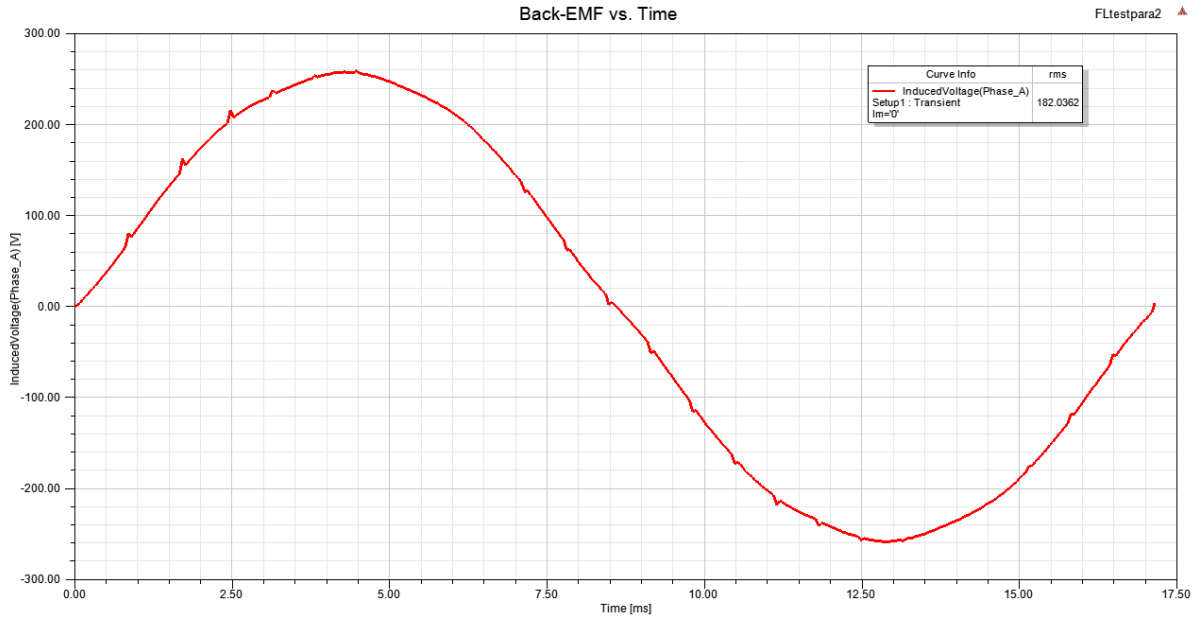

Figure 6.35: Back-EMF vs. time for the final parametrically optimized FSPM machine

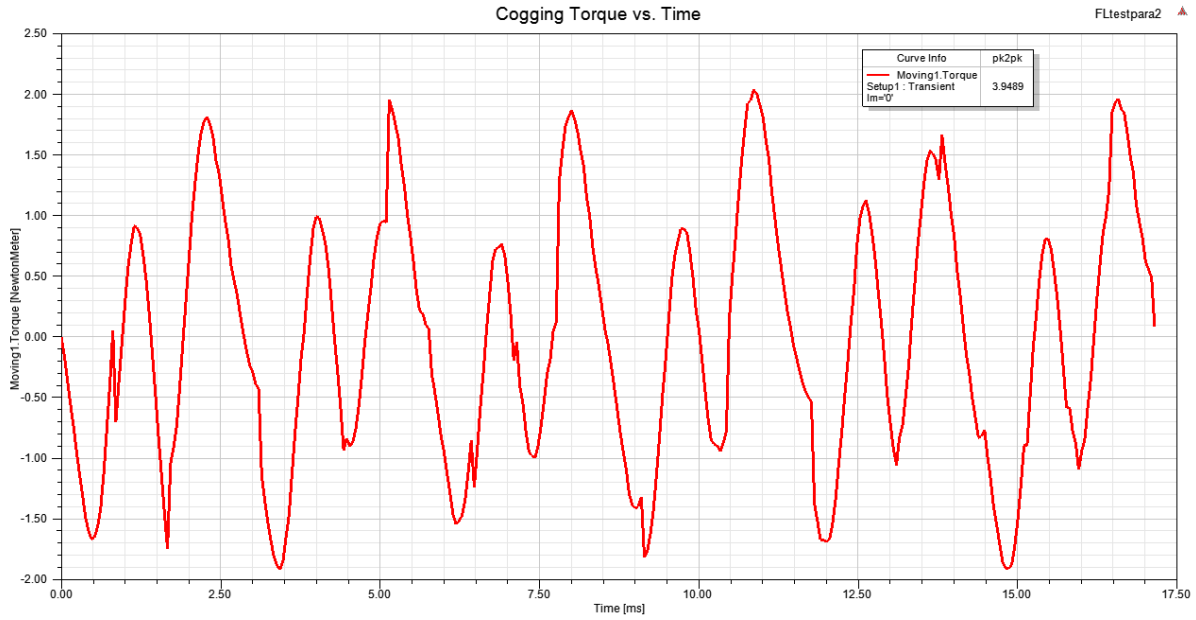

Figure 6.36: Cogging torque vs. time for the final parametrically optimized FSPM machine

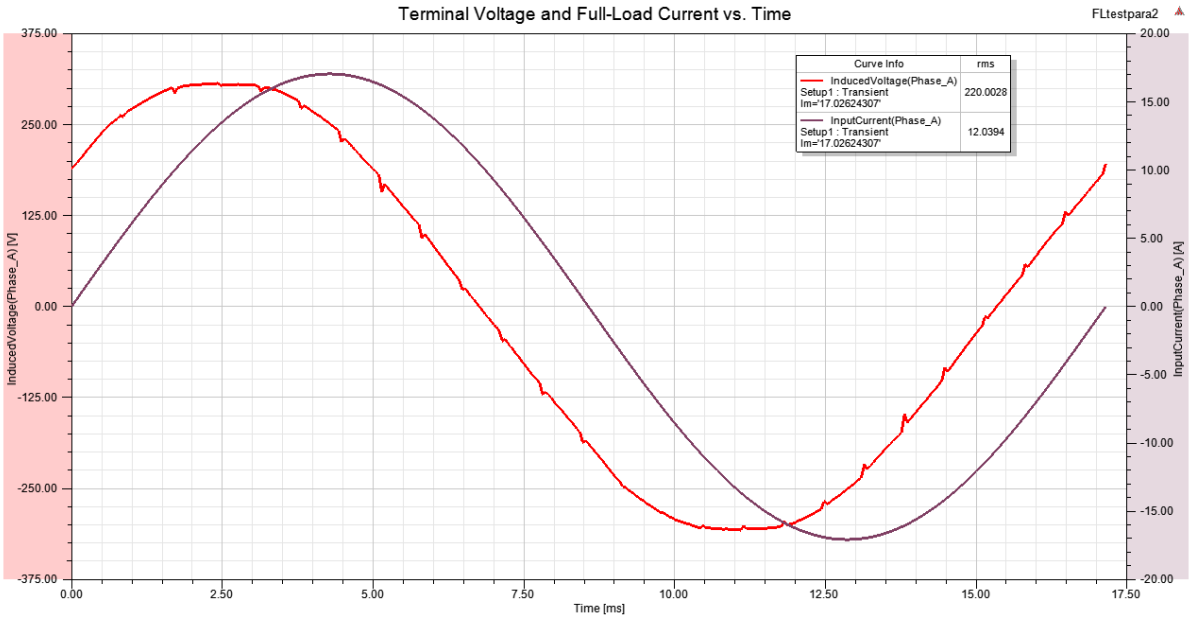

Figure 6.37: Full-load terminal voltage and current vs. time for the final parametrically optimized FSPM machine

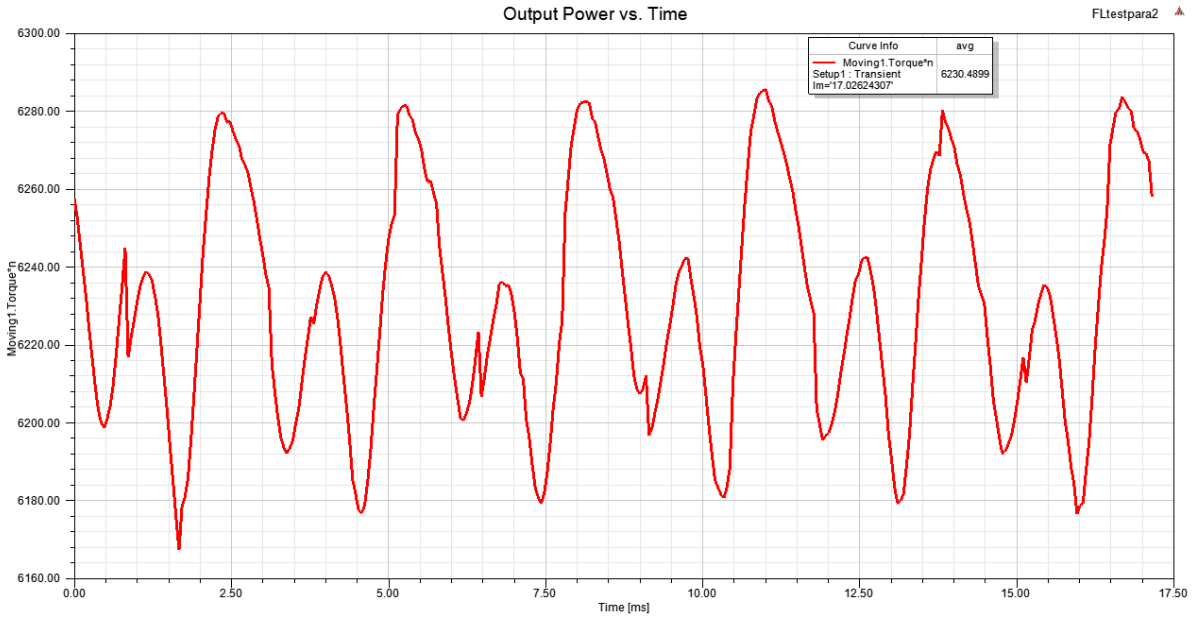

Figure 6.38: Output power vs. time for the final parametrically optimized FSPM machine

Table 6.6: Design Data Using Parametrically Optimized Ratios

Parameter	**Design Data**	**Units**
P_{out}	6.23	kW
V_t	220	V_{rms}
D_{so}	0.218	m
D_{si}	0.1308	m
D_{ro}	0.1288	m
D_{ri}	0.035	m
D_g	0.1298	m
l_{st}	0.2777	m
N_t	192	-
β_s	0.0094	m
β_r	0.012	m
H_{ys}	0.0086	m
H_{yr}	0.0387	m
β_{pm}	0.0068	m
A_s	34012	A/m
I_{rms}	12.0394	A
R_{ph}	0.6863	Ω
K_{es}	0.75	-
K_{er}	0.4147	-
K_{sio}	0.6	-

Chapter 7

Optimization

This chapter provides a brief overview of the selected optimizer that is used within Ansys Maxwell and includes the design of the final FSPM machine. A comparison between the parametrically optimized FSPM machine and the optimizer's design is done to determine any changes in optimal ratios and how the optimizer changed it to meet the design specifications.

Optimization of a machine is important to achieve the best possible performance. Parametric studies that's performed in chapter 6 are valuable as it show designers the effect of changing individual geometric parameters, however, this is seen as a manual optimization of individual parameters. While finding the optimal value for a specific parameter, it will change the optimal parameters that was found in previous studies because they are not optimized concurrently. Therefore, automated optimization techniques optimize the specified parameters concurrently, giving the most optimal design point. A comparison between the optimized parameters and those found using the parametric studies are discussed in this section.

According to [55], there are five optimization techniques that can be used within Ansys Maxwell, with Sequential Non-linear Programming (SNLP) being the general choice. It should be noted that all five optimizers assume that the optimal design solution is in close proximity of the nominal design solution, therefore, it is important to first perform a parametric study to manually attempt to achieve the design goals. The Sequential Non-Linear Programming (SNLP) optimizer is therefore used in this dissertation. Its ability to optimize much faster than other optimizers and the logical approach it follows to reach the goal made it attractive. More information on how the different optimizers work can be found in [55].

7.1 Optimization Setup and Results

The optimizer was set to allow variations in K_{er}, β_{pm}, H_{yr}, I_{rms}, l_{st} and N_t in order to achieve an output power of 6.05 kW at 220 V_{rms}. A maximum number of 50 evaluations were set and the most optimal solution is found at the 49th evaluation as indicated in Figure 7.1. A cost of 0.027377 is obtained, meaning that the solution has a small error with respect to the goals. The parameters as found by the optimizer are summarized in Table 7.1.

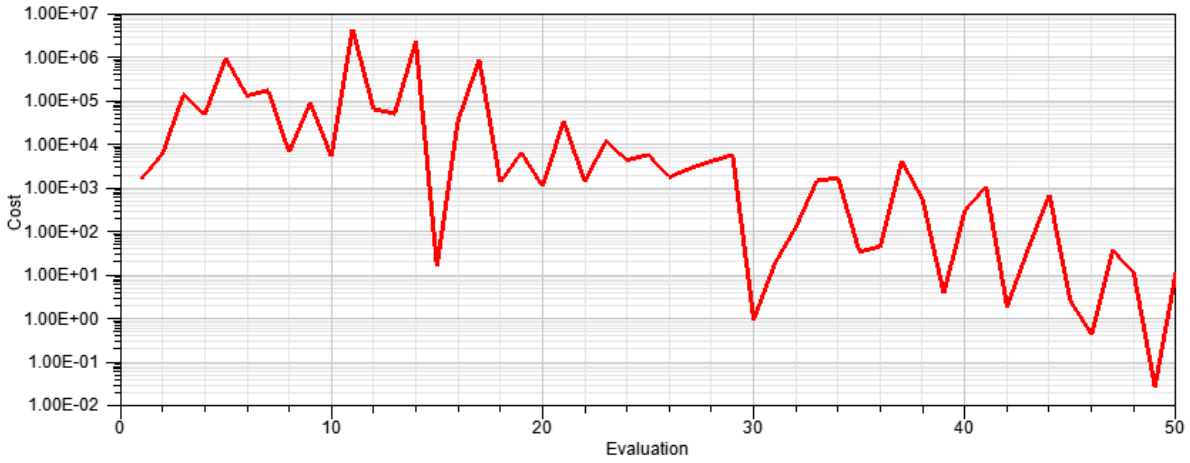

Figure 7.1: Cost function vs. number of evaluations (lower is better)

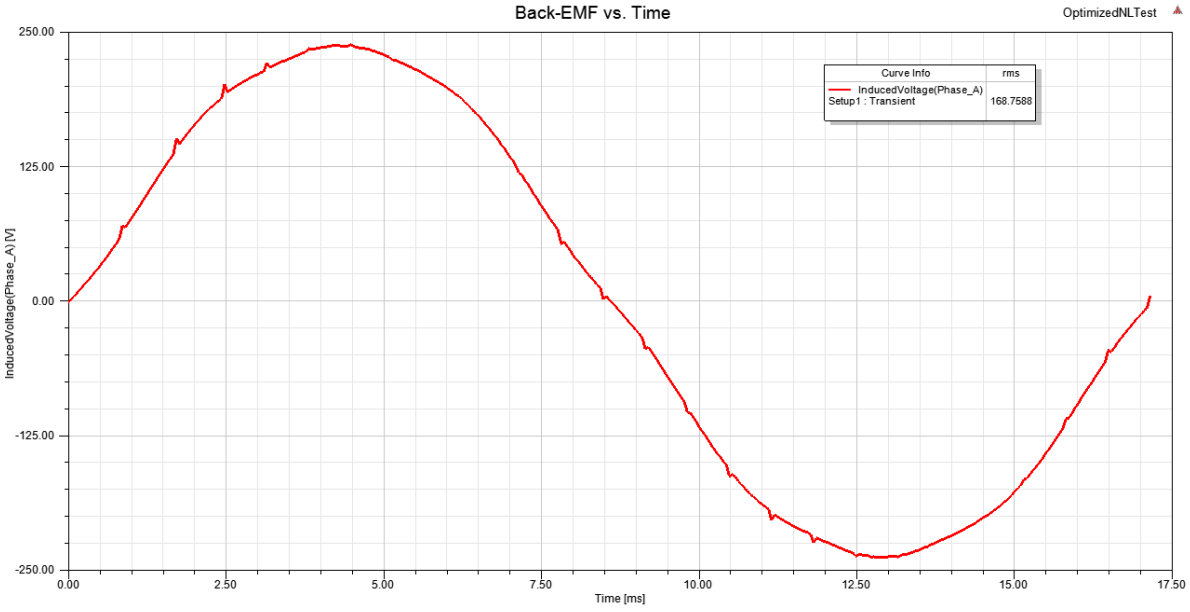

Figure 7.2: Optimized back-EMF vs. time

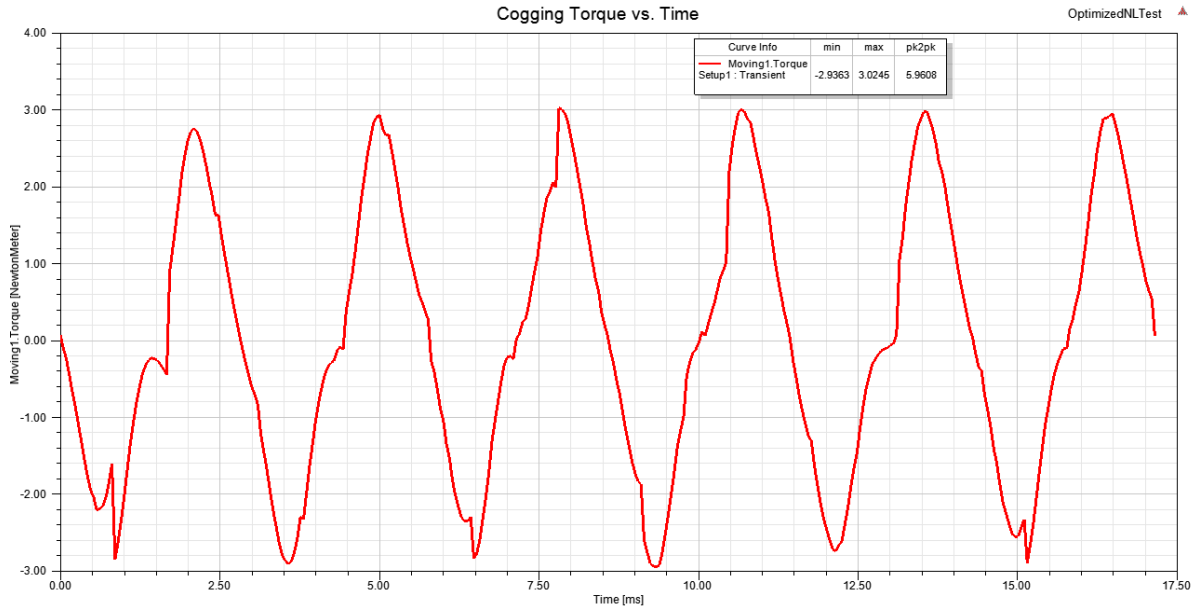

Figure 7.3: Optimized cogging torque vs. time

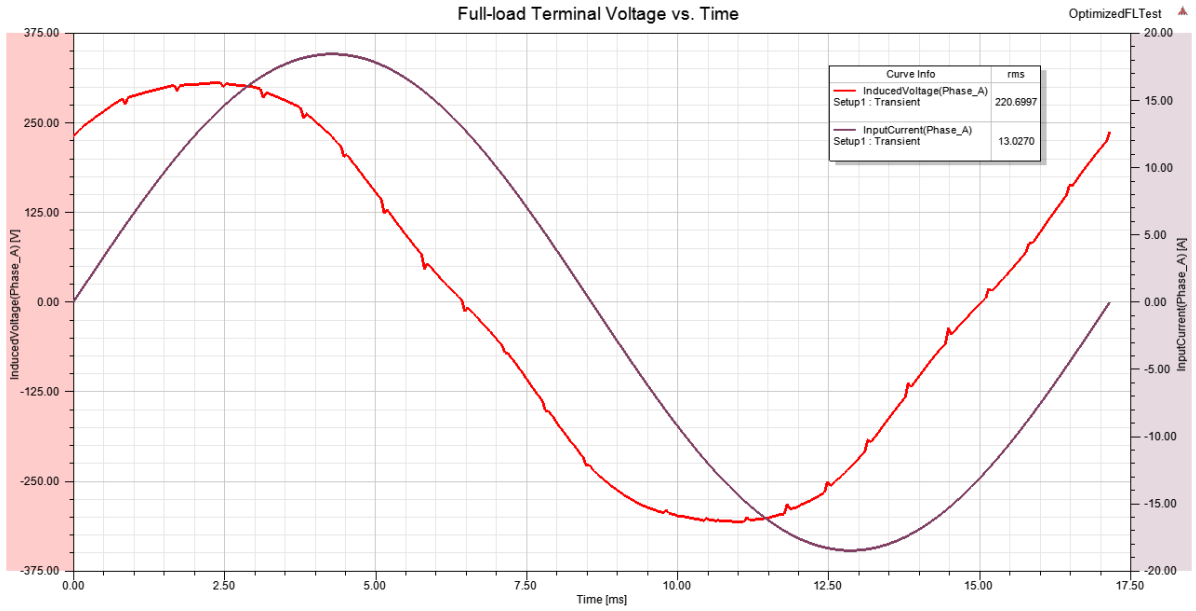

Figure 7.4: Optimized full-load terminal voltage and current vs. time

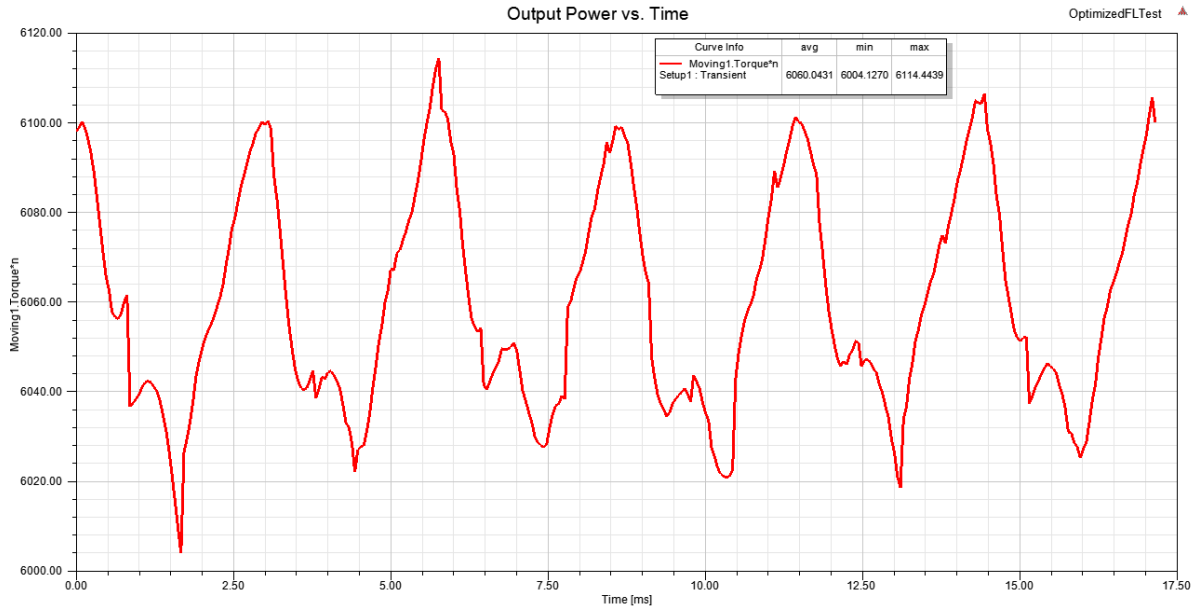

Figure 7.5: Optimized output power vs. time

Table 7.1: Optimized Parameters Using Sequential Non-Linear Programming Optimizer

Parameter	**Initial Value**	**Optimized Value**	**Units**
P_{out}	6.091	6.06	kW
V_t	215.0473	220.7	V_{rms}
K_{er}	0.4147	0.4429	-
β_{pm}	0.0068	0.005958	m
H_{yr}	0.0387	0.0369	m
I_{rms}	12.0394	13.027	A
l_{st}	0.271	0.2488	m
N_t	192	196	-

Table 7.2 below shows a comparison between the ratios determined from the parametric studies, and those derived by the optimizer to achieve the goals.

Table 7.2: Geometric Ratios Obtained from Parametric Analysis vs. Optimizer

Parameter	**Parametric Study Ratio**	**Optimizer Ratio**	**Units**
β_r	1.4	1.5	-
β_{pm}	0.8	0.7	-

Table 7.2: Geometric Ratios Obtained from Parametric Analysis vs. Optimizer (Continued)

Parameter	**Parametric Study Ratio**	**Optimizer Ratio**	**Units**
H_{yr}	1.3	1.24	-

The FSPM machine design data from the optimizer is summarized in Table 7.3 below:

Table 7.3: Design Data Using Optimizer

Parameter	**Design Data**	**Units**
P_{out}	6.06	kW
V_t	220.7	V_{rms}
D_{so}	0.218	m
D_{si}	0.1308	m
D_{ro}	0.1288	m
D_{ri}	0.035	m
D_g	0.1298	m
l_{st}	0.2488	m
N_t	196	-
β_s	0.0094	m
β_r	0.012	m
H_{ys}	0.0086	m
H_{yr}	0.0369	m
β_{pm}	0.005958	m
A_s	34012	A/m
I_{rms}	13.027	A
R_{ph}	0.6863	Ω
K_{es}	0.75	-
K_{er}	0.4429	-
K_{sio}	0.6	-

7.2 Finalized FSPM Machine Design

After the design is completed in optimization, it's sent out to manufacturers for quotations. The manufacturers can only manufacture according to specific tolerances and that must be taken into account, especially in the critical area such as the air-gap. The manufacturers used for this design have provided a tolerance of ±0.1 mm and ±0.2 mm for the steel laminations and the permanent magnets respectively.

The optimized design is therefore slightly altered to adhere to changes in geometrical dimensions as requested by manufacturers. The manufacturers requested to remove the stator outer rib as it would make assembling the machine much easier. Instead, tiny dovetails were added to the stator laminations that ensures the permanent magnets are kept in place. The shaft diameter was also increased to 40 mm. These alterations caused some deviation in the rated results and the current density needed to be increased to compensate for the changes.

Figures 7.6 - 7.10 show the nominal waveforms of the back-EMF, cogging torque, full-load terminal voltage, output power and losses respectively. The final back-EMF waveform is sinusoidal with a voltage of 156.84 V_{rms} and a cogging torque of 3.5 Nm_{pk-pk} is obtained, which is only 1.42 % of the rated torque. The full-load terminal voltage is still close to the design specification at 219.7 V_{rms} and the output power increased to 6460.21 W with a ripple of 1.15 %. The increased power is acceptable since the tolerance on the PMs can cause a reduction in output power. Note that the relationship between the tolerances of the PMs and steel laminations on the performance of the FSPM machine is non-linear. The total losses of the designed FSPM machine is 570.31 W, which indicates an efficiency of 91.17 %.

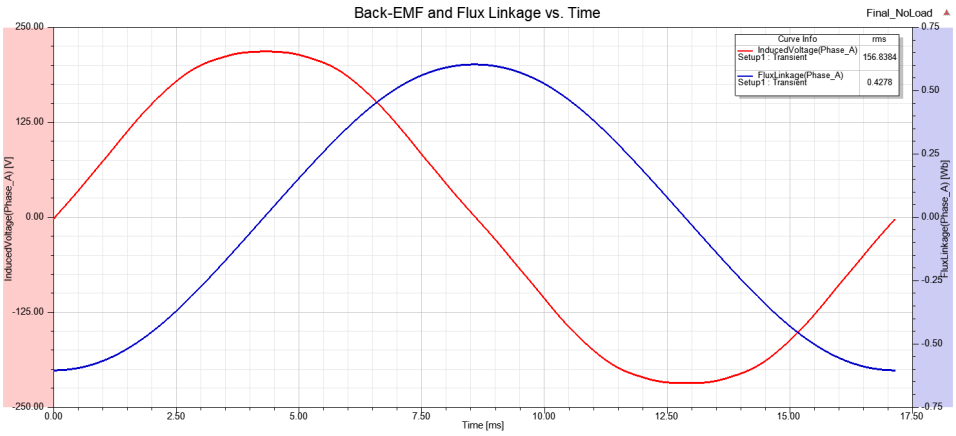

Figure 7.6: Final nominal back-EMF vs. time

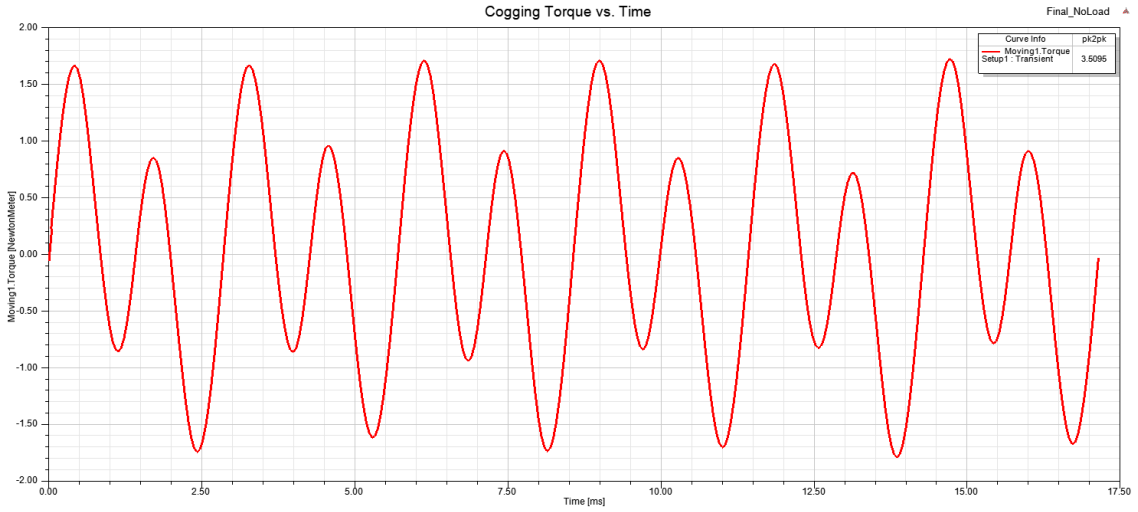

Figure 7.7: Final nominal cogging torque vs. time

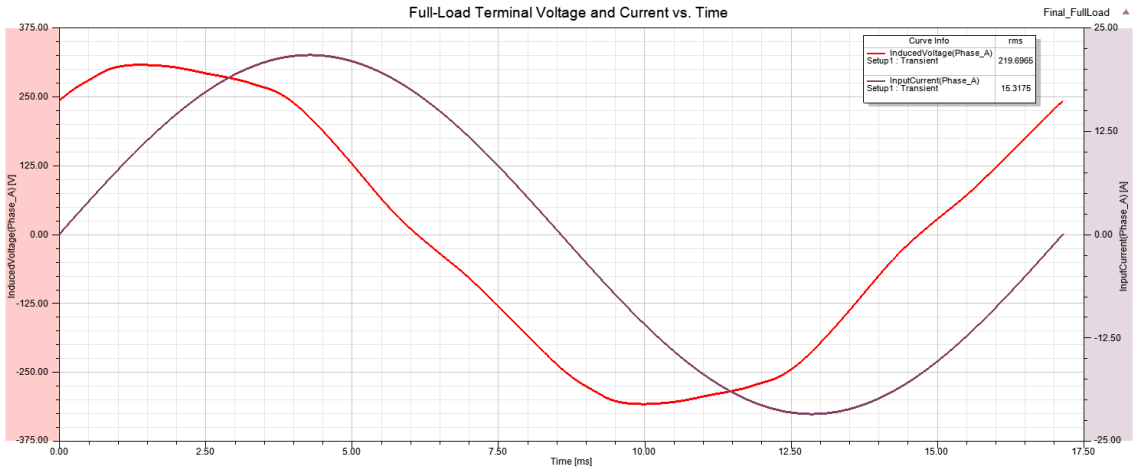

Figure 7.8: Final nominal full-load terminal voltage vs. time

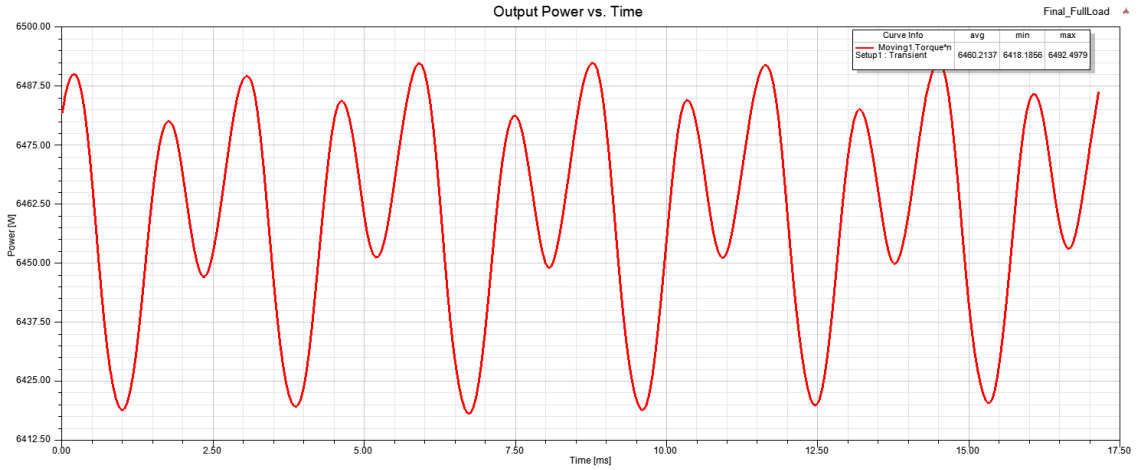

Figure 7.9: Final nominal output power vs. time

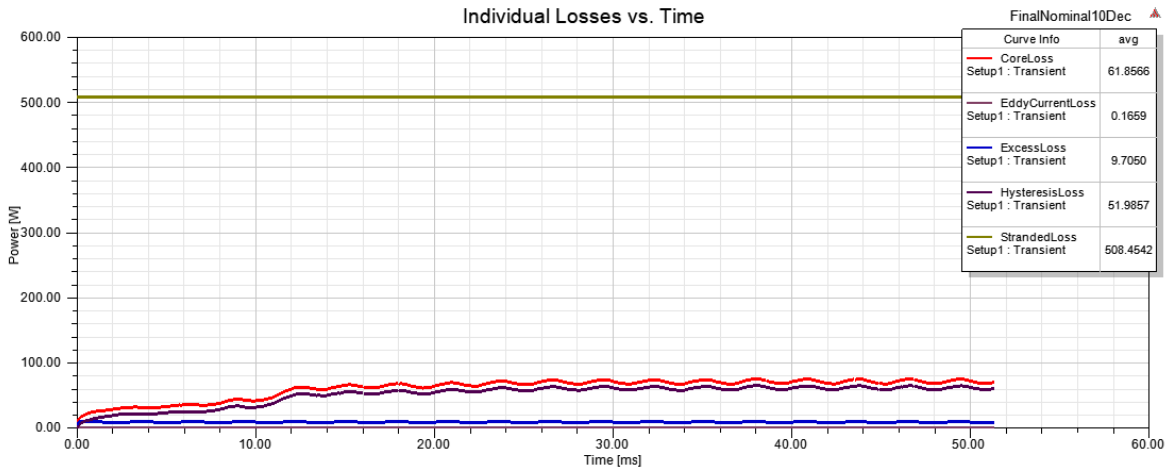

Figure 7.10: Final losses at rated power vs. time

A current angle study was performed and indicated that the designed FSPM machine is indeed starting in the d-axis position and operated at maximum torque using the q-axis current control.

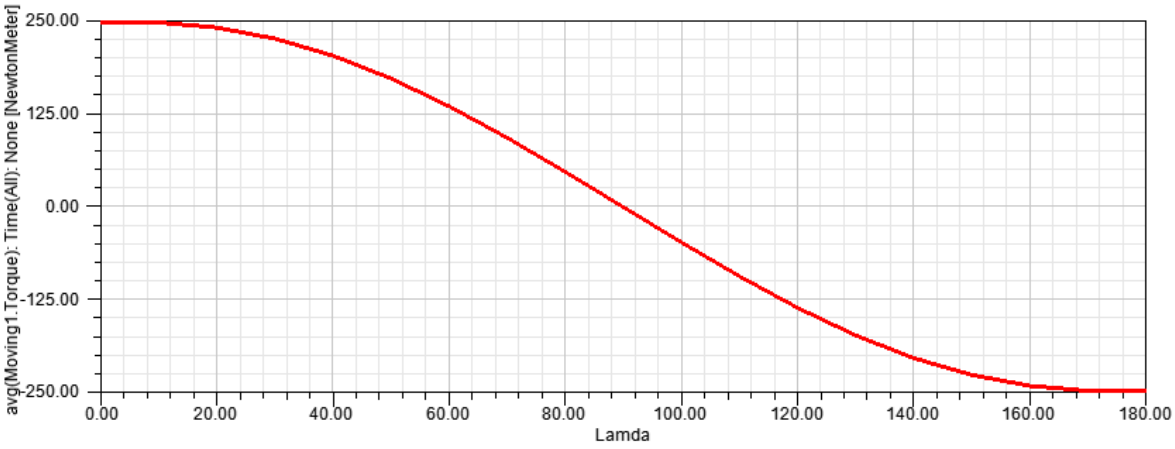

Figure 7.11: Variation in current angle on average output torque

The final FSPM machine design data that is used for implementation is summarized in Table 7.4 below:

Table 7.4: Final FSPM Design Data

Parameter	**Design Data**	**Units**
P_{out}	6.46	kW
V_t	219.7	V_{rms}
D_{so}	0.218	m
D_{si}	0.1308	m
D_{ro}	0.1288	m
D_{ri}	0.04	m
D_g	0.1298	m
l_{st}	0.2505	m
N_t	196	-
β_s	0.0094	m
β_r	0.012	m
H_{ys}	0.0086	m
H_{yr}	0.0369	m
β_{pm}	0.005958	m
A_s	44174.4	A/m
I_{rms}	15.3175	A
R_{ph}	0.6863	Ω
K_{es}	0.75	-
K_{er}	0.4429	-
K_{sio}	0.6	-

Chapter 8

Core Loss Analysis

This chapter contains an in-depth core loss analysis on the designed FSPM machine to identify the losses in each part of the machine's core.

8.1 Modelling of Core Losses

The core losses consist of hysteresis, eddy current and excess losses as detailed in [56, 57] and is simply a summation of the three losses:

$$P_c = P_h + P_e + P_{ex} \tag{8.1}$$

The individual loss terms are expanded by Bertotti's three-term model:

$$P_c = k_h f_e B^{\beta} + k_e f_e^2 B^2 + k_{ex} f_e^{1.5} B^{1.5} \tag{8.2}$$

Where k_h, k_e, k_{ex}, B and β are the hysteresis-, eddy current-, excess loss coefficients, peak sinusoidal flux density and Steinmetz constant respectively [56, 57]. The Steinmetz constant β is approximately equal to 2 for modern magnetic materials [58] and is used in this analysis.

The method used in this analysis to determine the individual core loss components requires analytical formulae to be created that represent the loss curves at different frequencies. (8.2) needs to be modified to represent a quadratic equation so that polynomial curve fitting may be used to extract the loss coefficients.

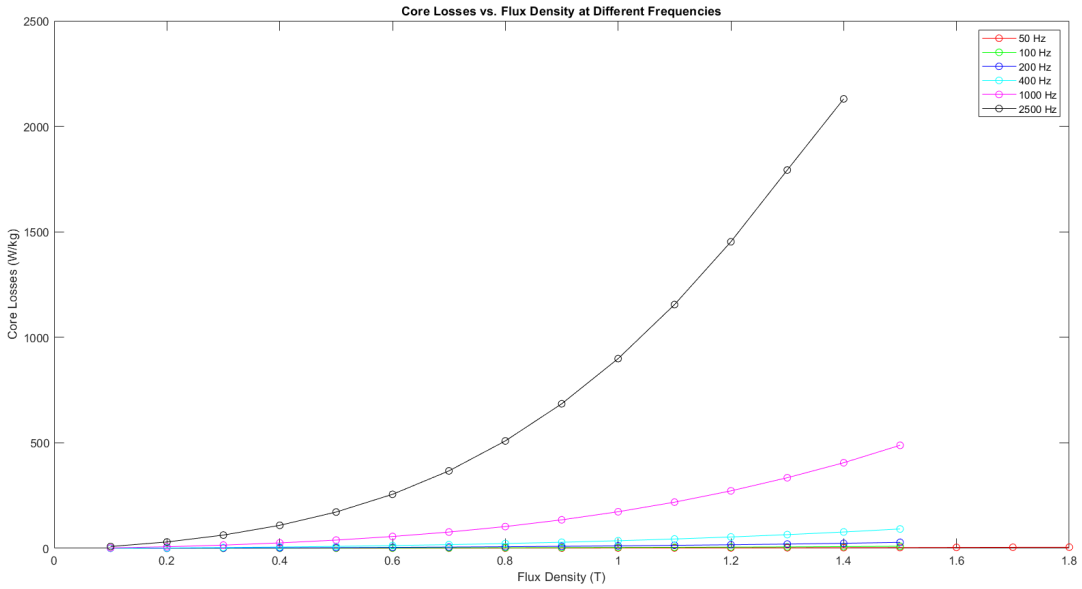

Figure 8.1: Core losses versus flux density for different frequencies as specified by the manufacturer for M400-50A silicone steel

To represent (8.2) in a quadratic form, it is divided by the frequency to show the power loss per frequency versus the square root of the frequency for different flux densities.

$$\frac{P_c}{f_e} = k_e B^2 \sqrt{f_e}^2 + k_{ex} B^{1.5} \sqrt{f_e} + k_h B^{\beta} \tag{8.3}$$

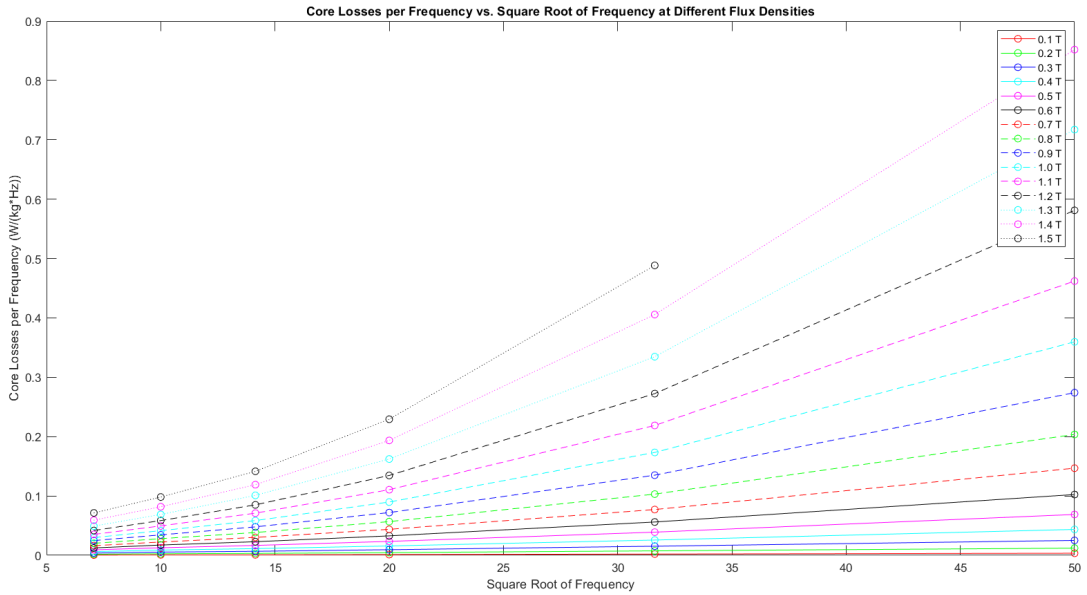

Figure 8.2: Core losses per frequency versus the square root of the frequency for different flux densities

It should be noted that Figure 8.2 only includes data from 0.1 T - 1.5 T because not enough data is available from all frequencies to perform the polynomial curve fitting for flux densities above 1.5 T.

Polynomial curve fitting is applied to all 15 curves in Figure 8.2 by using the script in Appendix A.4. The coefficients are received in the form of:

$$y = X\sqrt{f_e}^2 + Y\sqrt{f_e} + Z \tag{8.4}$$

where X, Y and Z are found by:

$$\begin{aligned} X &= k_e B^2 \\ Y &= k_{ex} B^{1.5} \\ Z &= k_h B^{\beta} \end{aligned} \tag{8.5}$$

From Table 8.1 it's clear that k_e, k_{ex} and k_h change with different flux densities, with the hysteresis coefficient being much higher than the eddy current and excess coefficients. Figures 8.3 to 8.5 show this change with respect to the flux density.

Table 8.1: X, Y, Z, k_e, k_{ex} and k_h coefficients at different flux densities

B	**X**	**Y**	**Z**	k_e	k_{ex}	k_h
0.1	2.26E-07	5,81E-05	1,42E-07	2,26E-05	1,84E-03	1,42E-05
0.2	7,26E-07	1,97E-04	3,88E-04	1,81E-05	2,21E-03	9,71E-03
0.3	1,89E-06	3,87E-04	1,07E-03	2,09E-05	2,35E-03	1,18E-02
0.4	4,56E-06	6,07E-04	1,89E-03	2,85E-05	2,40E-03	1,18E-02
0.5	9,77E-06	8,25E-04	3,10E-03	3,91E-05	2,33E-03	1,24E-02
0.6	1,76E-05	1,08E-03	4,18E-03	4,90E-05	2,33E-03	1,16E-02
0.7	3,08E-05	1,27E-03	6,04E-03	6,29E-05	2,17E-03	1,23E-02
0.8	4,89E-05	1,47E-03	7,82E-03	7,64E-05	2,06E-03	1,22E-02
0.9	7,21E-05	1,68E-03	9,75E-03	8,90E-05	1,97E-03	1,20E-02
1.0	1,01E-04	1,91E-03	1,16E-02	1,01E-04	1,91E-03	1,16E-02
1.1	1,36E-04	2,19E-03	1,32E-02	1,12E-04	1,90E-03	1,09E-02
1.2	1,76E-04	2,54E-03	1,48E-02	1,22E-04	1,93E-03	1,02E-02
1.3	2,20E-04	3,05E-03	1,55E-02	1,30E-04	2,06E-03	9,18E-03
1.4	2,51E-04	4,27E-03	1,29E-02	1,28E-04	2,58E-03	6,59E-03
1.5	4,10E-04	1,07E-03	4,46E-02	1,82E-04	5,82E-04	1,98E-02

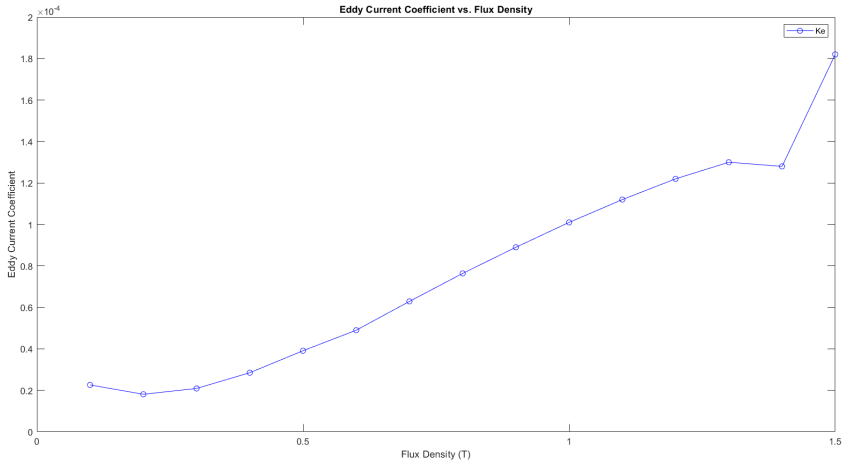

Figure 8.3: Eddy current coefficient versus flux density

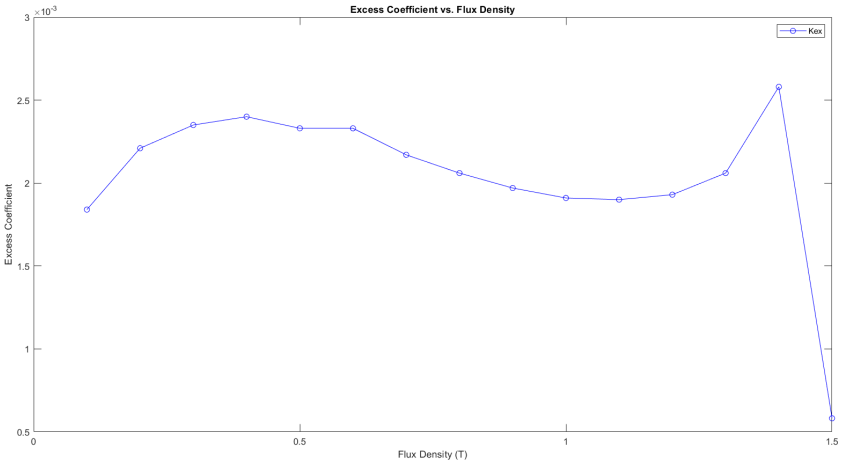

Figure 8.4: Excess current coefficient versus flux density

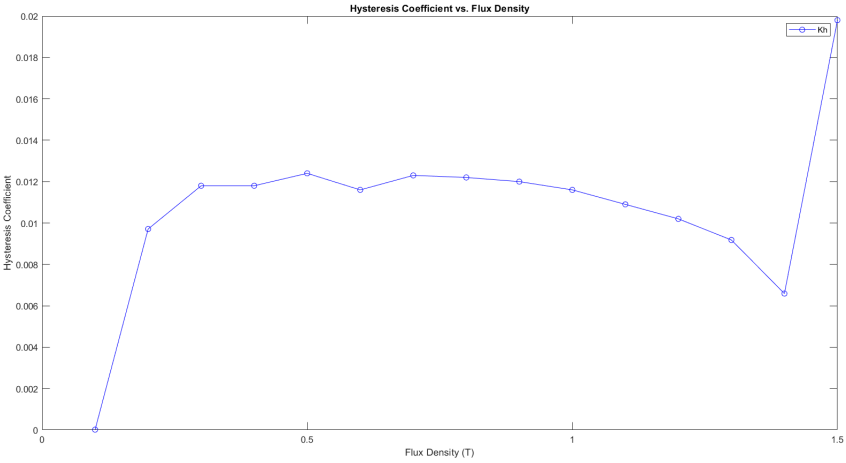

Figure 8.5: Hysteresis coefficient versus flux density

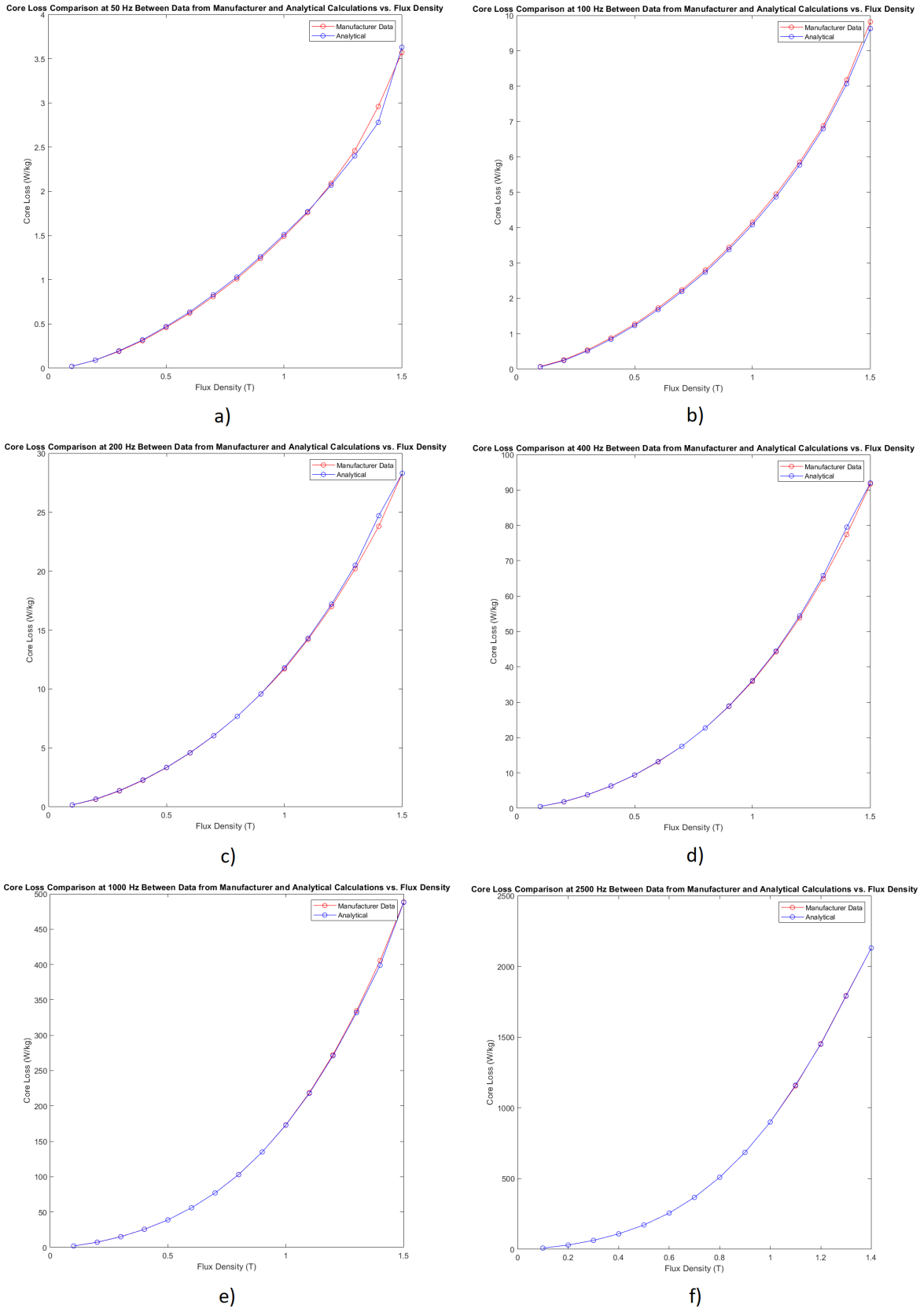

Figure 8.6: Core loss comparison between data from manufacturer and analytical computations at a) 50 Hz b) 100 Hz c) 200 Hz d) 400 Hz e) 1000 Hz f) and 2500 Hz

The method used by the Ansys Maxwell software to determine the loss coefficients k_e, k_{ex} and k_h, finds fixed loss coefficients at each frequency and can thus be used to determine the losses at any flux density. Contrary, the method used in this dissertation finds fixed loss coefficients at each flux density and can therefore be used to determine the losses at any frequency. The method that the Ansys Maxwell software uses also has the benefit of analysing the individual core loss components, however, the approach used in this dissertation provides a more accurate total core loss estimation when compared to the manufacturer's data.

To validate the accuracy of the analytical model, it's compared to the data from the manufacturer and depicted in Figure 8.6. The analytical model correlates very well with the data from the manufacturer and can be used to determine the core losses at any frequency. An important observation that's made is the lack of core loss data for higher flux densities at higher frequencies. This limits the analytical model to find core losses at flux densities up to 1.5 T, which is a problem for FSPM machines that have flux densities close to and above the saturation flux density of 1.8 T.

8.2 Determination of Core Losses

Core losses can be derived using Bertotti's three model term and from it, it's clear that the formula is dependent on the frequency and flux density in the specific section of the core. As found in [59], the frequency of the flux in the specific parts of the core in a switched reluctance machine is not constant throughout. In Figure 8.7, the frequencies in zones 1, 1', 1", 3 and 3' are f_{base}; $m * f_{base}$ in zone 2; and f_{base}/N_r in zones 4, 4' and 5. Therefore, since the FSPM machine has a very similar structure to the switched reluctance machine, the same principles can be applied.

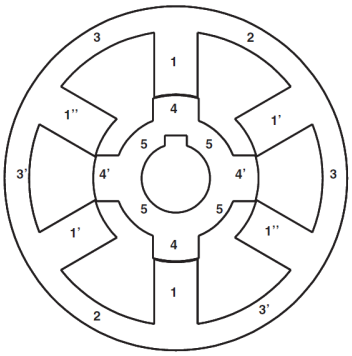

Figure 8.7: Switched reluctance machine's structure with changes in the flux's frequency in the different zones [59]

The different flux waveforms are shown in Figures 8.8 to 8.10 and in Table 8.2.

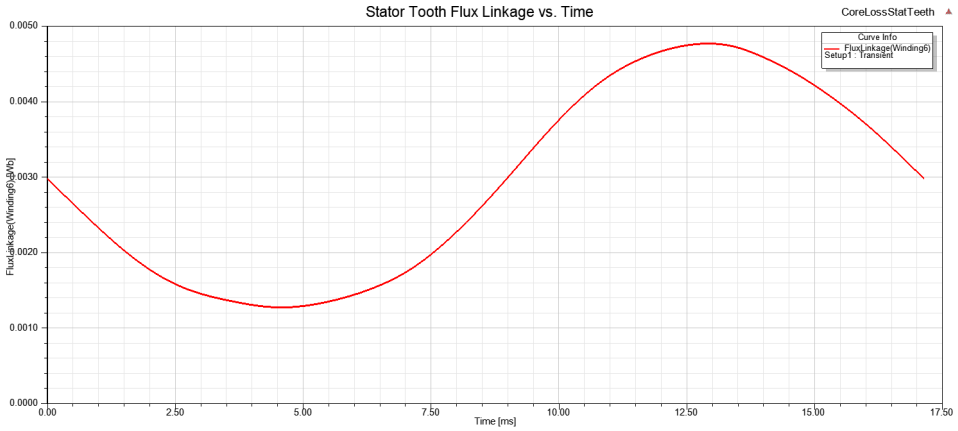

Figure 8.8: Flux in a stator tooth vs. Time

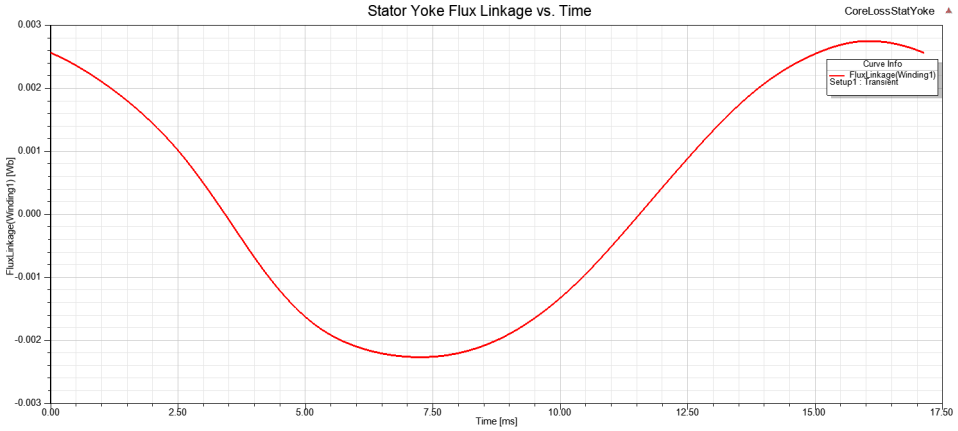

Figure 8.9: Flux in the stator back-iron vs. Time

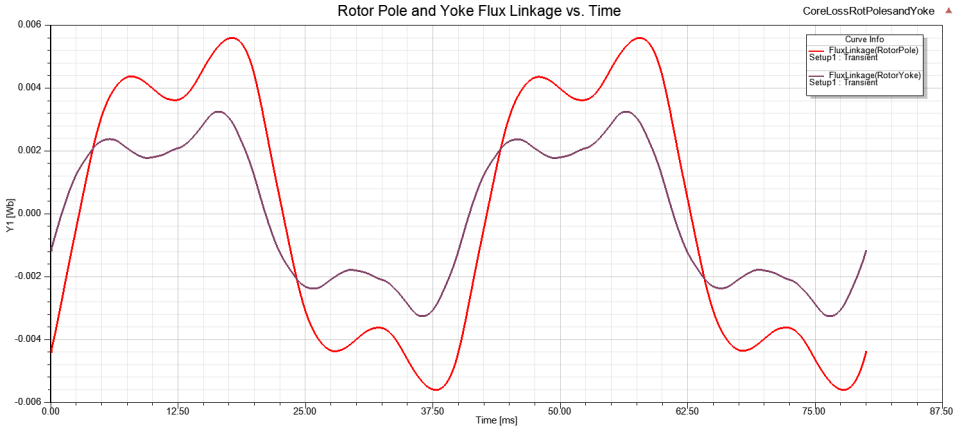

Figure 8.10: Flux in a rotor pole and back-iron vs. Time

Note that all the flux waveforms in Figures 8.8 to 8.10 are non-sinusoidal and that the flux in Figures 8.8 and 8.9 contain a dc bias component. This is problematic when using Bertotti's three term model since it's only applicable to sinusoidal flux waveforms. An approach similar to that in [60] was followed, which shows that the harmonic components in non-linear flux waveforms can be summed together to determine the total core losses. Therefore, a spectral analysis was performed to determine the harmonic components of the different flux flowing through the different core sections of the FSPM machine. These results are shown in Figures 8.11 to 8.14.

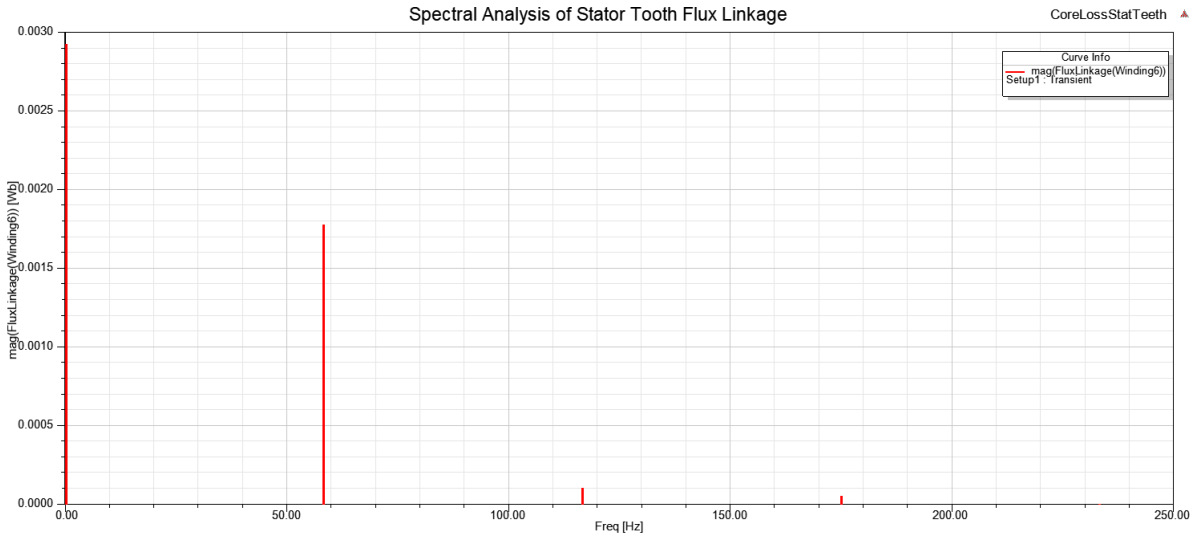

Figure 8.11: Spectral analysis of stator tooth flux

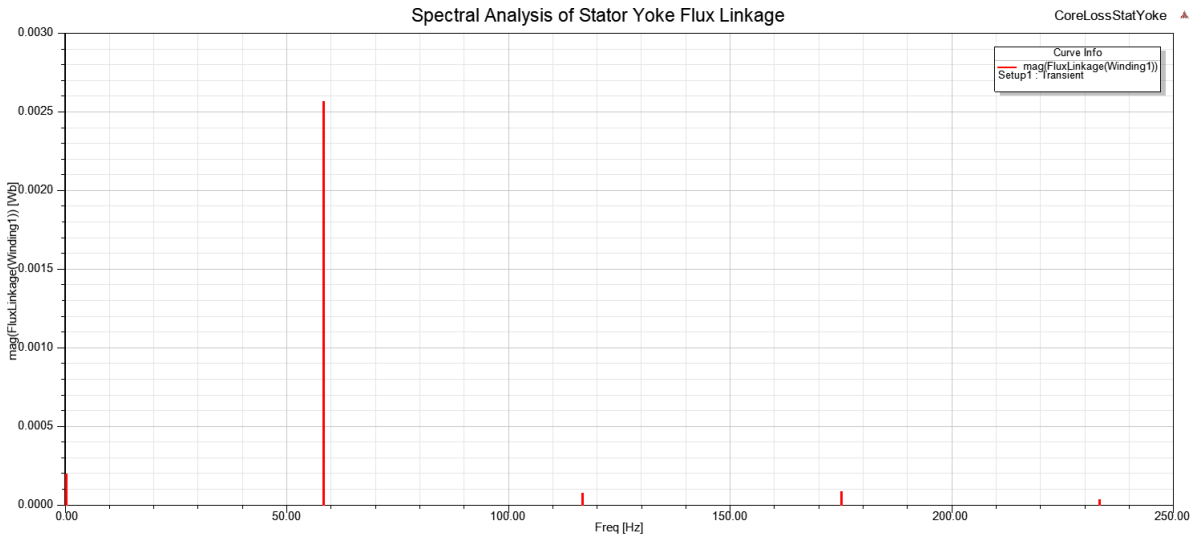

Figure 8.12: Spectral analysis of stator back-iron flux

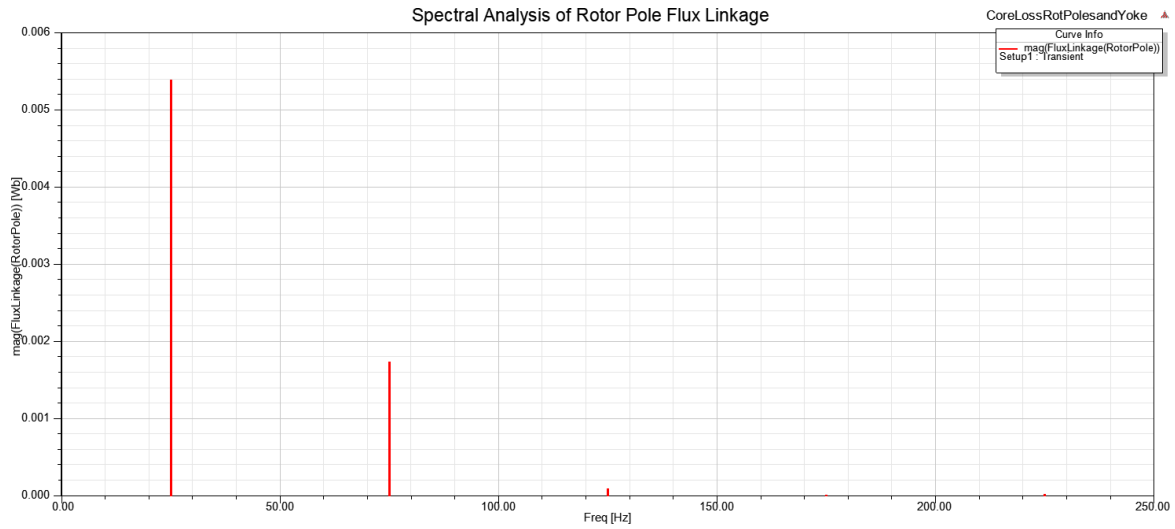

Figure 8.13: Spectral analysis of rotor pole flux

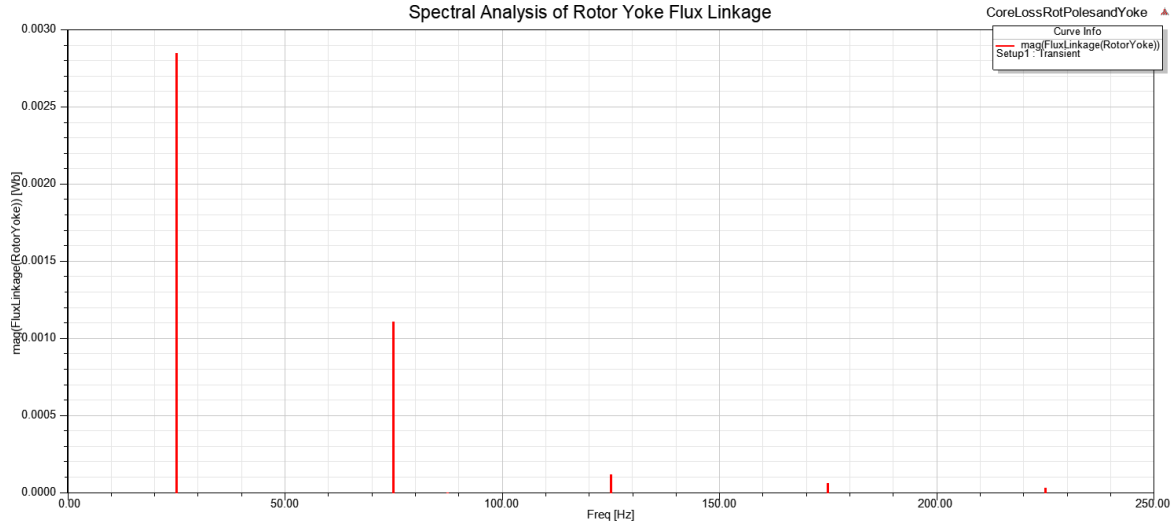

Figure 8.14: Spectral analysis of rotor back-iron flux

Seven frequencies are identified from Figures 8.11 to 8.14 and are summarized in Table 8.2. The core losses are derived using inter- and extrapolation of the data obtained in Table 8.1 and (8.4) by means of the script in Appendix A.3.

The resultant core losses for each on these identified frequencies are plotted in Figures 8.15 and 8.16. The dc bias component at 0 Hz can be neglected since it would account for 0 W based on (8.4).

Table 8.2: Frequencies in Different Magnetic Core Parts of an FSPM Machine

Zone	**Frequency (Hz)**	**Maximum Flux (mWb)**	**Cross Sectional Area (m^2)**	**Maximum Flux Density (T)**
Stator Tooth	0	2.918	2.40E-03	1.22
”	58.33	1.776	”	0.74
”	116.67	0.108	”	0.05
”	175	0.058	”	0.02
Stator	0	0.204	2.15E-03	0.10
Back-Iron	58.33	2.565	”	1.19
”	116.67	0.084	”	0.04
”	175	0.916	”	0.43
”	233.33	0.043	”	0.02
Rotor Pole	25	5.393	3.21E-03	1.68
”	75	1.743	”	0.54
”	125	0.103	”	0.03
Rotor	25	2.853	8.62E-03	0.33
Back-Iron	75	1.112	”	0.13
”	125	0.121	”	0.01

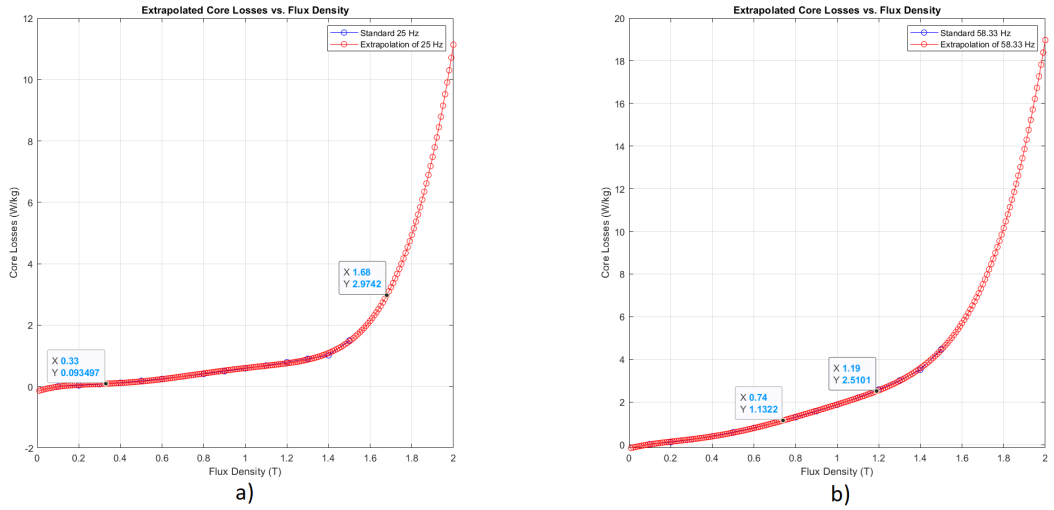

Figure 8.15: Derived core losses at a) 25 Hz and b) 58.33 Hz

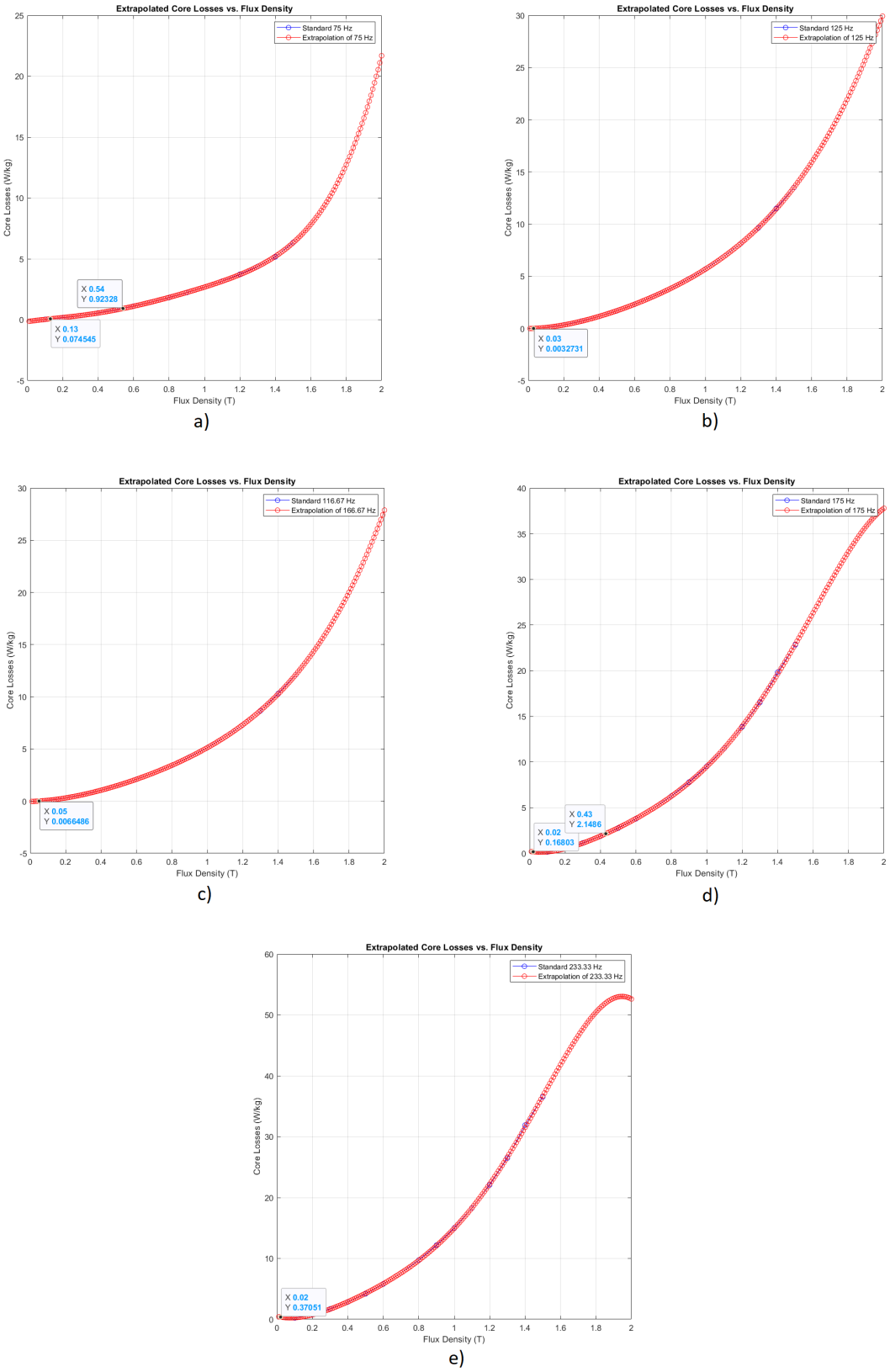

Figure 8.16: Derived core losses at a) 75 Hz b) 116.67 Hz c) 125 Hz d) 175 Hz and e) 233.33 Hz

Table 8.3: Individual Core Losses

Zone	**Freq (Hz)**	**Max Flux Density (T)**	**Core Losses - Analyt (W/kg)**	**Core Losses - ML (W/kg)**	**Mass (kg)**	**Core Loss - Analyt (W)**	**Core Loss - ML (W)**
Stator	58.33	0.74	1.132	0.89	19.42	21.99	17.23
Tooth	116.67	0.05	0.007	0	”	0.13	-0.07
”	175	0.02	0.168	0.16	”	3.26	3.09
Stator	58.33	1.19	2.510	2.05	5.75	14.43	11.81
Back-	116.67	0.04	0	0	”	0	-0.02
Iron	175	0.43	2.149	2.54	”	12.35	14.59
”	233.33	0.02	0.371	0.16	”	2.13	0.92
Rotor	25	1.68	2.974	4.76	3.46	10.28	16.49
Pole	75	0.54	0.923	0.52	”	3.19	1.81
”	125	0.03	0.003	0	”	0.01	-0.01
Rotor	25	0.33	0.093	0.23	15.51	1.45	3.54
Back-	75	0.13	0.075	0.03	”	1.16	0.40
Iron	125	0.01	0	0	”	0	-0.06

The results from Figures 8.15 and 8.16 are summarized in Table 8.3 and used to calculate the analytical core losses. In addition to this, a machine learning (ML) model was developed to compare with the analytical calculations. Using a machine learning model reduces the steps required to determine the core losses, since the only data you need are the original core loss curves from the manufacturer, the frequencies in the specific core sections of the FSPM machine, and the respective maximum flux densities.

Machine learning models require a lot of data points to learn the relationship between the input and output data, and since there are very few data points available from the manufacturer's core loss curves, a deep learning model was first developed in Appendix A.6 to predict more data points. These bigger datasets were then used with a random forest regressor in Appendix A.7 as the machine learning method to learn the relationship between frequency, flux density and core losses per kg. This method is able to mitigate an over-fitting problem that's often seen with a decision tree machine learning method, and a potential improvement would be to develop a deep learning model to perform the complete core loss prediction with higher accuracy [61].

The analytical core losses for the stator and rotor are 54.29 W and 16.09 W respectively, with a combined total of 70.38 W. The machine learning model was less accurate when predicting the individual stator and rotor core losses, however, the combined total came to 69.71 W, which is very close to the combined total from the analytical calculations. Figure 8.17 shows that the results correlate well with the numerical simulations.

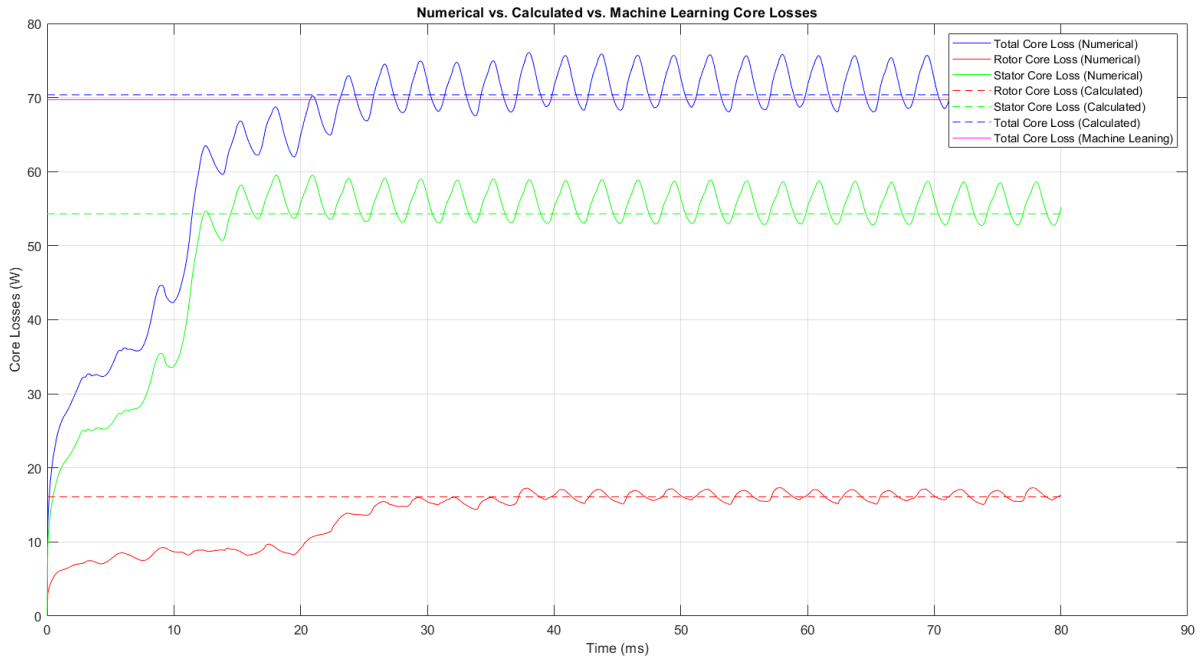

Figure 8.17: Numerical vs. calculated vs. machine learning core losses

There are a few possible reasons for the difference in analytical and numerical results. The first is that the core loss per kilogram depends a lot on the accuracy of the curve fitting, especially when extrapolating the curves above 1.5 T and below 0.1 T, as these values were not given by the manufacturer and tend to be less accurate. The second being that the stator dove tails haven't been taken into consideration in the analysis. Lastly, the distribution of the flux is non-uniform, especially in the stator teeth as it splits when entering and exiting the permanent magnets.

Chapter 9

Conclusion and Recommendations

The primary objectives to perform a design study and analysis of an FSPM machine was completed successfully. The numerical simulation results meet the design requirements when also taking into consideration mechanical design constraints for implementation. The secondary objectives on the parametric studies, optimization and core loss analysis were also completed to satisfaction. The need for parametric studies are clear as to reduce the computational time to find an optimized model that meet the design requirements. A detailed derivation of the sizing equation is also presented to assist designers in their understanding of the FSPM's development and think of new ways to potentially improve it. The desired results were limited to 2D FEA analyses, which reduces the accuracy as end-effects, axial leakage flux and complex cross-magnetization are not taken into consideration.

A deeper understanding and further research should be conducted into the complex cross-magnetization in the stator windings so that analytical approximations could be improved. This will allow for a more accurate computation of the effects that the full-load current has on the terminal voltage.

Bertotti's models assume that the flux waveforms are sinusoidal and even though that's not the case for FSPM machines, the approximations used in this dissertation were accurate. The main complication revolves around the extrapolation of the core loss data from the manufacturer and it is therefore recommended to conduct more research with artificial intelligence to determine a quicker and more accurate method for the core loss analysis.

Lastly, a suitable control system should be developed to perform and analyse the dynamic behaviour of the designed FSPM machine under vector control. This will ultimately be

the true test of the FSPM machine developed in this dissertation as it's designed to be operated in the dq reference frame with q-axis current control.

Overall, the project was a success and the implementation of the FSPM machine will be conducted in the future to validate the design.

Bibliography

[1] (2018). Vestas facts, Vestas, [Online]. Available: `https://www.vestas.com/#!`.

[2] M. R. R. Mojumdar, M. S. H. Himel, M. S. Rahman, and S. J. Hossain, "Electric machines and their comparative study for wind energy conversion systems (wecss)," *Journal of Clean Energy Technologies*, vol. 4, no. 4, pp. 290–294, 2016.

[3] C. Sikder, "Design and controller optimization of switched reluctance and flux switching pm machines," Doctor of Philosophy in Electrical Engineering, North Carolina State University, 2016.

[4] Y. Shi, L. Jian, J. Wei, Z. Shao, W. Li, and C. C. Chan, "A new perspective on the operating principle of flux-switching permanent-magnet machines," *IEEE Transactions on Industrial Electronics*, vol. 63, no. 3, pp. 1425–1437, 2016.

[5] F. Li, W. Hua, M. Tong, G. Zhao, and M. Cheng, "Nine-phase flux-switching permanent magnet brushless machine for low-speed and high-torque applications," *IEEE Transactions on Magnetics*, vol. 51, no. 3, 2015.

[6] Z. Q. Zhu and J. T. Chen, "Advanced flux-switching permanent magnet brushless machines," *IEEE Transactions on Magnetics*, vol. 46, no. 6, pp. 1447–1453, 2010.

[7] J. Zhang, M. Cheng, W. Hua, and X. Zhu, "New approach to power equation for comparison of doubly salient electrical machines," in *Conference Record of the 2006 IEEE Industry Applications Conference Forty-First IAS Annual Meeting*, Tampa, FL, USA: IEEE, 2006.

[8] J. T. Chen, Z. Q. Zhu, and D. Howe, "Stator and rotor pole combinations for multi-tooth flux-switching permanent-magnet brushless ac machines," *IEEE Transactions on Magnetics*, vol. 4, no. 12, pp. 4659–4667, 2008.

[9] G. Verez, G. Barakat, and Y. Amara, "Influence of slots and rotor poles combinations on noise and vibrations of magnetic origins in 'u'-core flux-switching permanent magnet machines," *Progress In Electromagnetics Research B*, vol. 61, no. 1, pp. 149–168, 2014.

[10] G. Verez, G. Barakat, Y. Amara, O. Bennouna, and G. Hoblos, "Impact of pole and slot combination on noise and vibrations of flux-switching pm machines," in *2014 International Conference on Electrical Machines (ICEM)*, Berlin, Germany: IEEE, 2014, pp. 182–188.

[11] J. T. Chen, Z. Q. Zhu, S. Iwasaki, and R. P. Deodhar, "Influence of slot opening on optimal stator and rotor pole combination and electromagnetic performance of switched-flux pm brushless ac machines," *IEEE Transactions on Industry Applications*, vol. 47, no. 4, pp. 1681–1691, 2011.

[12] J. T. Chen and Z. Q. Zhu, "Winding configurations and optimal stator and rotor pole combination of flux-switching pm brushless ac machines," *IEEE Transactions on Energy Conversion*, vol. 25, no. 2, pp. 293–302, 2010.

[13] M. Lehr and A. Binder, "Design and measurements of a permanent magnet flux-switching-machine for industrial applications," *Elektrotechnik and Informationstechnik*, vol. 134, no. 2, pp. 177–184, 2017.

[14] L. Shao, W. Hua, and M. Cheng, "Design of a twelve-phase flux-switching permanent magnet machine for wind power generation," in *17th International Conference on Electrical Machines and Systems (ICEMS)*, Hangzhou, China: IEEE, 2014, pp. 435–441.

[15] W. Hua and M. Cheng, "Cogging torque reduction of flux-switching permanent magnet machines without skewing," in *2008 International Conference on Electrical Machines and Systems*, Wuhan, China: IEEE, 2008, pp. 3020–3025.

[16] W. Xu, J. Zhu, Y. Zhang, and J. Hu, "Cogging torque reduction for radially laminated flux-switching permanent magnet machine with 12/14 poles," in *IECON 2011 - 37th Annual Conference of the IEEE Industrial Electronics Society*, Melbourne, VIC, Australia: IEEE, 2011, pp. 3590–3595.

[17] W. Hua, M. Cheng, Z. Q. Zhu, and D. Howe, "Design of flux-switching permanent magnet machine considering the limitation of inverter and flux-weakening capability," in *Conference Record of the 2006 IEEE Industry Applications Conference Forty-First IAS Annual Meeting*, Tampa, FL, USA: IEEE, 2006, pp. 2403–2410.

[18] W. Hua, Z. Q. Zhu, M. Cheng, Y. Pang, and D. Howe, "Comparison of flux-switching and doubly-salient permanent magnet brushless machines," in *2005 International Conference on Electrical Machines and Systems*, Nanjing, China: IEEE, 2005, pp. 165–170.

[19] A. S. Thomas, Z. Q. Zhu, and G. W. Jewell, "Proximity loss study in high speed flux-switching permanent magnet machine," *IEEE Transactions on Magnetics*, vol. 45, no. 10, pp. 4748–4751, 2009.

[20] Z. Q. Zhu, Y. Pang, J. T. Chen, R. L. Owen, D. Howe, S. Iwasaki, R. Deodhar, and A. Pride, "Analysis and reduction of magnet eddy current loss in flux-switching permanent magnet machines," in *4th IET Conference on Power Electronics, Machines and Drives*, York, UK: IET, 2008.

[21] Z. Q. Zhu, Y. Pang, J. T. Chen, Z. P. Xia, and D. Howe, "Influence of design parameters on output torque of flux-switching permanent magnet machines," in *2008 IEEE Vehicle Power and Propulsion Conference*, Harbin, China: IEEE, 2008.

[22] A. Chen, R. Nilssen, and A. Nysveen, "Analytical design of a high-torque flux-switching permanent magnet machine by a simplified lumped parameter magnetic circuit model," in *The XIX International Conference on Electrical Machines - ICEM 2010*, Rome, Italy: IEEE, 2010.

[23] C. Wen, G. Lu, P. Wang, Z. Li, X. Liu, and Z. Fan, "Vector control strategy for small-scale grid-connected pmsg wind turbine converter," in *2nd IEEE PES International Conference and Exhibition on Innovative Smart Grid Technologies*, Manchester, UK: IEEE, 2011.

[24] F. Kendouli, K. Abed, K. Nabti, H. Benalla, and B. Azoui, "High performance pwm converter control based pmsg for variable speed wind turbine," in *First International Conference on Renewable Energies and Vehicular Technology*, Hammamet, Tunisia: IEEE, 2012.

[25] H. Li, G. Lian, B. Chen, and G. Gu, "Vector control for flux-switching permanent magnet machine based on svpwm," in *2017 20th International Conference on Electrical Machines and Systems (ICEMS)*, Sydney, NSW, Australia: IEEE, 2017.

[26] M. Bhardwaj. (2013). Sensored field oriented control of 3-phase permanent magnet synchronous motors, Texas Instruments, [Online]. Available: `http://www.ti.com/lit/an/sprabq2/sprabq2.pdf`.

[27] U. B. Akuru and M. J. Kamper, "Evaluation of flux switching pm machines for medium-speed wind generator drives," in *2015 IEEE Energy Conversion Congress and Exposition (ECCE)*, Montreal, QC, Canada: IEEE, 2015, pp. 1925–1931.

[28] C. Sikder, I. Husain, and W. Ouyang, "Cogging torque reduction in flux-switching permanent-magnet machines by rotor pole shaping," *IEEE Transactions on Industry Applications*, vol. 51, no. 5, pp. 3609–3619, 2015.

[29] U. B. Akuru and M. J. Kamper, "Comparative advantage of flux switching pm machines for medium-speed wind drives," in *2015 International Conference on the Domestic Use of Energy (DUE)*, Cape Town, South Africa: IEEE, 2015.

[30] N. Rotevatn, "Design and testing of flux switched permanent magnet (fspm) machines," Master of Science in Energy and Environment, Norwegian University of Science and Technology, 2009.

[31] U. B. Akuru, "Design optimisation and performance evaluation of flux switching machines for geared medium–speed wind generator drives," Doctor of Philosophy in Electrical Engineering, Stellenbosch University, 2017.

[32] U. B. Akuru and M. J. Kamper, "Formulation and multiobjective design optimization of wound-field flux switching machines for wind energy drives," *IEEE Transactions on Industrial Electronics*, vol. 65, no. 2, pp. 1828–1836, 2018.

[33] U. B. Akuru and M. J. Kamper, "Performance comparison of optimum wound-field and ferrite pm flux switching machines for wind energy applications," in *2016 XXII International Conference on Electrical Machines (ICEM)*, Lausanne, Switzerland: IEEE, 2016, pp. 2478–2485.

[34] Z. Q. Zhu, Y. Pang, D. Howe, S. Iwasaki, R. Deodhar, and A. Pride, "Analysis of electromagnetic performance of flux-switching permanent-magnet machines by nonlinear adaptive lumped parameter magnetic circuit model," *IEEE Transactions on Magnetics*, vol. 41, no. 11, pp. 4277–4287, 2005.

[35] J. Zhao, Y. Zheng, C. Zhu, X. Liu, and B. Li, "A novel modular-stator outer-rotor flux-switching permanent-magnet motor," *Energies*, vol. 10, no. 7, p. 937, 2017.

[36] M. Ng'onga, "Design, analysis and prototyping of a high speed surface mounted permanent magnet machine," Master of Science in Engineering in Electrical Engineering, University of Cape Town, 2018.

[37] U. B. Akuru and M. J. Kamper, "Intriguing behavioral characteristics of rare-earth-free flux switching wind generators at small- and large-scale power levels," *IEEE Transactions on Industry Applications*, vol. 54, no. 6, pp. 5772–5782, 2018.

[38] Y. Li, S. Li, Y. Yang, and B. Sarlioglu, "Analysis of flux switching permanent magnet machine design for high-speed applications," in *2014 IEEE Energy Conversion Congress and Exposition (ECCE)*, Pittsburgh, PA, USA: IEEE, 2014, pp. 302–309.

[39] A. Zohoori, A. Vahedi, and M. A. Noroozi, "Design study of fspm generator with novel outer rotor configuration for small wind turbine application," in *2014 14th International Conference on Environment and Electrical Engineering*, Krakow, Poland: IEEE, 2014.

[40] E. Hoang, M. Lecrivain, and M. Gabsi, "A new structure of a switching flux synchronous polyphased machine with hybrid excitation," in *2007 European Conference on Power Electronics and Applications*, Aalborg, Denmark: IEEE, 2007.

[41] R. L. Boylestad, *Introductory Circuit Analysis*, 10th ed. Prentice Hall PTR Upper Saddle River, NJ, USA: Pearson, 2002, ch. 11: Magnetic Circuits, pp. 435–472, ISBN: 013097417X.

[42] R. L. Owen, Z. Q. Zhu, and G. W. Jewell, "Hybrid-excited flux-switching permanent magnet machines with iron flux bridges," *IEEE Transactions on Magnetics*, vol. 46, no. 6, pp. 1726–1729, 2010.

[43] A. K. Sawhney, *A Course in Electrical Machine Design*, 6th ed. Nai Sarak, Delhi: Dhanpat Rai Publishing Co Pvt Ltd, 2013, ch. 6: General Concepts and Constraints in Design of Rotating Machines, pp. 6.1–6.8.

[44] X. Xue, W. Zhao, J. Zhu, G. Liu, X. Zhu, and M. Cheng, "Design of five-phase modular flux-switching permanent-magnet machines for high reliability applications," *IEEE Transactions on Magnetics*, vol. 49, no. 7, pp. 3941–3944, 2013.

[45] X. Zhu, W. Hua, Z. Wu, W. Huang, H. Zhang, and M. Cheng, "Analytical approach for cogging torque reduction in flux-switching permanent magnet machines based on magnetomotive force-permeance model," *IEEE Transactions on Industrial Electronics*, vol. 65, no. 3, pp. 1965–1979, 2018.

[46] M. Shen, J. Wu, C. Gan, Y. Hu, and W. Cao, "Cogging torque reduction in fspm machines with short magnets and stator lamination bridge structure," in *IECON 2016 - 42nd Annual Conference of the IEEE Industrial Electronics Society*, Florence, Italy: IEEE, 2016, pp. 4307–4312.

[47] D. Wang, X. Wang, and S.-Y. Jung, "Reduction on cogging torque in flux-switching permanent magnet machine by teeth notching schemes," *IEEE Transactions on Magnetics*, vol. 48, no. 11, pp. 4228–4231, 2012.

[48] C. Studer, A. Keyhani, T. Sebastian, and S. . Murthy, "Study of cogging torque in permanent magnet machines," in *IAS '97. Conference Record of the 1997 IEEE Industry Applications Conference Thirty-Second IAS Annual Meeting*, New Orleans, LA, USA: IEEE, 1997, pp. 42–49.

[49] L. Zhu, S. Z. Jiang, Z. Q. Zhu, and C. C. Chan, "Analytical methods for minimizing cogging torque in permanent-magnet machines," *IEEE Transactions on Magnetics*, vol. 45, no. 4, pp. 2023–2031, 2009.

[50] M. J. Jin, Y. Wang, J. X. Shen, P. C. K. Luk, W. Z. Fei, and C. F. Wang, "Cogging torque suppression in a permanent-magnet flux-switching integrated-starter-generator," *IET Electric Power Applications*, vol. 4, no. 8, pp. 647–656, 2010.

[51] S. E. Abdollahi and S. Vaez-Zadeh, "Reducing cogging torque in flux switching motors with segmented rotor," *IEEE Transactions on Magnetics*, vol. 49, no. 10, pp. 5304–5309, 2013.

[52] L. Dosiek and P. Pillay, "Cogging torque reduction in permanent magnet machines," *IEEE Transactions on Magnetics Industry Applications*, vol. 43, no. 6, pp. 1565–1571, 2007.

[53] N. Bianchi and S. Bolognani, "Design techniques for reducing the cogging torque in surface-mounted pm motors," *IEEE Transactions on Industry Applications*, vol. 38, no. 5, pp. 1259–1265, 2002.

[54] H. Jia, M. Cheng, W. Hua, Z. Yang, and Y. Zhang, "Compensation of cogging torque for flux-switching permanent magnet motor based on current harmonics injection," in *2009 IEEE International Electric Machines and Drives Conference*, Miami, FL, USA: IEEE, 2009, pp. 286–291.

[55] (2018). Maxwell help. version 19.1, Ansys Inc., [Online]. Available: `https://ansyshelp.ansys.com/account/secured?returnurl=/Views/Secured/Electronics/v191/home.htm%23../Subsystems/Maxwell/Content/Maxwell_PDFs.htm`.

[56] M. Kalyan, "Comparison of interior permanent magnet synchronous machines for a high-speed application," Master of Science in Engineering in Electrical Engineering, University of Cape Town, 2018.

[57] Y. Chen and P. Pillay, "An improved formula for lamination core loss calculations in machines operating with high frequency and high flux density excitation," in *Industry Applications Society Annual Meeting (IAS), Conference Record of the IEEE*, Pittsburgh, USA: IEEE, 2002.

[58] A. K. Sawhney, *A Course in Electrical Machine Design*, 6th ed. Nai Sarak, Delhi: Dhanpat Rai Publishing Co Pvt Ltd, 2013, ch. 3: Principles of Magnetic Circuit Design, pp. 3.1–3.80.

[59] M. Torrent, P. Andrada, B. Blanqué, E. Martinez, J. I. Perat, and J. A. Sanchez, "Method for estimating core losses in switched reluctance motors," *European Transactions on Electrical Power*, vol. 21, no. 1, pp. 757–771, 2011.

[60] S. Nalakath, M. Preindl, Y. Yang, B. Bilgin, B. Cheng, and A. Emadi, "Modeling and analysis of core losses of an ipm machine for online estimation purposes," in *IECON*, Yokohama, Japan: IEEE, 2015.

[61] (2020). Random forest regression: When does it fail and why? Neptune Labs Inc., [Online]. Available: `https://neptune.ai/blog/random-forest-regression-when-does-it-fail-and-why`.

Appendices

Appendix A - Scripts

Appendix A.1 - FSPM Stator Outer Diameter vs. Stack Length

```
a = 0:0.001:0.5;
Dso = a; %stator outer diameter [m]
Ksio = 0.6; %stator split ratio
Lst = a; %stack length [m]
Bg = 2; %airgap flux density (measured from FEA, use 1.8T as initial design value) [T]
Js = 5; %current density (ranges from 3 - 7) [A/mm2]
Ns = 12; %number of stator poles
Nr = 10; %number of rotor poles
n = 250; %base speed [rpm]
g = 0.001; %airgap length [m]
m = 3; %number of phases
Cs = 0.25; %stator pole arc length vs stator pole pitch
Kd = 0.7; %flux leakage factor
p = 1.72*10^(-8); %resistivity of copper
u = 4*pi()*10^(-7); %permeability of free space
epsilon = 0.9; %ratio of back-EMF to full-load terminal voltage
kh = 0.0452736613347347;
ke = 0.000101277195748641;
f = Nr*n/60;
Dsi = Ksio*Dso; %stator inner diameter
Rso = Dso/2;
Rsi = Dsi/2;
Dro = Dsi-(2*g); %rotor outer diameter
TauS = (pi*Dsi)/Ns; %stator pole/slot pitch
```

```
TauR = (pi*Dro)/Nr; %rotor pole/slot pitch
Theta = 360/Ns; %angle between stator poles
Theta1 = 90/Ns; %
Theta2 = 3/2*Theta1; %
H = TauS*Cs; %initial dimensions for stator and rotor tooth width, PM length and
stator slot width
Bsl = H;
Hpm = H;
Br = H;
Hs = (Dso/2)-(Dsi/2)-H; %slot height
WidthPM = 2*(Dsi/2)*sin((Theta1/2)*pi/180); %actual width of PM and stator teeth
Dri = Dro-(2*H); %rotor inner diameter
Dryoke = Dro-(2*H)-(2*H); %rotor yoke diameter
EmbraceR = H./TauR; %rotor embrace
EmbraceS = ((H.*3)./TauS); %stator embrace for FSPM (reason for *3)
A1 = (pi().*Rso.^2)-(pi().*(Rso-H).^2);
A2 = 3.*H.*Hs;
Astator = A1+(Ns.*A2)
Aslot = (((pi().*Rso.^2)-(pi().*Rsi.^2))-Astator)./Ns;
Se = 1/4.*TauS.*Lst;
Kcu = 0.4; %slot fill factor
As = Js*10^6*Kcu*Ns.*Aslot./(pi().*Dsi); %specific electric loading for given current
density [A/m]
Dac = 0.001626; %copper conductor diameter [m] SWG
Ac = pi()*(Dac/2)^2; %[m2]
Nt = Kcu*Ns.*Aslot./(2*Ac*m); %number of turns per phase
w1 = ceil(Nt/(Ns/m));
Nt = Ns/m*w1;
I = sqrt(2)*pi().*As.*Dsi./(2.*m.*Nt); %full-load current[A]
Irms = I./sqrt(2) %full-load current in rms [A]
E = Nt.*Kd.*Bg.*Bsl.*Lst.*pi().*n.*Nr./30; %no-load peak back-EMF [V]
Erms = E./sqrt(2) %no-load back-EMF in rms [V]
rc = 2.*p.*Nt.*Lst./Ac; %conductor resistance excl end part per phase
Ploss = m.*(Irms.^2).*rc; %total winding losses
XL =
((pi().^2).*Nr.*n.*u.*(Nt.^2).*Lst.*Dsi.*Cs)./(30.*(Lst+((3.*pi().*Dsi.*Cs)./Ns)).*Ns);
pf = 0.88;
```

```
Ploss = (kh.*f.*Bg.^(2))+(ke.*f.^(2).*Bg.^(2))+(3*rc.*Irms.^2)
Pout1 = 3.*Vt.*Irms.*pf
eff = Pout1./(Pout1+Ploss).*100
%Output Power
[X, Y] = meshgrid(a);
[W] = meshgrid(Nt);
[BSL] = meshgrid(Bsl);
[DSI] = meshgrid(Dsi);
[AS] = meshgrid(As);
E1 = W.*Kd.*Bg.*BSL.*Y.*pi().*n.*Nr./(sqrt(2)*30); %no-load rms back-EMF [V]
IRMS = pi().*AS.*DSI./(2.*m.*W);
VT = E1./epsilon;
Z = 3.*VT.*IRMS.*pf
figure
contour(X,Y,Z,20,'b','ShowText','on','LevelList',[1000:1000:10000])
hold on
% Full-Load Terminal Voltage
[X, Y] = meshgrid(a);
[W] = meshgrid(Nt);
[BSL] = meshgrid(Bsl);
E1 = W.*Kd.*Bg.*BSL.*Y.*pi().*n.*Nr./(sqrt(2)*30); %no-load peak back-EMF [V]
VT = E1./epsilon;
contour(X,Y,VT,'g','LevelList',[220:220])
hold on
% Aspect Ratio
[X, Y] = meshgrid(a);
[LE] = meshgrid(Lst);
[DSI] = meshgrid(Dsi);
KL = Y./DSI; %aspect ratio
contour(X,Y,KL,'r','ShowText','on','LevelList',[2:2])
hold on
% Specific Electric Loading
[X, Y] = meshgrid(a);
[ASLOT] = meshgrid(Aslot);
[DSI] = meshgrid(Dsi);
AS1 = Js*10^6*Kcu*Ns.*ASLOT./(pi().*DSI); %specific electric loading for given
current density [A/m]
```

```
contour(X,Y,AS1,'m','ShowText','on','LevelList',[20000:10000:50000])
xlabel('Stator Outer Diameter (m)')
ylabel('Stack Length (m)')
zlabel('Back EMF (V)')
title(['Power Output, Full-load Terminal Voltage, Aspect Ratio and Specific Electric
Loading vs. Stator Outer Diameter and Stack Length'])
grid on
legend('Power Output (W)','Full-load Terminal Voltage (220 Vrms)','Aspect
Ratio','Specific Electric Loading (A/m)')
```

Appendix A.2 - FSPM Geometrical Parameters

```
Dso = 0.238; %stator outer diameter [m]
Ksio = 0.6; %stator split ratio
Lst = 0.286; %stack length [m]
Bg = 2.2422; %airgap flux density (measured from FEA, use 1.8T as initial design value) [T]
Js = 5; %current density (ranges from 3 - 7) [A/mm2]
Ns = 12; %number of stator poles
Nr = 10; %number of rotor poles
n = 250; %base speed [rpm]
g = 0.001; %airgap length [m]
m = 3; %number of phases
Cs = 0.25; %stator pole arc length vs stator pole pitch
Kd = 0.697; %flux leakage factor
p = 1.72*10^(-8); %resistivity of copper
u = 4*pi()*10^(-7); %permeability of free space
kh = 0.0452736613347347;
ke = 0.000101277195748641;
epsilon = 0.899;
f = Nr*n/60;
Dsi = Ksio*Dso; %stator inner diameter
Rso = Dso/2;
Rsi = Dsi/2;
Kl = Lst/Dsi; %aspect ratio
Dro = Dsi-(2*g); %rotor outer diameter
TauS = (pi*Dsi)/Ns; %stator pole/slot pitch
TauR = (pi*Dro)/Nr; %rotor pole/slot pitch
Theta = 360/Ns; %angle between stator poles
Theta1 = 90/Ns; %
Theta2 = 3/2*Theta1; %
H = TauS*Cs; %initial dimensions for stator and rotor tooth width, PM length and stator slot width
Bsl = H;
Hpm = H;
Br = H;
Hs = (Dso/2)-(Dsi/2)-H; %slot height
```

```
WidthPM = 2*(Dsi/2)*sin((Theta1/2)*pi/180); %actual width of PM and stator teeth
Hph = Dro/4;
Dri = 3/4*(Dro-2*(H)); %rotor inner diameter
Dryoke = Dro-(2*H)-(2*H); %rotor yoke diameter
Dg = Dsi-g;
EmbraceR = H/TauR; %rotor embrace
EmbraceS = ((H*3)/TauS); %stator embrace for FSPM (reason for *3)
A1 = (pi()*Rso^2)-(pi()*(Rso-H)^2);
A2 = 3*H*Hs;
Astator = A1+(Ns*A2);
Aslot = (((pi()*Rso^2)-(pi()*Rsi^2))-Astator)/Ns;
Se = 1/4*TauS*Lst;
Dac = 0.001626; %copper conductor diameter [m] SWG
a = pi()*(Dac/2)^2; %copper conductor area[m2]
Kcu = 0.4; %slot fill factor
Nt = Kcu*Ns*Aslot/(2*a*m); %number of turns per phase
w1 = ceil(Nt/(Ns/m));
Nt = Ns/m*w1;
Acopper = a*Nt/(Ns/m);
As = Js*10^6*Kcu*Ns*Aslot/(pi()*Dg); %specific electric loading for given current
density [A/m]
I = sqrt(2)*pi()*As*Dg/(2*m*Nt); %full-load current[A]
Irms = I/sqrt(2) %full-load current in rms [A]
E = Nt*Kd*Bg*Bsl*Lst*pi()*n*Nr/30; %no-load peak phase back-EMF [V]
Erms = E/sqrt(2) %no-load phase back-EMF in rms [V]
Vt = Erms/epsilon; %terminal voltage
rc = 2*p*Nt*Lst/a; %conductor resistance excl end part per phase
pf = cos((90.29-60.03)*pi()/180);
Ploss = (kh*f*Bg^(2))+(ke*f^(2)*Bg^(2))+(3*rc*Irms^2)
Pout1 = 3*Vt*Irms*pf
eff = Pout1/(Pout1+Ploss)*100
```

Appendix A.3 - Core Loss Curve Fitting

```
x = [0.1 0.2 0.3 0.4 0.5 0.6 0.7 0.8 0.9 1 1.1 1.2 1.3 1.4 1.5];
% y = [0.02665349 0.113042548 0.240787065 0.395860725 0.58181664 0.786181316
1.024348384 1.277716609 1.562647907 1.868656985 2.206630162 2.589502873
3.013074559 3.510378734 4.472569536]; %f = 58.33
% y = [0.007405533 0.034832271 0.076142171 0.125868792 0.186803783 0.250877718
0.329394042 0.409890611 0.498874292 0.590837763 0.688398319 0.795948193 0.90692365
1.013761799 1.504831737]; %f = 25
% y = [3.90E-02 1.61E-01 3.42E-01 5.61E-01 8.24E-01 1.12E+00 1.45E+00 1.82E+00
2.23E+00 2.68E+00 3.17E+00 3.74E+00 4.38E+00 5.16E+00 6.34E+00]; %f = 75
% y = [8.47E-02 3.36E-01 7.03E-01 1.15E+00 1.69E+00 2.31E+00 3.02E+00 3.80E+00
4.69E+00 5.69E+00 6.83E+00 8.14E+00 9.64E+00 1.15E+01 1.35E+01]; %f = 125
% y = [0.076290022 0.303895569 0.637139406 1.046739087 1.534911001 2.092170113
2.728716387 3.43141987 4.236564961 5.130107772 6.145350403 7.313696464 8.65000621
10.30608355 12.12931054]; %f = 116.67
% y = [0.141410173 0.547071762 1.139128649 1.874269831 2.752646556 3.778068002
4.948523419 6.270847586 7.804364947 9.537375243 11.53316075 13.84417148
16.51568846 19.83427825 22.83086877]; %f= 175
y = [0.219351241 0.833528291 1.729046649 2.850666606 4.197230387 5.794307299
7.625500059 9.728683974 12.18918861 15.00319246 18.27011347 22.06497729
26.47060357 31.89946099 36.52885766]; %f = 233.33
n=5;
p = polyfit(x,y,n);
x2 = 0.01:.01:2;
y2 = polyval(p,x2);
plot(x,y,'b-o',x2,y2,'r-o')
grid on
s = sprintf('y = (%.1f) x^2 + (%.1f) x',p(1),p(2));
text(2,400,s)
title('Extrapolated Core Losses vs. Flux Density')
xlabel('Flux Density (T)')
ylabel('Core Losses (W/kg)')
% legend('Standard 58.33 Hz','Extrapolation of 58.33 Hz') % for 58.33Hz
% legend('Standard 25 Hz','Extrapolation of 25 Hz') % for 25 Hz
% legend('Standard 75 Hz','Extrapolation of 75 Hz') % for 75 Hz
% legend('Standard 125 Hz','Extrapolation of 125 Hz') % for 125 Hz
```

% legend('Standard 116.67 Hz','Extrapolation of 166.67 Hz') % for 116.67 Hz
% legend('Standard 175 Hz','Extrapolation of 175 Hz') % for 175 Hz
legend('Standard 233.33 Hz','Extrapolation of 233.33 Hz') % for 233.33 Hz

Appendix A.4 - Core Loss Curve Fitting for Flux Densities

```
% x = [7.071067812 10 14.14213562 20 31.6227766 50]; %B < 1.5
x = [7.071067812 10 14.14213562 20 31.6227766]; %B = 1.5
% y = [0.0004 0.0007 0.0008 0.0012 0.00212 0.003456]; %B = 0.1
% y = [0.0018 0.0026 0.0032 0.0045 0.00749 0.01204]; %B = 0.2
% y = [0.0038 0.0054 0.00675 0.009425 0.0153 0.02508]; %B = 0.3
% y = [0.0062 0.0088 0.01125 0.015725 0.0257 0.0436]; %B = 0.4
% y = [0.0092 0.0127 0.01665 0.023425 0.039 0.0688]; %B = 0.5
% y = [0.0124 0.0173 0.0229 0.03275 0.0561 0.1024]; %B = 0.6
% y = [0.0162 0.0224 0.03015 0.04375 0.0771 0.1468]; %B = 0.7
% y = [0.0202 0.028 0.0384 0.05675 0.1031 0.2036]; %B = 0.8
% y = [0.0248 0.0344 0.0479 0.072 0.135 0.274]; %B = 0.9
% y = [0.0298 0.0415 0.0585 0.08975 0.1733 0.3596]; %B = 1.0
% y = [0.0352 0.0495 0.071 0.1105 0.2188 0.462]; %B = 1.1
% y = [0.0418 0.0585 0.085 0.1345 0.2724 0.5812]; %B = 1.2
% y = [0.0492 0.0688 0.101 0.16225 0.3346 0.7172]; %B = 1.3
% y = [0.0592 0.0818 0.119 0.1935 0.4056 0.852]; %B = 1.4
y = [0.0714 0.0982 0.1415 0.22925 0.4884]; %B = 1.5
n = 2;
p = polyfit(x,y,n);
x2 = 1:.1:50;
y2 = polyval(p,x2);
plot(x,y,'o',x2,y2)
grid on
s = sprintf('y = (%.1f) x^2 + (%.1f) x + (%.1f)',p(1),p(2),p(3));
text(2,400,s)
```

Appendix A.5 - Magnetic Circuit Modelling

```
syms Fpm Rpm Rgol Rgil Rsb Rst Rrt Rrb Rg11 Rg21 Rg22 Rg32 Rg42 Rg43 Rg53
Rg64
Le = 0.204;
U0 = 4*pi()*10^(-7);
Br = 1.2;
Upm = 1.1;
Hst = 0.0094; %stator tooth width
Hrt = 0.12; %rotor pole width
Hpm = 0.005958; %pm thickness
Wpm = 0.041658; %pm width
Fpm = Br*Hpm/(Upm*U0);
Rpm = Hpm/(Upm*U0*Wpm*Le);
Rst = 7;
Rsb = 3;
Rgol = 5;
Rgil = 2;
Rrt = 5;
Rrb = 3;
Rg11 = 7;
Rg21 = 2.5;
Rg22 = 4;
Rg32 = 6;
Rg42 = 7;
Rg43 = 9;
Rg53 = 5;
Rg64 = 2;
F = [0;Fpm;Fpm;0;0;0;0;Fpm;Fpm;0;0;0;0;Fpm;Fpm;0];
A = [-Rpm-Rgol Rpm 0 0 0 0 0 0 0 0 0 0 0 0 0 0;-Rpm Rpm 0 0 0 0 0 0 0 0 0 0 0 0 0 0;
0 0 -2*Rst-Rgil Rgil 0 Rst 0 0 0 0 0 0 0 0 0 0; 0 0 Rgil -Rg11-Rgil-Rg21 Rg21 0 0 0 0 0 0
0 0 0 0 0; 0 0 0 Rg21 -2*Rrt-Rg21-Rg22-Rrb Rg22 0 0 0 0 Rrt 0 0 0 0 0; 0 0 Rst 0 Rg22
-Rsb-2*Rst-Rg32-Rg22 0 0 Rst Rg32 0 0 0 0 0 0; 0 0 0 0 0 0 -Rpm-Rgol Rpm 0 0 0 0 0 0
0 0; 0 0 0 0 0 0 Rpm -Rpm 0 0 0 0 0 0 0 0; 0 0 0 0 0 -Rst 0 0 2*Rst+Rgil -Rgil 0 -Rst 0
0 0 0; 0 0 0 0 0 Rg32 0 0 Rgil -Rg32-Rgil-Rg42 Rg42 0 0 0 0 0; 0 0 0 0 Rrt 0 0 0 0 Rg42
-2*Rrt-Rrb-Rg42-Rg43 Rg43 0 0 0 Rrt; 0 0 0 0 0 0 0 0 Rst 0 Rg43
-Rsb-Rg43-2*Rst-Rg53 0 0 Rst Rg53; 0 0 0 0 0 0 0 0 0 0 0 0 -Rpm-Rgol Rpm 0 0; 0 0 0
```

```
0 0 0 0 0 0 0 0 0 -Rpm Rpm 0 0; 0 0 0 0 0 0 0 0 0 0 0 0 Rst 0 0 -2*Rst-Rgil Rgil; 0 0 0 0 0
0 0 0 0 0 0 Rrt Rg53 0 0 Rgil -2*Rrt-Rrb-Rg53-Rg64-Rgil];
B = A;
prompt = 'Which flux would you like to calculate, 1 to 16? ';
x = input(prompt);
if x == 1
A(:,1) = F;
I1 = det(A)/det(B)
elseif x == 2
A(:,2) = F;
I2 = det(A)/det(B)
elseif x == 3
A(:,3) = F;
I3 = det(A)/det(B)
elseif x == 4
A(:,4) = F;
I4 = det(A)/det(B)
elseif x == 5
A(:,5) = F;
I5 = det(A)/det(B)
elseif x == 6
A(:,6) = F;
I6 = det(A)/det(B)
elseif x == 7
A(:,7) = F;
I7 = det(A)/det(B)
elseif x == 8
A(:,8) = F;
I8 = det(A)/det(B)
elseif x == 9
A(:,9) = F;
I9 = det(A)/det(B)
elseif x == 10
A(:,10) = F;
I10 = det(A)/det(B)
elseif x == 11
A(:,11) = F;
```

```
I11 = det(A)/det(B)
elseif x == 12
A(:,12) = F;
I12 = det(A)/det(B)
elseif x == 13
A(:,13) = F;
I13 = det(A)/det(B)
elseif x == 14
A(:,14) = F;
I14 = det(A)/det(B)
elseif x == 15
A(:,15) = F;
I15 = det(A)/det(B)
elseif x == 16
A(:,16) = F;
I16 = det(A)/det(B)
end
```

Appendix A.6 - Deep Learning for Core Losses

```
# This model was scripted in the Python Programming Language
import tensorflow as tf
import matplotlib.pyplot as plt
import numpy as np
import logging
import keras
logger = tf.get_logger()
logger.setLevel(logging.ERROR)
# Input and Output Data
fluxdensity = np.array([0.1, 0.2, 0.3, 0.4, 0.5, 0.6, 0.7, 0.8, 0.9, 1.0, 1.1, 1.2, 1.3, 1.4, 1.5,
1.6, 1.7, 1.8], dtype=float)
powerloss = np.array( [0.02, 0.09, 0.19, 0.31, 0.46, 0.62, 0.81, 1.01, 1.24, 1.49, 1.76, 2.09,
2.46, 2.96, 3.57, 4.38, 5.02, 5.47], dtype=float)
# Layer and Number of Neurons
l0 = tf.keras.layers.Dense(units=30, activation='relu', input_shape=[1])
# l1 = tf.keras.layers.Dense(units=64, activation= 'relu')
# l2 = tf.keras.layers.Dense(units=64, activation= 'relu')
# l3 = tf.keras.layers.Dense(units=64, activation= 'relu')
l4 = tf.keras.layers.Dense(units=1)
# Defining the neural network
model = tf.keras.Sequential([l0, l4])
# Compiling the data
model.compile(loss='mean_squared_error',
optimizer=tf.keras.optimizers.RMSprop(0.001),
metrics=['mean_absolute_percentage_error', 'mse'])
# Training the neural network
epoch_update = 1
index = epoch_update - 1
history = model.fit(fluxdensity, powerloss, epochs=epoch_update, verbose=False)
loss = history.history['loss']
loss = float(loss[index])
losstest = loss
index1 = [loss]
# print(loss)
indexing = 3
```

```
loss_desired = float(0)
while losstest > loss_desired:
index += 1
epoch_update += 1
history = model.fit(fluxdensity, powerloss, epochs=epoch_update, verbose=False)
loss = history.history['loss']
losses = float(loss[index])
print(losses)
index1.extend([losses])
plt.xlabel('Epoch Number')
plt.ylabel("Loss Magnitude")
plt.title("Losses vs. Epoch Value")
# plt.plot(history.history['loss'])
plt.plot(index1)
plt.pause(0.05)
plt.draw()
indexing += 1
losstest = losses
# moving average calculator
limit = 0.0001
if len(loss) >= 5:
x = (loss[-1]) + (loss[-2]) + (loss[-3]) + (loss[-4]) + (loss[-5])
average = x / 5
upperlimit = average * (1 + limit)
lowerlimit = average * (1 - limit)
print(average, upperlimit, lowerlimit)
if upperlimit > loss[-1] > lowerlimit:
break
print("Saturated... Best possible solution found")
plt.show()
model.summary()
# Plotting the graphs
plt.xlabel('Epoch Number')
plt.ylabel("Loss Magnitude")
plt.plot(history.history['loss'])
plt.show()
plt.xlabel('Epoch Number')
```

```
plt.ylabel("Magnitude of Average Error
(plt.plot(history.history['mean_absolute_percentage_error'])
plt.show()
# Predicting the output based on the specified input
output = model.predict([0, 0.01, 0.02, 0.03, 0.04, 0.05, 0.06, 0.07, 0.08, 0.09, 0.1, 0.11,
0.12, 0.13, 0.14, 0.15, 0.16, 0.17, 0.18, 0.19, 0.2, 0.21, 0.22, 0.23, 0.24, 0.25, 0.26, 0.27,
0.28, 0.29, 0.3, 0.31, 0.32, 0.33, 0.34, 0.35, 0.36, 0.37, 0.38, 0.39, 0.4, 0.41, 0.42, 0.43,
0.44, 0.45, 0.46, 0.47, 0.48, 0.49, 0.5, 0.51, 0.52, 0.53, 0.54, 0.55, 0.56, 0.57, 0.58, 0.59,
0.6, 0.61, 0.62, 0.63, 0.64, 0.65, 0.66, 0.67, 0.68, 0.69, 0.7, 0.71, 0.72, 0.73, 0.74, 0.75,
0.76, 0.77, 0.78, 0.79, 0.8, 0.81, 0.82, 0.83, 0.84, 0.85, 0.86, 0.87, 0.88, 0.89, 0.9, 0.91,
0.92, 0.93, 0.94, 0.95, 0.96, 0.97, 0.98, 0.99, 1, 1.01, 1.02, 1.03, 1.04, 1.05, 1.06, 1.07,
1.08, 1.09, 1.1, 1.11, 1.12, 1.13, 1.14, 1.15, 1.16, 1.17, 1.18, 1.19, 1.2, 1.21, 1.22, 1.23,
1.24, 1.25, 1.26, 1.27, 1.28, 1.29, 1.3, 1.31, 1.32, 1.33, 1.34, 1.35, 1.36, 1.37, 1.38, 1.39,
1.4, 1.41, 1.42, 1.43, 1.44, 1.45, 1.46, 1.47, 1.48, 1.49, 1.5, 1.51, 1.52, 1.53, 1.54, 1.55,
1.56, 1.57, 1.58, 1.59, 1.6, 1.61, 1.62, 1.63, 1.64, 1.65, 1.66, 1.67, 1.68, 1.69, 1.7, 1.71,
1.72, 1.73, 1.74, 1.75, 1.76, 1.77, 1.78, 1.79, 1.8, 1.81, 1.82, 1.83, 1.84, 1.85, 1.86, 1.87,
1.88, 1.89, 1.9, 1.91, 1.92, 1.93, 1.94, 1.95, 1.96, 1.97, 1.98, 1.99, 2])
print(output)
output1 = model.predict([0.1, 0.2, 0.3, 0.4, 0.5, 0.6, 0.7, 0.8, 0.9, 1.0, 1.1, 1.2, 1.3, 1.4,
1.5, 1.6, 1.7, 1.8])
print(output1)
# Saving the model
# model.save('50Hz_coreloss_model.h5')
plt.xlabel('Flux Density')
plt.ylabel("Core Losses")
plt.plot(fluxdensity, output1)
plt.plot(fluxdensity, powerloss)
plt.show()
# print("These are the layer variables: ".format(l0.get_weights()))
# print("These are the layer variables: ".format(l1.get_weights()))
# print("These are the layer variables: ".format(l2.get_weights()))
# print("These are the layer variables: ".format(l3.get_weights()))
# print("These are the layer variables: ".format(l4.get_weights()))
```

Appendix A.7 - Machine Learning for Core Losses

```
# This model was scripted in the Python Programming Language
import pandas as pd
import numpy as np
from sklearn import model_selection
from sklearn.linear_model import LinearRegression
from sklearn.linear_model import Ridge
from sklearn.linear_model import Lasso
from sklearn.linear_model import ElasticNet
from sklearn.neighbors import KNeighborsRegressor
from sklearn.tree import DecisionTreeRegressor
from sklearn.svm import SVR
from sklearn.ensemble import RandomForestRegressor
from sklearn.metrics import r2_score
from sklearn.model_selection import train_test_split
from sklearn.metrics import mean_squared_error
from math import sqrt
import matplotlib.pyplot as plt
import matplotlib.tri as mtri
from mpl_toolkits.mplot3d import Axes3D
"dataset is the dataset I want the machine to use to find the pattern"
dataset = pd.read_csv(r"filepath.csv", sep=',')
"polpulate is the same dataset I'm gonna use to compare the machine learning's output"
populate = pd.read_csv(r"filepath.csv", sep=',')
"see the number of rows and columns of the populate dataset"
print(populate.shape)
"see the statistical details of the populate dataset"
print(populate.describe())
"choose the independent data; in this case, I want the model to learn the output based
on these inputs"
X = dataset[['frequency', 'flux_density']]
"this is the output I want the model to predict"
y = dataset['coreloss']
"this is just input data I'm going to use to compare the final result of the model"
Xpop = populate[['frequency', 'flux_density']]
"splitting the data up between testing and training data; variable test_size ranges from
```

0 to 1 and is percentage based”
X_train, X_test, y_train, y_test = train_test_split(X, y, test_size=0.05, random_state=40)
”this configures the random forest regressor that I’m gonna use to find the relationships between the input and output”
”data” model_rf = RandomForestRegressor(n_estimators=1000, oob_score=True, random_state=50)
”executes the task of finding the relationship”
model_rf.fit(X_train, y_train)
# training is finished
”predict outputs based on X_train inputs”
pred_train_rf = model_rf.predict(X_train)
”prints mean squared error between the training and predicted outputs used this to check the accuracy”
print(np.sqrt(mean_squared_error(y_train, pred_train_rf)))
print(r2_score(y_train, pred_train_rf))
pred_test_rf = model_rf.predict(X_test)
print(np.sqrt(mean_squared_error(y_test, pred_test_rf)))
print(r2_score(y_test, pred_test_rf))
”performs the predictions; I used the same training dataset to visually see how it compares to the actual datapoints”
pred_pop_rf = model_rf.predict(Xpop)
”splits datasets so that it can be used to plot graphs”
x = dataset[’frequency’]
y = dataset[’flux_density’]
z = dataset[’coreloss’]
xp = populate[’frequency’]
yp = populate[’flux_density’]
zp = pred_pop_rf
fig = plt.figure()
”some settings to overlay the data on a 3d graph with different colours”
ax = fig.add_subplot(111, projection=’3d’)
”uncomment this to get a surface on the 3d graph”
ax.plot_trisurf(x, y, z, cmap=’Greys’)
”creates the scatter plots on the 3d graph”
ax.scatter(x, y, z, marker=’.’, s=10, c=”black”, alpha=0.5)
ax.scatter(xp, yp, zp, marker=’.’, s=10, c=”red”, alpha=0.5)
ax.view_init(elev=60, azim=-45)

```
plt.xlabel('Frequency')
plt.ylabel("Flux Density")
plt.title("Core Loss")
plt.show()
"predict the frequency-flux density combinations"
wanted = [[58.33, 0.74], [116.67, 0.05], [175, 0.02], [58.33, 1.19], [116.67, 0.04], [175,
0.43], [233.33, 0.02], [25, 1.68], [75, 0.54], [125, 0.03], [25, 0.33], [75, 0.13], [125, 0.01]]
print(model_rf.predict(wanted))
```

Appendix B - Mechanical Drawings

Appendix B.1 - Stator Laminations

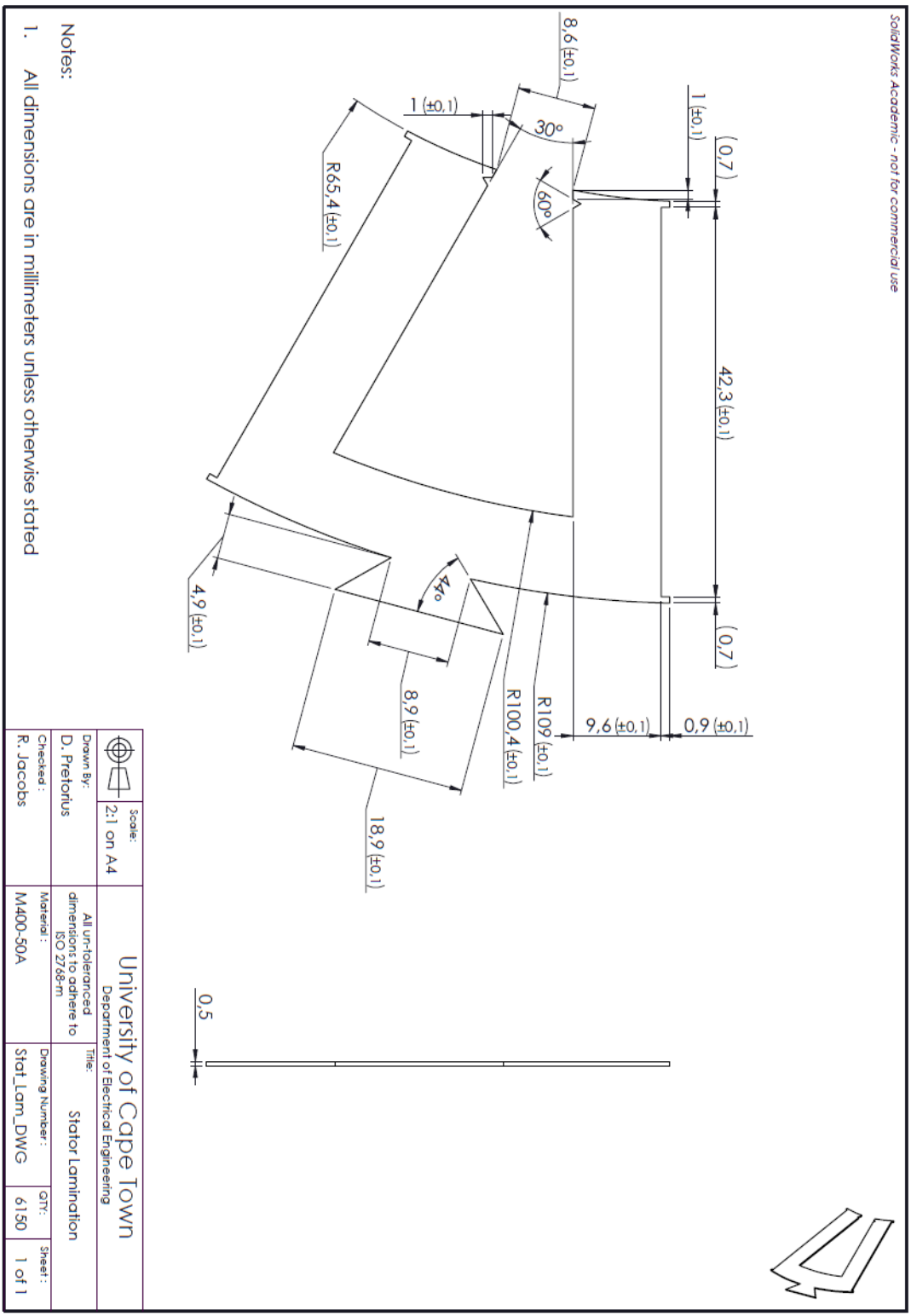

Appendix B.2 - Rotor Laminations

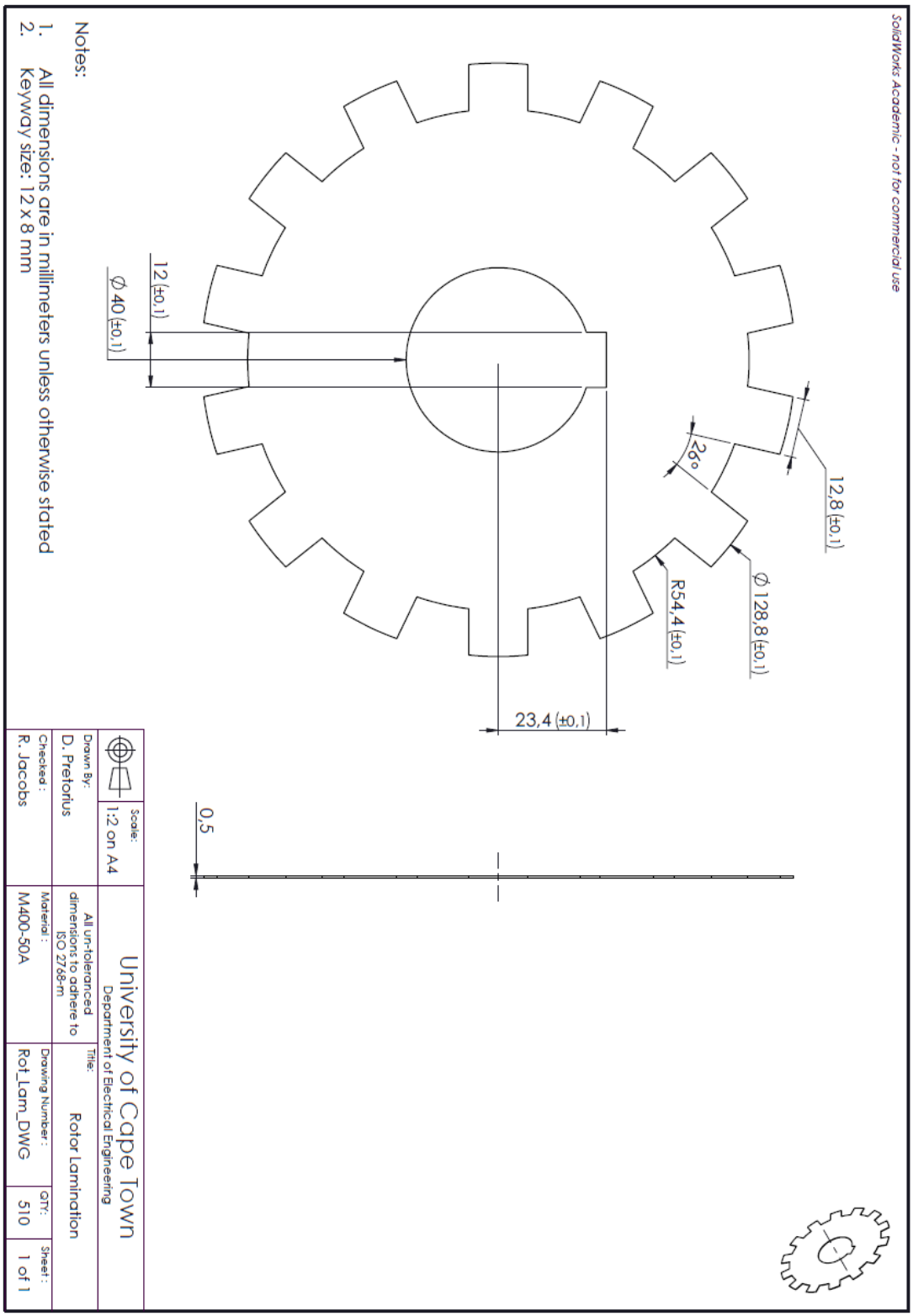

Appendix B.3 - Permanent Magnets

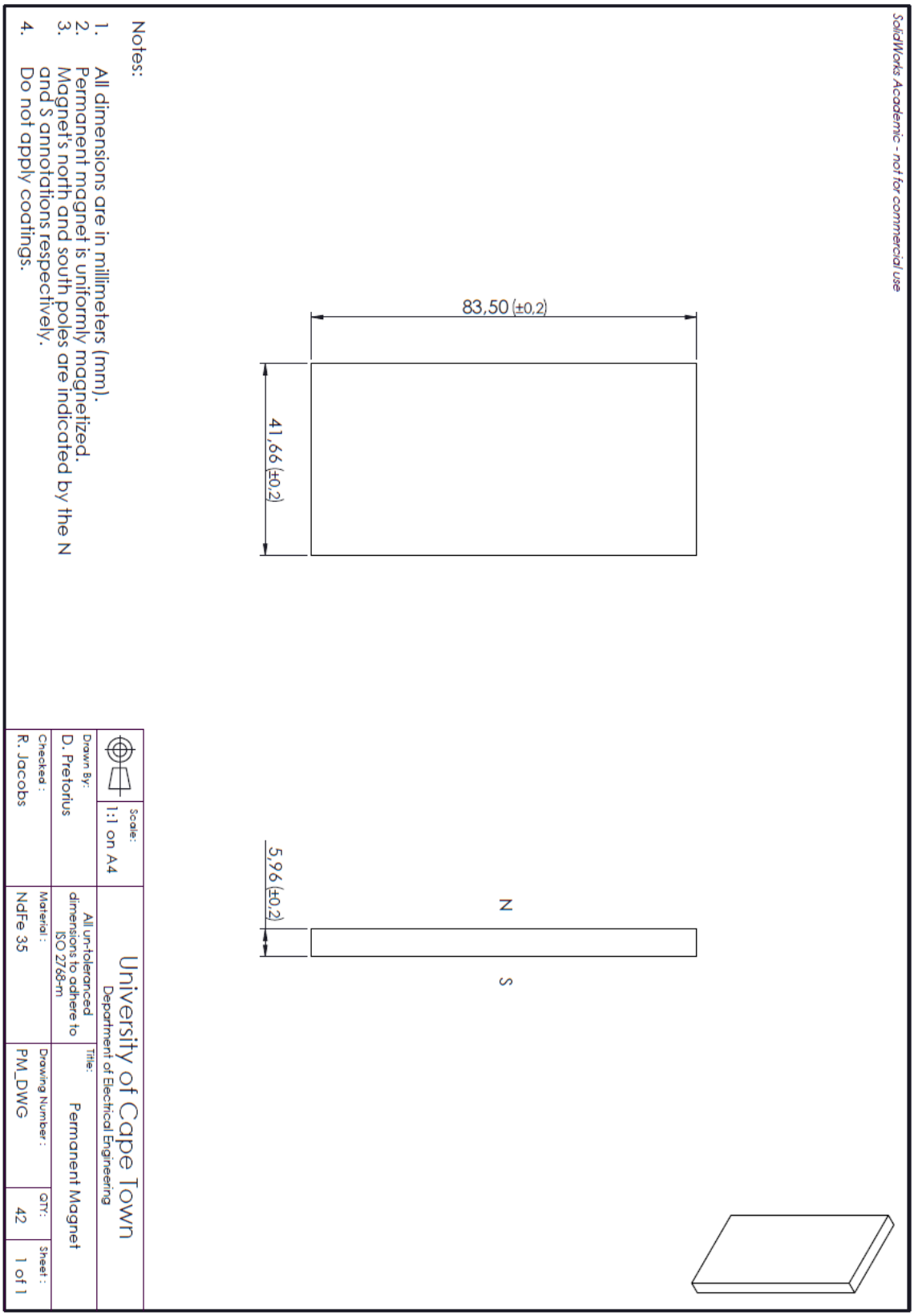

Appendix C - Wire Gauge Chart

Wire Number (Gauge) in gauge	Standard Wire Gauge (SWG) in mm
0000000 (7/0)	12.700
000000 (6/0)	11.786
00000 (5/0)	10.973
0000 (4/0)	10.160
000 (3/0)	9.449
00 (2/0)	8.839
0 (1/0)	8.230
1	7.620
2	7.010
3	6.401
4	5.893
5	5.385
6	4.877
7	4.470
8	4.064
9	3.658
10	3.251
11	2.946
12	2.642
13	2.337
14	2.032
15	1.829
16	1.626
17	1.422
18	1.219
19	1.016
20	0.914
21	0.813
22	0.711
23	0.610
24	0.599
25	0.508

Wire Number (Gauge) in gauge	Standard Wire Gauge (SWG) in mm
26	0.457
27	0.417
28	0.376
29	0.345
30	0.315
31	0.295
32	0.274
33	0.254
34	0.234
35	0.213
36	0.193
37	0.173
38	0.152
39	0.132
40	0.122
41	0.112
42	0.102
43	0.0914
44	0.0813
45	0.0711
46	0.0610
47	0.0508
48	0.0406
49	0.0305
50	0.0254